

## **INFORMATION TO USERS**

This manuscript has been reproduced from the microfilm master. UMI films the text directly from the original or copy submitted. Thus, some thesis and dissertation copies are in typewriter face, while others may be from any type of computer printer.

**The quality of this reproduction is dependent upon the quality of the copy submitted.** Broken or indistinct print, colored or poor quality illustrations and photographs, print bleedthrough, substandard margins, and improper alignment can adversely affect reproduction..

In the unlikely event that the author did not send UMI a complete manuscript and there are missing pages, these will be noted. Also, if unauthorized copyright material had to be removed, a note will indicate the deletion.

Oversize materials (e.g., maps, drawings, charts) are reproduced by sectioning the original, beginning at the upper left-hand corner and continuing from left to right in equal sections with small overlaps.

Photographs included in the original manuscript have been reproduced xerographically in this copy. Higher quality 6" x 9" black and white photographic prints are available for any photographs or illustrations appearing in this copy for an additional charge. Contact UMI directly to order.

ProQuest Information and Learning  
300 North Zeeb Road, Ann Arbor, MI 48106-1346 USA  
800-521-0600

**UMI<sup>®</sup>**



**University of Alberta**

**Relativistic Calculations for Incoherent Photoproduction  
of Eta Mesons**

by

**Ian Richard Blokland**



A thesis submitted to the Faculty of Graduate Studies and Research in partial  
fulfillment of the requirements for the degree of Master of Science

**Department of Physics**

**Edmonton, Alberta**

**Spring 2000**



**National Library  
of Canada**

**Acquisitions and  
Bibliographic Services**

**395 Wellington Street  
Ottawa ON K1A 0N4  
Canada**

**Bibliothèque nationale  
du Canada**

**Acquisitions et  
services bibliographiques**

**395, rue Wellington  
Ottawa ON K1A 0N4  
Canada**

*Your file Votre référence*

*Our file Notre référence*

The author has granted a non-exclusive licence allowing the National Library of Canada to reproduce, loan, distribute or sell copies of this thesis in microform, paper or electronic formats.

The author retains ownership of the copyright in this thesis. Neither the thesis nor substantial extracts from it may be printed or otherwise reproduced without the author's permission.

L'auteur a accordé une licence non exclusive permettant à la Bibliothèque nationale du Canada de reproduire, prêter, distribuer ou vendre des copies de cette thèse sous la forme de microfiche/film, de reproduction sur papier ou sur format électronique.

L'auteur conserve la propriété du droit d'auteur qui protège cette thèse. Ni la thèse ni des extraits substantiels de celle-ci ne doivent être imprimés ou autrement reproduits sans son autorisation.

0-612-60104-8

**Canada**

**University of Alberta**

**Library Release Form**

NAME OF AUTHOR: Ian Richard Blokland

TITLE OF THESIS: Relativistic Calculations for Incoherent Photoproduction of Eta Mesons

DEGREE: Master of Science

YEAR THIS DEGREE GRANTED: 2000

Permission is hereby granted to the University of Alberta Library to reproduce single copies of this thesis and to lend or sell such copies for private, scholarly or scientific research purposes only.

The author reserves all other publication and other rights in association with the copyright in the thesis, and except as hereinbefore provided neither the thesis nor any substantial portion thereof may be printed or otherwise reproduced in any material form whatever without the author's prior written permission.



---

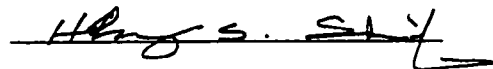
Ian Richard Blokland  
Apt. 416  
11104 - 84th Avenue NW  
Edmonton Alberta  
CANADA T6G 2R4

December 6, 1999

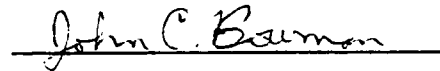
**University of Alberta**

**Faculty of Graduate Studies and Research**

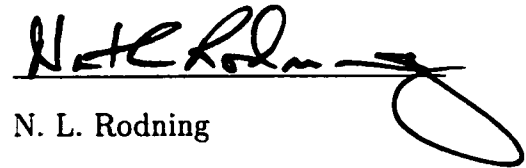
The undersigned certify that they have read, and recommend to the Faculty of Graduate Studies and Research for acceptance, a thesis entitled **Relativistic Calculations for Incoherent Photoproduction of Eta Mesons** submitted by **Ian Richard Blokland** in partial fulfillment of the requirements for the degree of Master of Science.



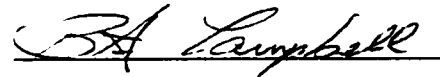
H. S. Sherif (Supervisor)



J. C. Bowman (External)



N. L. Rodning



B. A. Campbell

DATE: NOVEMBER 29, 1999

## Abstract

A relativistic model for incoherent photoproduction of  $\eta$  mesons from complex nuclei is developed. The elementary process is described using an effective Lagrangian containing photons, nucleons, nucleon resonances, and  $\rho$ ,  $\omega$ , and  $\eta$  mesons. The nucleon and  $\eta$  wavefunctions are obtained from relativistic wave equations using potentials that simulate meson exchanges. Nuclear structure is incorporated by using the Nuclear Shell Model.

Expressions are obtained for the reaction amplitude and the physical observables for incoherent  $\eta$ -photoproduction processes. Numerical results are presented for a number of reaction scenarios. The cross sections are found to be slightly smaller than those from a corresponding nonrelativistic calculation. The cross sections for incoherent  $\eta$ -photoproduction reactions are several orders of magnitude smaller than those of quasifree processes and of comparable size to those of coherent processes. The calculations are found to be quite sensitive to the choice of parameters used in the effective Lagrangian.

The great mass of workers in between, connecting one step to another, are improving all the time our understanding of the world, both from working at the ends and working in the middle, and in that way we are gradually understanding this tremendous world of interconnecting hierarchies.

Richard Feynman



## Acknowledgements

First, I sincerely give thanks to my supervisor, Dr. Helmy Sherif, for patiently and wisely guiding me through this research. I am also grateful to Mohammad Hedayati-Poor and Jon Johansson for the thousands of lines of Fortran code that they left behind and for the time they took to help me through it.

I am indebted to Lynn Chandler and all the office staff for their efforts which have allowed me to concentrate on physics. Conversely, when it was time to take my mind off physics, I could always count on the help of some of the other graduate students in the department. In particular, the Hockey Pool and the Monday Night Hockey league were useful distractions.

I also wish to acknowledge the financial support of the Natural Sciences and Engineering Research Council.

Finally, I would like to thank Alice for agreeing to come to Edmonton to be my wife.

# Table of Contents

<b>1</b>	<b>Introduction</b>	<b>1</b>
<b>2</b>	<b>Theory</b>	<b>7</b>
2.1	Resonances . . . . .	8
2.2	The Effective Lagrangian . . . . .	9
2.3	Derivation of the Reaction Amplitude . . . . .	12
2.3.1	Relating $S$ to the Interaction Lagrangian . . . . .	12
2.3.2	Initial and Final States . . . . .	14
2.3.3	Lowest-Order Contributions to $S_{fi}$ . . . . .	15
2.3.4	Fock Space Calculations . . . . .	16
2.3.5	Approximating the Propagator . . . . .	18
2.3.6	Putting the Pieces Together . . . . .	19
2.4	Feynman Rules . . . . .	21
2.5	Observables . . . . .	25
2.5.1	Preliminary Simplifications . . . . .	26
2.5.2	Fermi's Golden Rule . . . . .	27
2.5.3	The Recoil Factor . . . . .	28
2.5.4	Spin Summations . . . . .	30
2.5.5	Units . . . . .	31

## TABLE OF CONTENTS

2.5.6	Final Form of the Observables . . . . .	32
Appendix 2.A	Gauge Invariance . . . . .	34
<b>3</b>	<b>Details of the Calculation</b>	<b>37</b>
3.1	Kinematics . . . . .	37
3.1.1	Outer Kinematics . . . . .	38
3.1.2	Inner Kinematics . . . . .	42
3.2	Particle Wavefunctions . . . . .	43
3.2.1	Nucleon Wavefunctions . . . . .	43
3.2.2	The Photon Wavefunction . . . . .	46
3.2.3	The $\eta$ Meson Wavefunction . . . . .	47
3.2.4	The Plane Wave Approximation . . . . .	48
3.2.5	The Distorted Wave Approximation . . . . .	49
3.2.6	$\eta$ Optical Potentials . . . . .	50
3.3	Evaluation of the Integral . . . . .	54
3.3.1	Substituting the Wavefunctions . . . . .	54
3.3.2	The Radial Integrals . . . . .	55
3.3.3	The Angular Integrals . . . . .	56
Appendix 3.A	Parameter Values . . . . .	60
Appendix 3.B	The Spectroscopic Factors . . . . .	63
Appendix 3.C	Tests of the Code . . . . .	68
<b>4</b>	<b>Results for the Reaction <math>A(\gamma, \eta)A^*</math></b>	<b>70</b>
4.1	Model Calculations . . . . .	71
4.1.1	The $^{16}\text{O}(\gamma, \eta)^{16}\text{O}^*(3^-; 7.88)$ Reaction . . . . .	71
4.1.2	The $^{12}\text{C}(\gamma, \eta)^{12}\text{C}^*(2^+; 4.44)$ Reaction . . . . .	81
4.1.3	The $^{12}\text{C}(\gamma, \eta)^{12}\text{C}^*(2^+; 16.11)$ Reaction . . . . .	81

## TABLE OF CONTENTS

4.1.4	The $^{12}\text{C}(\gamma, \eta)^{12}\text{C}^*(1^+; 12.71)$ Reaction . . . . .	85
4.1.5	The $^{12}\text{C}(\gamma, \eta)^{12}\text{C}^*(3^-; 9.641)$ Reaction . . . . .	85
4.1.6	The $^{40}\text{Ca}(\gamma, \eta)^{40}\text{Ca}^*(5^-; 4.48)$ Reaction . . . . .	88
4.1.7	Discussion of Results . . . . .	89
4.2	Realistic Modifications to the Model . . . . .	90
4.2.1	Isospin Considerations . . . . .	90
4.2.2	Realistic Spectroscopic Factors . . . . .	93
4.2.3	Transforming to the Center of Momentum Frame . . . . .	94
4.2.4	Results of the Modified Calculations . . . . .	96
4.2.5	Discussion of Results . . . . .	97
4.3	Sensitivity to Parameters . . . . .	101
<b>5</b>	<b>Conclusion</b>	<b>106</b>
	<b>Bibliography</b>	<b>111</b>

# List of Tables

1.1	Classification of $\eta$ -photoproduction processes on a target $A$ . . . .	4
2.1	Properties of the three nucleon resonances that will be used in our model . . . . .	9
3.1	Woods-Saxon binding potential parameters for $^{16}\text{O}$ . . . . .	45
3.2	Masses and widths of the particles in our calculations [2] . . . . .	60
3.3	Coupling constants and magnetic moments used in our calculations	61
3.4	Off-shell parameters used in our calculations . . . . .	61
3.5	Hierarchy and occupancy of nuclear shells . . . . .	63
3.6	Wavefunction of the $3^-$ , $E_x = 7.88$ MeV state of $^{16}\text{O}$ . . . . .	64
3.7	Resonance configurations used in our calculations . . . . .	65
4.1	Parameters changed in the new parameter set . . . . .	102

# List of Figures

2.1	Feynman diagram for a $\gamma + N \longrightarrow \eta + N$ reaction . . . . .	21
2.2	The vertex specified by $\mathcal{L}_{\eta NN}$ . . . . .	22
2.3	The contributing Feynman diagrams to the $\gamma + N \longrightarrow \eta + N$ reaction	23
3.1	Definition of the coordinate system used for this reaction . . . . .	39
3.2	The upper and lower component radial wavefunctions of the $1p_{\frac{1}{2}}$ proton of $^{16}\text{O}$ . . . . .	46
3.3	Graph of the nuclear densities for $^{12}\text{C}$ , $^{16}\text{O}$ , and $^{40}\text{Ca}$ . . . . .	52
3.4	Comparison of the DW1 and DW3 optical potentials . . . . .	53
4.1	Differential cross sections for the $^{16}\text{O}(\gamma, \eta)^{16}\text{O}^*(3^-; 7.88)$ reaction with $E_\gamma = 600$ MeV. The upper graph shows the total differential cross sections. The lower graph shows the contributions to the DW1 differential cross section from the individual diagrams. . . . .	73
4.2	Differential cross sections for the $^{16}\text{O}(\gamma, \eta)^{16}\text{O}^*(3^-; 7.88)$ reaction with $E_\gamma = 750$ MeV . . . . .	74
4.3	Differential cross sections for the $^{16}\text{O}(\gamma, \eta)^{16}\text{O}^*(3^-; 7.88)$ reaction with $E_\gamma = 900$ MeV . . . . .	75
4.4	Photon asymmetries for the $^{16}\text{O}(\gamma, \eta)^{16}\text{O}^*(3^-; 7.88)$ reaction with $E_\gamma = 600$ MeV . . . . .	77

## LIST OF FIGURES

4.5	Photon asymmetries for the $^{16}\text{O}(\gamma, \eta)^{16}\text{O}^*(3^-; 7.88)$ reaction with $E_\gamma = 750$ MeV . . . . .	78
4.6	Photon asymmetries for the $^{16}\text{O}(\gamma, \eta)^{16}\text{O}^*(3^-; 7.88)$ reaction with $E_\gamma = 900$ MeV . . . . .	79
4.7	Total cross sections for the $^{16}\text{O}(\gamma, \eta)^{16}\text{O}^*(3^-; 7.88)$ reaction . . . .	80
4.8	Total cross sections for the $^{12}\text{C}(\gamma, \eta)^{12}\text{C}^*(2^+; 4.44)$ reaction . . . .	82
4.9	Differential cross sections for the $^{12}\text{C}(\gamma, \eta)^{12}\text{C}^*(2^+; 4.44)$ reaction with $E_\gamma = 750$ MeV . . . . .	83
4.10	Total cross sections for the $^{12}\text{C}(\gamma, \eta)^{12}\text{C}^*(2^+; 16.11)$ reaction . . .	84
4.11	Total cross sections for the $^{12}\text{C}(\gamma, \eta)^{12}\text{C}^*(1^+; 12.71)$ reaction . . .	86
4.12	Total cross sections for the $^{12}\text{C}(\gamma, \eta)^{12}\text{C}^*(3^-; 9.641)$ reaction . . .	87
4.13	Total cross sections for the $^{40}\text{Ca}(\gamma, \eta)^{40}\text{Ca}^*(5^-; 4.48)$ reaction . . .	88
4.14	Model calculations for the $^{12}\text{C}(\gamma, \eta)^{12}\text{C}^*(2^+; 4.44)$ and $^{12}\text{C}(\gamma, \eta)^{12}\text{C}^*(2^+; 16.11)$ reactions . . . . .	97
4.15	Modified calculations for the $^{12}\text{C}(\gamma, \eta)^{12}\text{C}^*(2^+0; 4.44)$ and $^{12}\text{C}(\gamma, \eta)^{12}\text{C}^*(2^+1; 16.11)$ reactions . . . . .	98
4.16	Calculations of Bennhold and Tanabe for the angular distributions of the reactions $^{12}\text{C}(\gamma, \eta)^{12}\text{C}^*(2^+1; 16.11)$ and $^{12}\text{C}(\gamma, \eta)^{12}\text{C}^*(2^+0; 4.44)$ , as taken from Figure 19 of [1] . . . . .	99
4.17	Comparison of the total PW cross sections for the $^{12}\text{C}(\gamma, \eta)^{12}\text{C}^*(2^+; 4.44)$ reaction using different parameter sets . . . . .	103
4.18	Contributions from the different diagrams to the differential cross section of the $^{12}\text{C}(\gamma, \eta)^{12}\text{C}^*(2^+; 4.44)$ reaction when $E_\gamma = 750$ MeV using the new parameter set . . . . .	104

# Chapter 1

## Introduction

The  $\eta$  meson is an intriguing particle that plays significant roles in both nuclear and particle physics. Until recently, experiments involving the  $\eta$  have been few and somewhat crude. This is changing, though, because the advent of high duty-cycle electron accelerators at JLAB (CEBAF), Bates, Mainz (MAMI), and Bonn (ELSA) has allowed nuclear meson production reactions to be probed at high enough energies to study  $\eta$ -photoproduction on complex nuclei. Data from these experiments will permit the evaluation of previous theoretical work and assist future theoretical research.

The  $\eta$  has a rest mass of  $(547.30 \pm 0.12)$  MeV/ $c^2$  [2], which is about half that of a nucleon and about four times that of a pion. It has a width of  $(1.18 \pm 0.11)$  keV, which corresponds to a lifetime of about  $7 \times 10^{-19}$  s. Its decay products include  $2\gamma$  ( $\approx 39\%$  of all  $\eta$  decays),  $3\pi^0$  ( $\approx 32\%$ ),  $\pi^+\pi^-\pi^0$  ( $\approx 23\%$ ) as well as a plethora of rare decays.

The  $\eta$  belongs to an  $SU(3)$  nonet of pseudoscalar mesons, therefore it has zero spin and  $P = -1$ . Charge conjugation and G-parity are  $+1$ , hence  $CP = -1$ . All its other quantum numbers are zero, including charge, strangeness, and most



importantly, isospin. In terms of its constituent quarks,  $\eta = \frac{1}{\sqrt{6}}(u\bar{u} + d\bar{d} - 2s\bar{s})$ .

The short lifetime of the  $\eta$  makes it impossible to prepare  $\eta$ -beams in order to investigate the  $\eta$ -nuclear potential with scattering experiments. The interactions between  $\eta$  mesons and nuclei must therefore be studied using reactions that produce the  $\eta$ . From a theoretical standpoint, the least complicated of these reactions is  $\eta$ -photoproduction:  $\gamma + p \rightarrow \eta + p$ . The threshold photon energy for  $\eta$ -photoproduction on a free proton is  $E_\gamma = 709.3$  MeV. If the target is a complex nucleus, the recoil effects are less significant and the threshold decreases toward the rest energy of the  $\eta$ .

$\eta$  meson research, both theoretical and experimental, is often based on the precedents set by similar research endeavors involving  $\pi$  mesons. Being the lightest of all mesons,  $\pi$  mesons cannot decay hadronically. This means that they live a great deal longer than  $\eta$  mesons and are easier to manage experimentally as a result. After the pions, though, the  $\eta$  is the most prolifically produced hadron in intermediate-energy reactions. The theoretical simplicity of the  $\eta$  stems from the fact that its electric charge and isospin are zero, so that Coulomb interactions with the  $\eta$  can be ignored. More importantly, the zero isospin restricts the  $\gamma + N$  coupling to an isospin- $\frac{1}{2}$  state. This is much simpler than the situation that arises with the isospin-1 pions, where the  $\gamma + N$  coupling can be isospin  $\frac{1}{2}$  or  $\frac{3}{2}$ .

The  $N^*(1535)$  is an  $S_{11}$  nucleon resonance with a mass that is 50 MeV greater than the combined mass of the  $\eta$  meson and a nucleon. This resonance is observed to decay into an  $\eta$  and a nucleon almost fifty percent of the time. On the other hand, the  $S_{11}$   $N^*(1650)$  resonance undergoes such a decay only a few percent of the time. This is an unsolved problem for quark models of resonance structure.

Recent experiments have determined that the  $\eta N$  scattering length is positive and large. This result has prompted speculation about the existence of eta-mesic

nuclei — bound or quasi-bound states of  $\eta$  mesons and nuclei.

The decays of the  $\eta$  often confront various conservation laws. As a result, the study of  $\eta$  decay can test physics both within and beyond the Standard Model. The major decay modes of the  $\eta$  are fairly well understood.  $\eta \rightarrow 2\gamma$  is a second-order electromagnetic transition that is forbidden in the limit of massless quarks. The strong decays  $\eta \rightarrow 2\pi$  and  $\eta \rightarrow 4\pi$  are forbidden by P and CP invariance. Since  $\eta$  is an eigenstate of the CP operator, Nefkens [21] suggests that a study of  $\eta \rightarrow 4\pi^0$  would constitute a good test of CP invariance. This would be a particularly useful experiment since CP violation has only been observed in the neutral K meson system. Unfortunately, the sensitivity of present  $\eta$  decay experiments would need to be improved by several orders of magnitude in order to detect  $\eta \rightarrow 4\pi^0$ . The decay  $\eta \rightarrow 3\pi$  is prohibited by charge symmetry conservation, but it does occur as a result of the quark mass terms in the QCD Lagrangian. By using charge symmetry breaking to examine  $\pi^0 - \eta$  mixing, it is possible to determine the mass difference between the up and down quarks. This is of special interest since QCD prohibits the existence of free quarks, which suggests that it is impossible to measure the mass of a quark directly. Precise measurements of the decays  $\eta \rightarrow 3\pi^0$ ,  $\eta \rightarrow \pi^0\gamma\gamma$ , and  $\eta \rightarrow \pi^+\pi^-\gamma$  will relate to chiral perturbation theory, a promising approach to strong interaction processes at low energies where QCD itself cannot be applied perturbatively.  $\eta$  decay can also be used to test other conservation principles, such as lepton family nonconservation in the decay  $\eta \rightarrow \mu e$ . Explanation of any such decays requires physics beyond the Standard Model.

Photoproduction reactions from complex nuclei can be classified into three types, depending on what happens to the target after the initial interaction. In a coherent process, the target is unchanged by the interaction. In an incoherent

process, the interaction leaves the target in an excited state, but still intact. In a quasifree process, the incident photon ejects a nucleon from the target during the interaction. The notations for these processes are given in Table 1.1.

Process	Notation
Coherent	$A(\gamma, \eta)A$
Incoherent	$A(\gamma, \eta)A^*$
Quasifree	$A(\gamma, N\eta)A - 1$

Table 1.1: Classification of  $\eta$ -photoproduction processes on a target  $A$

If we concern ourselves with any particular final state configuration of the target and any ejected nucleons, we describe this as an exclusive photoproduction reaction. On the other hand, if we only observe the  $\eta$  meson produced by the interaction, it is an inclusive photoproduction reaction.

As a result of the upgrades to the research facilities mentioned earlier, there are many  $\eta$ -photoproduction experiments currently under way or planned for the near future. In particular, researchers at MAMI have recently reported experimental data for inclusive  $\eta$ -photoproduction cross sections on  $p$ ,  $d$ ,  $^{12}\text{C}$ ,  $^{40}\text{Ca}$ ,  $^{93}\text{Nb}$ , and  $\text{Pb}$  for  $\gamma$  energies up to 790 MeV [3, 4, 5]. Also, the CLAS collaboration at JLAB is currently performing  $\eta$ -photoproduction experiments on proton and deuterium targets [6, 7].

Several groups have published theoretical descriptions of  $\eta$ -photoproduction. Due to the complexity of the problem and a dearth of experimental data from which theoretical parameters can be constrained and to which results can be compared, there have been a variety of interesting approaches.

Benmerrouche *et al.* [8] investigated  $\eta$ -photoproduction on a single nucleon within an effective Lagrangian approach (ELA). Their model included tree level

contributions from nucleon resonances,  $t$ -channel vector mesons, and nucleon Born diagrams. By optimizing fits to existing  $\eta$ -photoproduction data, they determined a set of phenomenological parameters for the effective Lagrangian.

Bennhold and Tanabe [9, 1] used a coupled channels isobar model, in which the  $\eta$ -photoproduction reaction  $(\gamma, \eta)$  was related to  $(\gamma, \pi)$ ,  $(\pi, \eta)$  and  $(\eta, \eta)$  reactions. They assumed that the elementary operator is a one-body operator in the nucleon space so that a  $t$ -matrix formalism arises. Tiator *et al.* [10] extended this work by including Born diagrams along with  $\rho$  and  $\omega$  meson exchange diagrams, all calculated using effective Lagrangians. Amplitudes for  $\eta$ -photoproduction on light nuclei were calculated in the plane wave impulse approximation (PWIA). These treatments made use of the large body of data for reactions involving the  $\pi$  meson to obtain parameters such as the  $\eta NN$  vertex factor.

Lee *et al.* [11] used the  $t$ -matrix parameters obtained by Bennhold and Tanabe to calculate exclusive and inclusive  $\eta$ -photoproduction amplitudes in the distorted wave approximation (DWA) for heavier nuclei such as  $^{12}\text{C}$  and  $^{40}\text{Ca}$ . Their approach used nonrelativistic nucleon wavefunctions.

Carrasco [12] used the ELA to calculate inclusive photoproduction of  $\eta$  mesons with the assumption that only the  $S_{11}(1535)$  nucleon resonance is involved. Final state interactions of the  $\eta$  meson with the residual nucleus were accounted for with a Monte Carlo approach.

Hombach *et al.* [13] modeled  $\eta$ -photoproduction from complex nuclei, using the coupled channel Boltzmann-Uehling-Uhlenbeck (BUU) formalism to describe the final-state interaction of the  $\eta$  meson. Effenberger and Sibirtsev [14] refined Hombach's approach by applying Glauber formalism to the MAMI data for  $\eta$ -photoproduction [5] in order to deduce certain properties of  $\eta N$  scattering.

Chen and Chiang [15] calculated a double differential inclusive cross section

for  $\eta$ -photoproduction on a  $^{12}\text{C}$  target by assuming that the underlying process is quasifree and only involves the  $S_{11}(1535)$  resonance.

Fix and Arenhövel [16] used the ELA to obtain the cross section for coherent  $\eta$ -photoproduction on  $^4\text{He}$  and  $^{12}\text{C}$  in the near-threshold region, using only the  $S_{11}(1535)$  and  $D_{13}(1520)$  resonances.

Hedayati-Poor and Sherif [17, 18, 19] developed a relativistic model for the quasifree photoproduction of  $\eta$  mesons on complex nuclei. An ELA was used and contributions from several nucleon resonances were included. The final state interaction of the  $\eta$  meson was taken into account using  $\eta$ -nucleus optical potentials.

Peters *et al.* [20] used an ELA with a relativistic, non-local model to study coherent  $\eta$ -photoproduction on spin-zero nuclei. Several optical potentials for the  $\eta$  final state interactions were compared.

In this thesis, we will use the relativistic model developed by Hedayati-Poor and Sherif [17] to examine the incoherent photoproduction of  $\eta$  mesons from complex nuclei.

# Chapter 2

## Theory

For the last half-century, Quantum Field Theory (QFT) has been a highly successful theory. In the realm of elementary particle physics, an experimental measurement of the anomalous magnetic moment of the electron has verified its predictions to 12 digits of precision [2]. It is somewhat paradoxical that some of the more recent accomplishments of QFT are in areas of research where a theoretical prediction that agrees with experiment to within ten percent is a laudable achievement.

One such area of research is nuclear physics, and in particular, the interactions of complex nuclei with intermediate-energy scattering probes. The photoproduction of  $\eta$  mesons from complex nuclei is an interesting problem in this field for at least two reasons. First, only recently has a fully relativistic field theoretic model of this reaction been used to calculate observable quantities [17, 18]. Second, there are several detailed experiments in progress, or planned for the near future, that will provide us with a great deal of data for these types of reactions. In this chapter, we will illustrate the ways in which QFT is used as part of a model for  $\eta$ -photoproduction.

## 2.1 Resonances

As we shall soon see, nucleon resonances play an important role in meson photo-production reactions. At the simplest level, we can describe a resonance as a very short-lived particle whose existence is inferred from unusual energy-dependent behavior of certain sets of experimental data. Baryon resonances can be pictured as excited states of longer-lived baryons, differing in mass as a result of a realignment of quark spins, for instance. Since these resonances have such short lifetimes, often less than  $10^{-23}$  s, it follows from the Heisenberg uncertainty relation

$$\Delta E \Delta t \geq \hbar \quad (2.1)$$

that there will be a significant spread in the energy, and hence, the mass of a resonance. We parametrize this phenomenon with a property called the width,  $\Gamma$ , of a resonance. Experimentally, it is actually  $\Gamma$  that is measured, which allows us to infer the lifetime of a resonance.

In order to completely parametrize a resonance, for our purposes, we need to specify its mass, width, and parity, as well as its angular momentum and isospin quantum numbers. The  $\eta$  meson has isospin zero, so we will only need to consider isospin- $\frac{1}{2}$  nucleon resonances. Based on the results of previous calculations [17, 18], only three resonances are expected to provide non-negligible contributions to the processes that we are considering. Their properties are summarized in Table 2.1. In this table, the nucleon resonances are labeled by  $N^*(M)$ , where  $M$  is the mass of the resonance in MeV. We can also describe resonances by their quantum numbers using the spectroscopic notation  $L_{(2I)(2J)}$ . Here,  $I$  is the total isospin quantum number,  $J$  is the total angular momentum quantum number, and  $L$  represents the orbital angular momentum quantum number. Using a

convention that dates back to atomic spectroscopy, we denote  $L = 0$  by the letter  $S$ ,  $L = 1$  by  $P$ ,  $L = 2$  by  $D$ , and all higher  $L$  values with the sequence of letters beginning with  $F$ . Another useful description is the  $J^\pi$  convention, whereby  $\pi$  represents the parity of the resonance, written as  $+$  or  $-$ .

There is an  $S_{11}$  resonance at 1650 MeV that decays less than 2 % of the time to an  $\eta$  meson and a nucleon, in sharp contrast to the  $S_{11}$  resonance at 1535 MeV which decays this way nearly 50 % of the time. There is no explanation for these dissimilar branching ratios. One of the long-term goals in nuclear physics is to obtain a better understanding of the formation of resonances and how they propagate within the nuclear medium.

Resonance	$L_{(2I)(2J)}$	$J^\pi$	Mass (MeV)	$\Gamma$ (MeV)
$N^*(1440)$	$P_{11}$	$(1/2)^+$	1440	350
$N^*(1520)$	$D_{13}$	$(3/2)^-$	1520	120
$N^*(1535)$	$S_{11}$	$(1/2)^-$	1535	150

Table 2.1: Properties of the three nucleon resonances that will be used in our model

## 2.2 The Effective Lagrangian

In any QFT the starting point is a Lagrangian density that describes the free dynamics of all the types of particles under consideration as well as the ways in which they can interact. In a QFT of elementary particles, such as Quantum Electrodynamics, the Lagrangian can be unambiguously written as a sum of free Lagrangians for the individual particle types and interaction Lagrangians, which can be constructed so that the resulting reaction amplitudes satisfy unitarity



and gauge invariance. In nuclear physics, however, the fundamental particles are protons, neutrons, resonances, and mesons. These are themselves composed of quarks, so we should not expect to construct a QFT in terms of nucleons and mesons that will be accurate at arbitrarily high energies. Nevertheless, in the right situations, we can construct a reliable QFT.

The first part of the effective Lagrangian arises from the description of nucleons within the nuclear medium. The strong force is mediated by mesons; to reflect this, Serot and Walecka developed a phenomenological model to describe nucleon dynamics within a nucleus [22]. This model, in its most general form, leads to coupled nonlinear field equations that cannot be solved. Even perturbation techniques are useless due to the size of the coupling constants. For high nuclear density, though, we can make the Mean Field Approximation, whereby we replace the meson field operators with their expectation values. This results in a workable model that is known as Quantum Hadrodynamics (QHD). QHD provides us with a theoretical justification for writing the wavefunction of a bound nucleon,  $\psi_B$ , as a solution of the Dirac equation with scalar and vector potentials,  $S(r)$  and  $V(r)$ , that approximate the meson exchanges responsible for nuclear binding:

$$[\vec{\alpha} \cdot \vec{p} + \beta(M + S(r)) + V(r)] \psi_B(\vec{x}) = E \psi_B(\vec{x}) \quad (2.2)$$

Similarly, the  $\eta$  wavefunction,  $\eta(x)$ , is obtained by solving the Klein-Gordon Equation with the appropriate optical potential for the  $\eta$ -nucleus system. This differs from most other field-theoretic approaches to  $\eta$ -photoproduction, such as that of Lee *et al.* [11], which have used nonrelativistic wavefunctions for  $\psi(x)$ , obtained via the Schrödinger Equation.

The other part of the effective Lagrangian consists of all the possible inter-

action terms. For the sake of simplicity, we can consider the elementary process

$$\gamma + p \longrightarrow \eta + p \quad (2.3)$$

and ignore the fact that the proton might be bound within a nucleus. Our roster of particles includes photons (which will be denoted by the subscript  $\gamma$ ), nucleons (N), eta mesons ( $\eta$ ), the  $\rho$  and  $\omega$  vector mesons (V), and the three nucleon resonances (R) of Table 2.1. The interaction Lagrangian will then be

$$\mathcal{L}_{\text{INT}} = \mathcal{L}_{\eta NN} + \mathcal{L}_{\gamma NN} + \mathcal{L}_{V\eta\gamma} + \mathcal{L}_{VNN} + \mathcal{L}_{\eta NR} + \mathcal{L}_{\gamma NR} \quad (2.4)$$

In reality, we will have  $(\mathcal{L}_{\eta NR} + \mathcal{L}_{\gamma NR})$  terms for each of the three types of resonances under consideration. The explicit forms of the terms in (2.4) are presented in [8]. Due to the negative parity of the  $\eta$  meson, we could use either a pseudoscalar or a pseudovector coupling for the  $\eta NN$  vertex. Bennhold and Tanabe [9, 1] found that the pseudoscalar coupling more accurately described the data for the elementary reaction, therefore we have:

$$\mathcal{L}_{\eta NN} = -ig_{\eta NN} \bar{\psi} \gamma_5 \psi \eta \quad (2.5)$$

$$\mathcal{L}_{\gamma NN} = -e \bar{\psi} \gamma_\mu A^\mu \psi - \frac{e\kappa_p}{4M} \bar{\psi} \sigma_{\mu\nu} F^{\mu\nu} \psi \quad (2.6)$$

$$\mathcal{L}_{VNN} = -g_v \bar{\psi} \gamma_\mu V^\mu \psi - \frac{g_t}{4M} \bar{\psi} \sigma_{\mu\nu} V^{\mu\nu} \psi \quad (2.7)$$

$$\mathcal{L}_{V\eta\gamma} = \frac{e\lambda_v}{4m_\eta} \epsilon_{\mu\nu\lambda\sigma} F^{\mu\nu} V^{\lambda\sigma} \eta \quad (2.8)$$

For an  $S_{11}$  resonance,

$$\mathcal{L}_{\eta NR} = -ig_{\eta NR} \bar{\psi} R \eta + H.c. \quad (2.9)$$

$$\mathcal{L}_{\gamma NR} = -\frac{e\kappa_p^R}{2(M + M_R)} \bar{R} \gamma_5 \sigma_{\mu\nu} F^{\mu\nu} \psi + H.c. \quad (2.10)$$

where  $H.c.$  denotes the Hermitian conjugate of the preceding term. Since a  $P_{11}$  resonance differs from an  $S_{11}$  resonance only in its parity, the  $P_{11}$  resonance terms

are easily obtained from (2.9) and (2.10) by including an additional  $\gamma_5$  operator. The  $D_{13}$  resonance terms are quite complicated. The coupling constants that appear in all these expressions must be determined from other experiments. Some of these constants are subject to a great deal of uncertainty, in large part due to a lack of comprehensive experimental data.

## 2.3 Derivation of the Reaction Amplitude

Having obtained an effective Lagrangian, we are now in a position to derive expressions that will describe observable quantities. In this section we will see in detail how the techniques of QFT can be used to write an expression for the reaction amplitude, or alternatively, the S-matrix, for the reaction  $\gamma + A \rightarrow \eta + A^*$ .

The S-matrix, which relates the initial state of the system ( $t \rightarrow -\infty$ ) to the final state ( $t \rightarrow \infty$ ), is given by

$$S = \sum_{n=0}^{\infty} \frac{(-i)^n}{n!} \int \dots \int d^4x_1 \dots d^4x_n T \{ \mathcal{H}_{\text{INT}}(x_1) \dots \mathcal{H}_{\text{INT}}(x_n) \} \quad (2.11)$$

where  $T$  denotes the time-ordered product of the operators in the braces and  $\mathcal{H}_{\text{INT}}$  is the interaction Hamiltonian.

### 2.3.1 Relating $S$ to the Interaction Lagrangian

Our first task will be to relate the factors of  $\mathcal{H}_{\text{INT}}$  in (2.11) to the  $\mathcal{L}_{\text{INT}}$  in (2.4). Since  $\mathcal{H}_{\text{INT}}$  is related to  $\mathcal{L}_{\text{INT}}$  by the Legendre transformation

$$\mathcal{H}_{\text{INT}}(\pi_k, \phi_k) = \sum_j \pi_j \dot{\phi}_j - \mathcal{L}_{\text{INT}}(\phi_k, \dot{\phi}_k) \quad (2.12)$$

where

$$\pi_j = \frac{\partial \mathcal{L}_{\text{INT}}}{\partial \dot{\phi}_j} \quad (2.13)$$

we see that

$$\mathcal{H}_{\text{INT}} = -\mathcal{L}_{\text{INT}} \quad (2.14)$$

provided  $\pi_j = 0 \ \forall j$ . Looking at (2.6), (2.7), (2.8), and (2.10), though, we see that  $\mathcal{L}_{\text{INT}}$  contains factors of

$$F^{\mu\nu} \equiv \partial^\mu A^\nu - \partial^\nu A^\mu \quad (2.15)$$

and

$$V^{\mu\nu} \equiv \partial^\mu V^\nu - \partial^\nu V^\mu \quad (2.16)$$

so (2.12) states that  $\mathcal{H}_{\text{INT}}$  is more complicated than  $\mathcal{L}_{\text{INT}}$ . The extra terms that we acquire are of the form

$$\frac{\partial \mathcal{L}_{\text{INT}}}{\partial \dot{\phi}_j} \dot{\phi}_j \quad (2.17)$$

For example, suppose

$$\mathcal{L}_{\text{INT}} = C_{\mu\nu} V^{\mu\nu} \quad (2.18)$$

This resembles the second term in (2.7). Then

$$\frac{\partial \mathcal{L}_{\text{INT}}}{\partial \dot{V}^\mu} \dot{V}^\mu = (C_{0\mu} - C_{\mu 0}) \dot{V}^\mu \quad (2.19)$$

so that the additional terms are not even covariant. Fortunately, the propagator for  $V^\mu$  will also involve noncovariant terms and it can be shown that these two sets of noncovariant terms will always cancel [23]. As a result, we can use (2.14) for all of our interactions.

Returning to (2.11), we now have

$$S = \sum_{n=0}^{\infty} \frac{i^n}{n!} \int \dots \int d^4 x_1 \dots d^4 x_n T \{ \mathcal{L}_{\text{INT}}(x_1) \dots \mathcal{L}_{\text{INT}}(x_n) \} \quad (2.20)$$

### 2.3.2 Initial and Final States

The reaction amplitude is just the S-matrix element involving the initial and final states:

$$S_{fi} = \langle f | S | i \rangle \quad (2.21)$$

$$S_{fi} = \sum_{n=0}^{\infty} \frac{i^n}{n!} \int \dots \int d^4x_1 \dots d^4x_n \langle f | T \{ \mathcal{L}_{\text{INT}}(x_1) \dots \mathcal{L}_{\text{INT}}(x_n) \} | i \rangle \quad (2.22)$$

In the elementary reaction (2.3), the initial state  $|i\rangle$  consists of a photon and a proton, so we can write

$$|i\rangle = a_r^\dagger(\vec{k}_\gamma) b_{s_i}^\dagger(\vec{k}_p) |0\rangle \quad (2.23)$$

where  $a_r^\dagger(\vec{k}_\gamma)$  is the creation operator for a photon with momentum  $\vec{k}_\gamma$  and polarization  $r$ , and  $b_{s_i}^\dagger(\vec{k}_p)$  creates a proton with momentum  $\vec{k}_p$  and spin  $s_i$ . For photoproduction on a nucleus, the initial state is a photon along with a target nucleus. According to the nuclear shell model, we can treat the target nucleus as a core along with a valence proton, so that

$$|i\rangle = a_r^\dagger(\vec{k}_\gamma) \sum_{J_B M_B J_C} (J_C, J_B; M_C, M_B | J_i, M_i) [S_{J_i J_C}(J_B)]^{1/2} b_{J_B M_B}^\dagger |\phi_{J_C}^{M_C}\rangle \quad (2.24)$$

where  $b_{J_B M_B}^\dagger$  creates a bound proton with angular momentum quantum numbers  $J_B$  and  $M_B$ . The core  $|\phi_{J_C}^{M_C}\rangle$  has quantum numbers  $J_C$  and  $M_C$  and since the target nucleus has quantum numbers  $J_i$  and  $M_i$ , we incur the Clebsch-Gordan coefficient  $(J_C, J_B; M_C, M_B | J_i, M_i)$ .  $[S_{J_i J_C}(J_B)]$  is a spectroscopic factor which expresses the probability that the real target nucleus has the configuration given in (2.24).

Similarly, the final state  $|f\rangle$  can be written as

$$|f\rangle = c_\eta^\dagger(\vec{k}_\eta) \sum_{J_{B'} M_{B'} J_C} (J_C, J_{B'}; M_C, M_{B'} | J_f, M_f) [S_{J_f J_C}(J_{B'})]^{1/2} b_{J_{B'} M_{B'}}^\dagger |\phi_{J_C}^{M_C}\rangle \quad (2.25)$$

where  $c_\eta^\dagger(\vec{k}_\eta)$  creates an  $\eta$  meson with momentum  $\vec{k}_\eta$ . Note that while the angular momentum quantum numbers of the initial bound proton change from  $\{J_B, M_B\}$  to  $\{J_{B'}, M_{B'}\}$  and those of the entire nucleus change from  $\{J_i, M_i\}$  to  $\{J_f, M_f\}$ , we assume that the core  $|\phi_{J_C}^{M_C}\rangle$  is unaffected by the interaction.

Using (2.24) and (2.25), (2.22) becomes

$$\begin{aligned}
S_{fi} = & \sum_{J_B M_B} \sum_{J_C} \sum_{J_{B'} M_{B'}} (J_C, J_B; M_C, M_B | J_i, M_i) (J_C, J_{B'}; M_C, M_{B'} | J_f, M_f) \\
& \times [S_{J_i J_C}(J_B)]^{1/2} [S_{J_f J_C}(J_{B'})]^{1/2} \sum_{n=0}^{\infty} \frac{i^n}{n!} \int \dots \int d^4 x_1 \dots d^4 x_n \\
& \times \langle 0 | b_{J_{B'}, M_{B'}} c_\eta(\vec{k}_\eta) T \{ \mathcal{L}_{\text{INT}}(x_1) \dots \mathcal{L}_{\text{INT}}(x_n) \} a_r^\dagger(\vec{k}_\gamma) b_{J_B M_B}^\dagger | 0 \rangle \quad (2.26)
\end{aligned}$$

where we have used

$$\langle \phi_{J_C}^{M_C} | \phi_{J_C}^{M_C} \rangle = 1 \quad (2.27)$$

### 2.3.3 Lowest-Order Contributions to $S_{fi}$

Each of the terms in the interaction Lagrangian contains exactly three field operators, so it is clear from (2.26) that the lowest-order contributions to  $S_{fi}$  will occur when  $n = 2$ . Therefore, to lowest order,

$$S_{fi} = -\frac{1}{2} \int \int d^4 x d^4 y \langle f | T \{ \mathcal{L}_{\text{INT}}(x) \mathcal{L}_{\text{INT}}(y) \} | i \rangle \quad (2.28)$$

By substituting (2.4) for  $\mathcal{L}_{\text{INT}}$ , we obtain a number of terms in the time ordering in (2.28), each consisting of the product of two specific interaction Lagrangians. Only those terms whose fields, when written in second quantized form, can be matched with the annihilation and creation operators in (2.26) will contribute to  $S_{fi}$ .

Consider, for instance, the terms  $\mathcal{L}_{\gamma NR}(x) \mathcal{L}_{\eta NR}(y) + \mathcal{L}_{\gamma NR}(y) \mathcal{L}_{\eta NR}(x)$ , or equivalently,  $2\mathcal{L}_{\gamma NR}(x) \mathcal{L}_{\eta NR}(y)$ , where  $R$  represents an  $S_{11}$  resonance. From (2.10)

and (2.9), we see that this yields a contribution to  $S_{fi}$  of

$$S_{fi}^R = -\frac{ie\kappa_p^R g_{\eta NR}}{2(M + M_R)} \int \int d^4x d^4y \langle f | T \left\{ [\bar{\psi} R \eta - \eta \bar{R} \psi] (y) \right. \\ \left. \times [\bar{R} \gamma_5 \sigma_{\mu\nu} F^{\mu\nu} \psi - \bar{\psi} \gamma_5 \sigma_{\mu\nu} F^{\mu\nu} R] (x) \right\} | i \rangle \quad (2.29)$$

where we have used

$$\sigma_{\mu\nu}^\dagger = \sigma_{\mu\nu} \quad (2.30)$$

and

$$F^{\mu\nu\dagger} = -F^{\mu\nu} \quad (2.31)$$

in order to obtain the minus sign in the second factor of the time ordering in (2.29). Next, we use Wick's Theorem to rewrite the time-ordered product as a sum of normal-ordered products permuted over every possible set of contractions.

We need  $\bar{\psi}$  and  $\eta$  in the normal ordering to match with  $|f\rangle$  as well as  $\psi$  and  $F^{\mu\nu}$  to match with  $|i\rangle$ . As a result, the resonance field operators must be contracted. Since

$$\underline{R(x) R(y)} = \underline{\bar{R}(x) \bar{R}(y)} = 0 \quad (2.32)$$

there will only be two surviving terms in (2.29):

$$S_{fi}^R = -\frac{ie\kappa_p^R g_{\eta NR}}{2(M + M_R)} \int \int d^4x d^4y \langle f | N \left\{ \bar{\psi}(y) \eta(y) \underline{R(y) \bar{R}(x)} \gamma_5 \sigma_{\mu\nu} F^{\mu\nu}(x) \psi(x) \right. \\ \left. + \bar{\psi}(x) \gamma_5 \sigma_{\mu\nu} F^{\mu\nu}(x) \underline{R(x) \bar{R}(y)} \psi(y) \eta(y) \right\} | i \rangle \quad (2.33)$$

### 2.3.4 Fock Space Calculations

For the  $\eta$  meson, with the second quantized form

$$\eta(x) = \frac{1}{(2\pi)^{3/2}} \int \frac{d^3\vec{k}}{\sqrt{2E_k}} \left[ c_\eta^\dagger(\vec{k}) \Phi_\eta^*(k, x) + c_\eta(\vec{k}) \Phi_\eta(k, x) \right] \quad (2.34)$$

we obtain

$$\langle 0 | c_\eta(\vec{k}_\eta) \eta(y) | 0 \rangle = \frac{1}{(2\pi)^{3/2}} \frac{1}{\sqrt{2E_\eta}} \Phi_\eta^*(k_\eta, x) \quad (2.35)$$

since

$$[c_\eta(\vec{k}), c_\eta^\dagger(\vec{k}')] = \delta(\vec{k} - \vec{k}') \quad (2.36)$$

Similarly, for the electromagnetic field,

$$A^\mu(x) = \frac{1}{(2\pi)^{3/2}} \sum_r \epsilon_r^\mu \int \frac{d^3\vec{k}}{\sqrt{2E_k}} [a_r(\vec{k}) e^{-ik \cdot x} + a_r^\dagger(\vec{k}) e^{ik \cdot x}] \quad (2.37)$$

and therefore

$$F^{\mu\nu} = \frac{-i}{(2\pi)^{3/2}} \sum_r \int \frac{d^3\vec{k}}{\sqrt{2E_k}} [a_r(\vec{k}) e^{-ik \cdot x} - a_r^\dagger(\vec{k}) e^{ik \cdot x}] \{k^\mu \epsilon_r^\nu - k^\nu \epsilon_r^\mu\} \quad (2.38)$$

We need to evaluate

$$\langle 0 | \sigma_{\mu\nu} F^{\mu\nu}(x) a_r^\dagger(\vec{k}_\gamma) | 0 \rangle = \frac{-i\sigma_{\mu\nu}}{(2\pi)^{3/2}} \frac{1}{\sqrt{2E_\gamma}} e^{-ik_\gamma \cdot x} \{k_\gamma^\mu \epsilon_r^\nu - k_\gamma^\nu \epsilon_r^\mu\} \quad (2.39)$$

but

$$\begin{aligned} -i\sigma_{\mu\nu} \{k_\gamma^\mu \epsilon_r^\nu - k_\gamma^\nu \epsilon_r^\mu\} &= \frac{1}{2} (\gamma_\mu \gamma_\nu - \gamma_\nu \gamma_\mu) \{k_\gamma^\mu \epsilon_r^\nu - k_\gamma^\nu \epsilon_r^\mu\} \\ &= \frac{1}{2} [\not{k}_\gamma \not{\epsilon}_r - \not{\epsilon}_r \not{k}_\gamma - \not{\epsilon}_r \not{k}_\gamma + \not{k}_\gamma \not{\epsilon}_r] \\ &= 2\not{k}_\gamma \not{\epsilon}_r \end{aligned} \quad (2.40)$$

where in the last step we used  $\not{\epsilon}_r \not{k}_\gamma = -\not{k}_\gamma \not{\epsilon}_r$ , since  $k_\gamma \cdot \epsilon_r = 0$ . With (2.40), (2.39)

becomes

$$\langle 0 | \sigma_{\mu\nu} F^{\mu\nu}(x) a_r^\dagger(\vec{k}_\gamma) | 0 \rangle = \frac{2}{(2\pi)^{3/2}} \frac{1}{\sqrt{2E_\gamma}} e^{-ik_\gamma \cdot x} \not{k}_\gamma \not{\epsilon}_r \quad (2.41)$$

Finally, for a bound proton, the field operator  $\psi(x)$  can be written in second quantized form as

$$\psi(x) = \sum_n [b_n u_n(x) + d_n^\dagger v_n(x)] \quad (2.42)$$



where  $n$  refers to the angular momentum quantum numbers of any particular bound state. If the proton was not bound, we would write

$$\psi(x) = \sum_s \int \frac{d^3\vec{k}}{(2\pi)^{3/2}} \sqrt{\frac{M}{E_k}} \left[ b_s(\vec{k}) u_s(k, x) + d_s^\dagger(\vec{k}) v_s(k, x) \right] \quad (2.43)$$

An incoherent photoproduction reaction is characterized by the final nucleus being an excited state of the initial nucleus. Since we are considering incoherent  $\eta$ -photoproduction, we use (2.42) to write

$$\langle 0 | b_{J_B, M_B} N \left[ \bar{\psi}(y) \psi(x) \right] b_{J_B, M_B}^\dagger | 0 \rangle = \bar{u}_{J_B, M_B}(y) u_{J_B, M_B}(x) \quad (2.44)$$

with the provision that since  $\bar{u}$  and  $u$  are Dirac spinors, we must put any  $4 \times 4$  matrix operators, such as the ones in (2.41), between these two spinors so that  $S_{fi}$  is just a number.

### 2.3.5 Approximating the Propagator

Having completed the Fock space calculations, the last thing we need to evaluate for the  $S_{fi}^R$  in (2.33) is the contraction of  $R(y)$  with  $\bar{R}(x)$ . Since, for an  $S_{11}$  resonance,  $R$  is a fermion field, the contraction results in the configuration space Feynman propagator:

$$\begin{aligned} \underline{R(y) \bar{R}(x)} &= i S_F(y - x) \\ &= \frac{i}{(2\pi)^4} \int d^4 k_R \frac{\not{k}_R + M_R}{k_R^2 - M_R^2 + i\epsilon} e^{-ik_R \cdot (y-x)} \end{aligned} \quad (2.45)$$

From (2.33), we see that there are  $\int \int d^4 x d^4 y$  integrations remaining. In the limit that the  $\eta$  meson and the proton in  $|f\rangle$  are both plane waves, we can perform the  $\int d^4 x$  and  $\int d^4 k_R$  integrations explicitly [24]. The result that we obtain is equivalent to writing

$$\underline{R(y) \bar{R}(x)} = i \frac{\not{k}_R + M_R}{k_R^2 - M_R^2} \delta^4(y - x) \quad (2.46)$$

and imposing overall four-momentum conservation for the reaction, without making explicit assumptions about the particles in  $|f\rangle$ .

### 2.3.6 Putting the Pieces Together

Using (2.46) and the Fock space calculations (2.35), (2.41), and (2.44) in expression (2.33) for  $S_{fi}^R$ , we obtain

$$\begin{aligned}
 S_{fi}^R &= \frac{e}{(2\pi)^3} \sqrt{\frac{1}{2E_\eta 2E_\gamma}} \sum_{J_C J_B M_B} \sum_{J_{B'} M_{B'}} (J_C, J_B; M_C, M_B | J_i, M_i) \\
 &\quad \times (J_C, J_{B'}; M_C, M_{B'} | J_f, M_f) [S_{J_i J_C}(J_B)]^{1/2} [S_{J_f J_C}(J_{B'})]^{1/2} \\
 &\quad \times \int d^4x \Psi_{J_{B'} M_{B'}}^\dagger(x) \Gamma_{S_{11}} \Psi_{J_B M_B}(x) \Phi_\eta^*(x) e^{-ik_\gamma \cdot x}
 \end{aligned} \tag{2.47}$$

where  $\Gamma_{S_{11}}$  is a  $4 \times 4$  matrix operator that can be written as

$$\Gamma_{S_{11}} = \frac{g_{\eta NR} \kappa_p^R}{M + M_R} \gamma_0 \left\{ \frac{k_s + M_R}{k_s^2 - M_R^2} \gamma_5 \not{k}_\gamma \not{\epsilon}_r + \gamma_5 \not{k}_\gamma \not{\epsilon}_r \frac{k_u + M_R}{k_u^2 - M_R^2} \right\} \tag{2.48}$$

The  $\gamma_0$  comes from writing the  $\bar{u}_{J_{B'} M_{B'}}(y)$  factor in (2.44) as

$$\bar{u}_{J_{B'} M_{B'}}(y) = \Psi_{J_{B'} M_{B'}}^\dagger(y) \gamma_0 \tag{2.49}$$

where  $\Psi_{J_{B'} M_{B'}}(y)$  is just the configuration space wavefunction of the final bound proton. This proton will be denoted by the subscript  $p'$ . Similarly,  $\Psi_{J_B M_B}(x)$  corresponds to the initial bound proton, which will be denoted by the subscript  $p$ . In (2.48), we have also used the momenta

$$k_s = k_\eta + k_{p'} \tag{2.50}$$

and

$$k_u = k_{p'} - k_\gamma \tag{2.51}$$

to represent  $k_R$  for the two terms in (2.33).

The structure of the total reaction amplitude,  $S_{fi}$ , is the same as for  $S_{fi}^R$  in (2.47) except for  $\Gamma_{S_{11}}$ , which is replaced by a different  $\Gamma$  operator for every pair of  $\mathcal{L}_{\text{INT}}$  terms that contribute. We would then have

$$S_{fi} = \sum_{\text{All interactions } (j)} S_{fi}^{(j)} \quad (2.52)$$

For completeness, we will now list the remainder of the  $\Gamma$  operators [17].

$$\begin{aligned} \Gamma_{\text{proton}} = g_{\eta NN} \gamma_0 & \left\{ \gamma_5 \frac{\not{k}_s + M}{k_s^2 - M^2} \left( \frac{\kappa_p}{2M} \not{k}_\gamma + 1 \right) \not{\epsilon}_r \right. \\ & \left. + \left( \frac{\kappa_p}{2M} \not{k}_\gamma + 1 \right) \not{\epsilon}_r \frac{\not{k}_u + M}{k_u^2 - M^2} \gamma_5 \right\} \end{aligned} \quad (2.53)$$

$$\Gamma_{P_{11}} = \frac{g_{\eta NR} \kappa_p^R}{M + M_R} \gamma_0 \left\{ \gamma_5 \frac{\not{k}_s + M_R}{k_s^2 - M_R^2} \not{k}_\gamma \not{\epsilon}_r + \not{k}_\gamma \not{\epsilon}_r \frac{\not{k}_u + M_R}{k_u^2 - M_R^2} \gamma_5 \right\} \quad (2.54)$$

$$\Gamma_V = \frac{\lambda_t g_t}{2M m_\eta} \epsilon_{\mu\nu\lambda\sigma} \gamma_0 \frac{\epsilon^\mu k_\gamma^\nu \sigma^{\sigma\alpha} k_{t\alpha} k_\eta^\lambda}{k_t^2 - m_V^2} - i \frac{\lambda_v g_v}{m_\eta} \epsilon_{\mu\nu\lambda\sigma} \gamma_0 \frac{\epsilon^\mu k_\gamma^\nu k_\eta^\lambda \gamma^\sigma}{k_t^2 - m_V^2} \quad (2.55)$$

$$\begin{aligned} \Gamma_{D_{13}}^{(1)} = -\frac{f_{\eta NR} \kappa_R^{(1)}}{2M m_\eta} \gamma_0 & \left\{ \gamma_5 k_\eta^\nu \theta_{\nu\mu}(Z) \frac{\not{k}_s + M_R}{k_s^2 - M_R^2} P^{\mu\alpha} \theta_{\alpha\beta}(Y) \gamma_\lambda (k_\gamma^\beta \epsilon_r^\lambda - \epsilon_r^\beta k_\gamma^\lambda) \right. \\ & \left. + \gamma_\lambda \theta_{\beta\alpha}(Y) (k_\gamma^\beta \epsilon_r^\lambda - \epsilon_r^\beta k_\gamma^\lambda) \frac{\not{k}_u + M_R}{k_u^2 - M_R^2} P^{\alpha\mu} \theta_{\mu\nu}(Z) k_\eta^\nu \gamma_5 \right\} \end{aligned} \quad (2.56)$$

$$\begin{aligned} \Gamma_{D_{13}}^{(2)} = -\frac{f_{\eta NR} \kappa_R^{(2)}}{4m_\eta M^2} \gamma_0 & \left\{ \gamma_5 k_\eta^\nu \theta_{\nu\mu}(Z) \frac{\not{k}_s + M_R}{k_s^2 - M_R^2} P^{\mu\alpha} \theta_{\alpha\beta}(X) (k_\gamma^\beta \epsilon_r^\lambda - \epsilon_r^\beta k_\gamma^\lambda) (k_p)_\lambda \right. \\ & \left. + (k_{p'})_\lambda \theta_{\beta\alpha}(X) (k_\gamma^\beta \epsilon_r^\lambda - \epsilon_r^\beta k_\gamma^\lambda) \frac{\not{k}_u + M_R}{k_u^2 - M_R^2} P^{\alpha\mu} \theta_{\mu\nu}(Z) k_\eta^\nu \gamma_5 \right\} \end{aligned} \quad (2.57)$$

where

$$\theta_{\mu\nu}(V) \equiv g_{\mu\nu} + \left[ -\frac{1}{2} (1 + 4V) + V \right] \gamma_\mu \gamma_\nu \quad (2.58)$$

for  $V = X, Y, Z$  and

$$P^{\mu\nu} \equiv \left( g^{\mu\nu} - \frac{1}{3} \gamma^\mu \gamma^\nu - \frac{1}{2M_R} [\gamma^\mu k_\gamma^\nu - \gamma^\nu k_\gamma^\mu] - \frac{2}{3M_R^2} k_\gamma^\mu k_\gamma^\nu \right) \quad (2.59)$$

The quantities  $M$ ,  $M_R$ ,  $m_\eta$ , and  $m_V$  represent the masses of the nucleon, the appropriate nucleon resonance, the  $\eta$  meson, and the appropriate vector meson, respectively. In equation (2.53),  $\kappa_p$  is the anomalous magnetic moment of the proton. In equation (2.55), the four-momentum  $k_t$  is defined by

$$k_t = k_\gamma - k_\eta \quad (2.60)$$

The quantities  $g_{\eta NN}$ ,  $g_{\eta NR}$ ,  $\kappa_p^R$ ,  $\lambda_t$ ,  $g_t$ ,  $\lambda_v$ ,  $g_v$ ,  $f_{\eta NR} \kappa_R^{(1)}$  and  $f_{\eta NR} \kappa_R^{(2)}$  are the phenomenological parameters of the effective Lagrangian.

## 2.4 Feynman Rules

In the previous section, we saw how QFT can be used to write the reaction amplitude for an incoherent  $\eta$ -photoproduction reaction. The required steps, though straightforward, are tedious, so in this section I will present Feynman rules with which we can quickly write expressions for the various terms of  $S_{fi}$ .

We start by looking at Feynman diagrams. In the absence of any knowledge about the detailed form of the interactions, we would have, for the elementary process  $\gamma + N \rightarrow \eta + N$ , a Feynman diagram as in Figure 2.1.

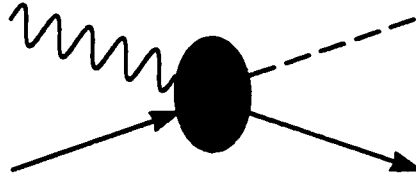


Figure 2.1: Feynman diagram for a  $\gamma + N \rightarrow \eta + N$  reaction

The interaction Lagrangian specifies the detailed form of the interactions. All of the terms in our interaction Lagrangian contain three field operators, and so each vertex in our diagrams will connect three lines.  $F^{\mu\nu}$  represents a photon line (which will be drawn as a wavy line),  $V^{\mu\nu}$  a vector meson line (coiled line), and  $\eta$  represents an eta meson line (dotted line). For the fermions,  $\psi$  represents a nucleon travelling into a vertex and  $\bar{\psi}$  represents a nucleon travelling away from a vertex. Both will be represented by a solid line with an arrow to specify direction. Similarly,  $R$  and  $\bar{R}$  represent resonances travelling to and away from a vertex, and these will be represented by thick solid lines with arrows.

For each of the  $\mathcal{L}_{\text{INT}}$  terms, we can now draw a simple vertex. The vertex factors can be obtained by removing the field operators in  $\mathcal{L}_{\text{INT}}$ . For example, (2.5) gives

$$\mathcal{L}_{\eta NN} = -ig_{\eta NN}\bar{\psi}\gamma_5\psi\eta$$

which represents the vertex shown in Figure 2.2 with a vertex factor of  $-ig_{\eta NN}\gamma_5$ .

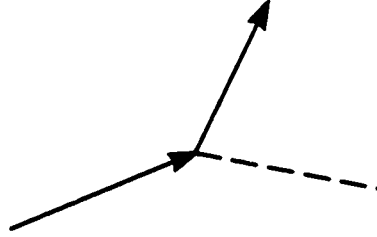


Figure 2.2: The vertex specified by  $\mathcal{L}_{\eta NN}$

The next step consists of drawing all the possible Feynman diagrams, to any given order, that are consistent with Figure 2.1, using the  $\mathcal{L}_{\text{INT}}$  terms available. Since we will be working in configuration space, each vertex must be labeled by a spacetime coordinate. We will use  $x$  and  $y$ , and it will turn out to be a trivial

detail once we encounter  $\delta^4(x - y)$  factors in the propagators. To lowest order, which turns out to be second order in our case, we have five distinct types of diagrams, as shown in Figure 2.3.

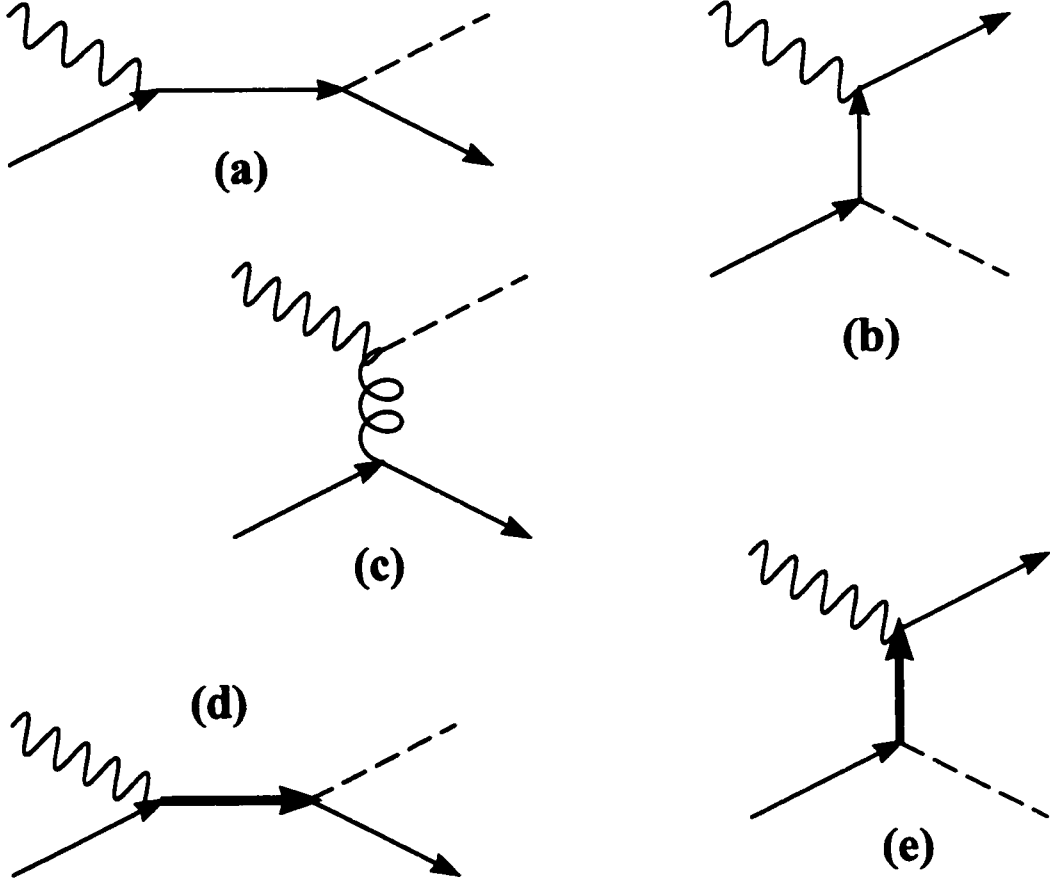


Figure 2.3: The contributing Feynman diagrams to the  $\gamma + N \rightarrow \eta + N$  reaction

Diagrams (a) and (b) are the s- and u-channel Born diagrams that use  $\mathcal{L}_{\eta NN}$  and  $\mathcal{L}_{\gamma NN}$ . Diagram (c) is the t-channel vector meson diagram that uses  $\mathcal{L}_{VNN}$  and  $\mathcal{L}_{V\eta\gamma}$ . Diagrams (d) and (e) are the s- and u-channel resonance diagrams that use  $\mathcal{L}_{\eta NR}$  and  $\mathcal{L}_{\gamma NR}$ . We will have these two diagrams for each of the resonances under consideration.

The propagator for a spin- $\frac{1}{2}$  resonance is given by (2.46) as

$$i \frac{\not{k}_R + M_R}{k_R^2 - M_R^2} \delta^4(x - y)$$

We can also use this expression for the nucleon propagator that will be required in diagrams (a) and (b). The vector meson propagator needed in diagram (c) is  $i\Delta_F(x - y)$  which, in the plane wave approximation, becomes

$$i \frac{\delta^4(x - y)}{k_v^2 - M_v^2} \left( g_{\mu\nu} - \frac{k_{v\mu} k_{v\nu}}{M_v^2} \right) \quad (2.61)$$

The spin- $\frac{3}{2}$  resonance propagator presents an assortment of complications, as is evidenced by the form of equations (2.56) and (2.57) for  $\Gamma_{D_{13}}$ .

The second quantized forms of the fields we encountered in the last section suggest the method with which we can account for external lines attached to a vertex at  $x$ . For an outgoing  $\eta$  meson with four-momentum  $k_\eta$ , include a factor of

$$\frac{1}{(2\pi)^{3/2}} \frac{1}{\sqrt{2E_\eta}} \Phi^*(k_\eta, x) \quad (2.62)$$

For an incoming photon with polarization  $\epsilon_r$  and four-momentum  $k_\gamma$ , attached to a vertex whose interaction Lagrangian contains  $F^{\mu\nu}$ , include a factor of

$$\frac{1}{(2\pi)^{3/2}} \frac{1}{\sqrt{2E_\gamma}} \left( k_\gamma^\mu \epsilon_r^\nu - k_\gamma^\nu \epsilon_r^\mu \right) e^{-ik_\gamma \cdot x} \quad (2.63)$$

If the  $\mathcal{L}_{\text{INT}}$  term defining the vertex contains  $A^\mu$ , include a factor of

$$\frac{1}{(2\pi)^{3/2}} \frac{1}{\sqrt{2E_\gamma}} \epsilon_r^\mu e^{-ik_\gamma \cdot x} \quad (2.64)$$

For  $\mathcal{L}_{\gamma NN}$ , which contains a term with  $A^\mu$  and a term with  $F^{\mu\nu}$  due to the anomalous magnetic moment of a nucleon, treat the two terms as separate interactions, electric and magnetic and add the contributions. For a free outgoing nucleon

with four-momentum  $k_{p'}$  and spin  $s_f$ , include a factor of

$$\frac{1}{(2\pi)^{3/2}} \sqrt{\frac{M}{E_{p'}}} \bar{u}_{s_f}(k_{p'}, x) \quad (2.65)$$

Note that this does not occur in an incoherent reaction, but we include it for completeness. For a bound final-state nucleon with angular momentum quantum numbers  $J_{B'}$  and  $M_{B'}$ , include a factor of

$$\sum_{J_{B'} M_{B'}} (J_C, J_{B'}; M_C, M_{B'} | J_f, M_f) [S_{J_f J_C}(J_{B'})]^{1/2} \bar{u}_{J_{B'} M_{B'}}(x) \quad (2.66)$$

Similarly, for a bound initial-state nucleon, include a factor of

$$\sum_{J_B M_B} (J_C, J_B; M_C, M_B | J_i, M_i) [S_{J_i J_C}(J_B)]^{1/2} u_{J_B M_B}(x) \quad (2.67)$$

Take care to arrange these nucleon factors so that  $\bar{u}$  is at the beginning and  $u$  is at the end of the entire expression for  $S_{fi}$ .

For two-vertex diagrams, include a factor of  $i^2 = -1$  and integrate over all possible positions of the vertices:  $\int \int d^4x d^4y$ . In this context, we do not need to specify rules for loops since it is apparent that this effective field theory will no longer be valid at sufficiently high energies. As a result, we would only consider tree level contributions and acknowledge the impossibility of calculating higher-order corrections using this model.

## 2.5 Observables

Having derived an expression for the reaction amplitude, which we will write for a general diagram as

$$\begin{aligned} S_{fi} = & \frac{e}{(2\pi)^3} \sqrt{\frac{1}{2E_\eta 2E_\gamma}} \sum_{J_C J_B M_B} \sum_{J_{B'} M_{B'}} (J_C, J_B; M_C, M_B | J_i, M_i) \\ & \times (J_C, J_{B'}; M_C, M_{B'} | J_f, M_f) [S_{J_i J_C}(J_B)]^{1/2} [S_{J_f J_C}(J_{B'})]^{1/2} \\ & \times \int d^4x \Psi_{J_{B'} M_{B'}}^\dagger(x) \Gamma \Psi_{J_B M_B}(x) \Phi_\eta^*(x) e^{-ik_\gamma \cdot x} \end{aligned} \quad (2.68)$$



we must now relate it to quantities that are experimentally observable.

### 2.5.1 Preliminary Simplifications

Since none of our interactions are time-dependent, we can factor the wavefunctions  $\Psi_{J_{B'}M_{B'}}^\dagger(x)$ ,  $\Psi_{J_B M_B}(x)$ ,  $\Phi_\eta^*(x)$  and  $e^{-i\mathbf{k}_\gamma \cdot \mathbf{x}}$  into spatial and temporal parts:

$$\begin{aligned}\Psi_{J_{B'}M_{B'}}^\dagger(x) &= e^{iE_{B'}t} \psi_{J_{B'}M_{B'}}^\dagger(\vec{x}) \\ \Psi_{J_B M_B}(x) &= e^{-iE_B t} \psi_{J_B M_B}(\vec{x}) \\ \Phi_\eta^*(x) &= e^{iE_\eta t} \varphi_\eta^*(\vec{x}) \\ e^{-i\mathbf{k}_\gamma \cdot \mathbf{x}} &= e^{-iE_\gamma t} e^{i\vec{k}_\gamma \cdot \vec{x}}\end{aligned}\tag{2.69}$$

Using (2.69) we can perform the temporal integration in (2.68),

$$\int dx_0 e^{i(E_{B'}+E_\eta-E_B-E_\gamma)t} = 2\pi\delta(E_{B'}+E_\eta-E_B-E_\gamma)\tag{2.70}$$

so that the reaction amplitude can now be written as

$$\begin{aligned}S_{fi} &= \frac{e}{(2\pi)^2} \sqrt{\frac{1}{2E_\eta 2E_\gamma}} \delta(E_{B'}+E_\eta-E_B-E_\gamma) \\ &\times \sum_{J_C J_B M_B} \sum_{J_{B'} M_{B'}} (J_C, J_B; M_C, M_B | J_i, M_i) \\ &\times (J_C, J_{B'}; M_C, M_{B'} | J_f, M_f) [S_{J_i J_C}(J_B)]^{1/2} [S_{J_f J_C}(J_{B'})]^{1/2} \\ &\times \int d^3x \psi_{J_{B'}M_{B'}}^\dagger(\vec{x}) \Gamma \psi_{J_B M_B}(\vec{x}) \varphi_\eta^*(\vec{x}) e^{i\vec{k}_\gamma \cdot \vec{x}}\end{aligned}\tag{2.71}$$

Before we proceed further, we will find it convenient to define the integral in (2.71) as

$$\mathcal{Z} \equiv \int d^3x \psi_{J_{B'}M_{B'}}^\dagger(\vec{x}) \Gamma \psi_{J_B M_B}(\vec{x}) \varphi_\eta^*(\vec{x}) e^{i\vec{k}_\gamma \cdot \vec{x}}\tag{2.72}$$

### 2.5.2 Fermi's Golden Rule

In any photoproduction reaction, the principal fundamental observable quantity is the differential cross section. Fermi's Golden Rule relates the differential cross section to the reaction amplitude:

$$d\sigma = \frac{|S_{fi}|^2}{T J_{inc}} d^3 \vec{p}_\eta \quad (2.73)$$

The factor of  $T$  in the denominator of (2.73) is usually taken to be the time period of the interaction. When we square the  $\delta(E_f - E_i)$  factor in (2.71), we can cancel the factor of  $T$  by making use of the relation [25]

$$[\delta(E_f - E_i)]^2 = \frac{T}{2\pi} \delta(E_f - E_i) \quad (2.74)$$

The  $J_{inc}$  in (2.73) refers to the incident flux. In the laboratory frame, where the target nucleus is initially at rest and the photon is incident at the speed of light, we have

$$J_{inc} = \frac{1}{(2\pi)^3} \quad (2.75)$$

By defining

$$\mathcal{A} \equiv \sum_{J_C J_B M_B} (J_C, J_B; M_C, M_B | J_i, M_i) [S_{J_i J_C}(J_B)]^{1/2} \quad (2.76)$$

$$\mathcal{B} \equiv \sum_{J_{B'} M_{B'}} (J_C, J_{B'}; M_C, M_{B'} | J_f, M_f) [S_{J_f J_C}(J_{B'})]^{1/2} \quad (2.77)$$

as operators that act on  $\mathcal{Z}$ , we can rewrite (2.73), using (2.71), (2.72), (2.74), and (2.75) as

$$d\sigma = \frac{e^2}{16\pi^2 E_\eta E_\gamma} \delta(E_{B'} + E_\eta - E_B - E_\gamma) |\mathcal{A} \mathcal{B} \mathcal{Z}|^2 d^3 \vec{p}_\eta \quad (2.78)$$

or, using the dimensionless fine structure constant  $\alpha = \frac{e^2}{4\pi}$ ,

$$d\sigma = \frac{\alpha}{4\pi E_\eta E_\gamma} \delta(E_{B'} + E_\eta - E_B - E_\gamma) |\mathcal{A} \mathcal{B} \mathcal{Z}|^2 d^3 \vec{p}_\eta \quad (2.79)$$

### 2.5.3 The Recoil Factor

We will write the phase space factor  $d^3\vec{p}_\eta$  in spherical coordinates:

$$d^3\vec{p}_\eta = p_\eta^2 dp_\eta d\Omega_\eta \quad (2.80)$$

Since

$$E_\eta^2 = p_\eta^2 + m_\eta^2 \quad (2.81)$$

we have

$$2E_\eta dE_\eta = 2p_\eta dp_\eta \quad (2.82)$$

which allows us to rewrite (2.80) as

$$d^3\vec{p}_\eta = p_\eta E_\eta dE_\eta d\Omega_\eta \quad (2.83)$$

Combining (2.83) with (2.79), we obtain

$$\frac{d\sigma}{d\Omega_\eta} = \frac{\alpha}{4\pi E_\gamma} p_\eta \delta(E_{B'} + E_\eta - E_B - E_\gamma) |\mathcal{ABZ}|^2 dE_\eta \quad (2.84)$$

We would now like to integrate over  $E_\eta$ . At first glance, the  $\delta$ -function in (2.84) seems to make this integration trivial, but we must take note that the other energies are not all independent of  $E_\eta$ . Based on the  $\delta$ -function identity

$$\delta(f(x)) = \sum_i \frac{1}{f'(x_i)} \delta(x - x_i) \quad (2.85)$$

where  $f(x_i) = 0$ , we define the recoil factor

$$R \equiv \frac{\partial}{\partial E_\eta} (E_{B'} + E_\eta - E_B - E_\gamma) \quad (2.86)$$

With the recoil factor, the differential cross section (2.84) can be written as

$$\frac{d\sigma}{d\Omega_\eta} = \frac{\alpha}{4\pi E_\gamma R} p_\eta |\mathcal{ABZ}|^2 \quad (2.87)$$

Now we will derive an explicit expression for the recoil factor in (2.87). The  $\delta$ -function from which this factor originates serves to enforce energy conservation. In order to model the reaction more accurately, we will now allow a momentum transfer to the core of the nucleus during the reaction so that the more general energy conservation law follows from a factor of

$$\delta(E_\eta + E_R - E_T - E_\gamma) \quad (2.88)$$

where  $E_R$  is the energy of the recoiling nucleus and  $E_T$  is the energy of the target. Since the target is assumed to be stationary in the laboratory frame, we have

$$\vec{p}_\gamma = \vec{p}_R + \vec{p}_\eta \quad (2.89)$$

which leads to

$$p_R^2 = p_\gamma^2 + p_\eta^2 - 2\vec{p}_\eta \cdot \vec{p}_\gamma \quad (2.90)$$

and with  $\vec{p}_\eta \cdot \vec{p}_\gamma = p_\eta p_\gamma \cos \theta_\eta$  we can differentiate both sides of (2.90) with respect to  $p_\eta$ :

$$2p_R \frac{\partial p_R}{\partial p_\eta} = 2p_\eta - 2p_\gamma \cos \theta_\eta \quad (2.91)$$

$$\frac{\partial p_R}{\partial p_\eta} = \frac{p_\eta}{p_R} - \frac{p_\gamma}{p_R} \cos \theta_\eta \quad (2.92)$$

The recoil factor in (2.86) is defined in terms of a partial derivative with respect to  $E_\eta$  and not  $p_\eta$ , so we use (2.82) and

$$2E_R dE_R = 2p_R dp_R \quad (2.93)$$

to write

$$\frac{\partial E_R}{\partial E_\eta} = \frac{p_R dp_R / E_R}{p_\eta dp_\eta / E_\eta} \quad (2.94)$$

so that

$$R = 1 + \frac{E_\eta p_R}{E_R p_\eta} \frac{\partial p_R}{\partial p_\eta} \quad (2.95)$$

Inserting (2.92) into (2.95) we obtain the final form of the recoil factor:

$$R = 1 + \frac{E_\eta}{E_R} \left( 1 - \frac{p_\gamma}{p_\eta} \cos \theta_\eta \right) \quad (2.96)$$

### 2.5.4 Spin Summations

Now we are in a position to simplify the  $|\mathcal{ABZ}|^2$  factor in (2.87). If we do not specify or detect the spin states of the incident photon, the target nucleus, and the recoiling nucleus, then we must average over the spin states of the initial particles and sum over the spin states of the final particles. Since the photon has two possible spin states, as labelled by  $\xi$ , and the spin- $J_i$  target nucleus has  $(2J_i + 1)$  possible spin states, our differential cross section now takes the form

$$\frac{d\sigma}{d\Omega_\eta} = \frac{1}{2(2J_i + 1)} \sum_{M_i, M_f, \xi} \frac{\alpha}{4\pi E_\gamma R} p_\eta |\mathcal{ABZ}|^2 \quad (2.97)$$

The only part of  $|\mathcal{ABZ}|^2$  that depends on  $M_i$  is the Clebsch-Gordan coefficient in  $\mathcal{A}$ . Similarly, the Clebsch-Gordan coefficient in  $\mathcal{B}$  has the only  $M_f$  dependence. Therefore, we need to evaluate

$$\mathcal{Q} \equiv \sum_{M_i} (J_C, K_B; M_C, N_B | J_i, M_i) (J_C, J_B; M_C, M_B | J_i, M_i) \quad (2.98)$$

Note that  $K_B$  and  $N_B$  are the dummy indices of summation resulting from  $\mathcal{A}^* \mathcal{A}$ . Also, we can ignore the complex conjugation since Clebsch-Gordan coefficients are defined to be real. Now we will use some of the symmetry relations that govern Clebsch-Gordan coefficients [26] in order to evaluate  $\mathcal{Q}$ . Using

$$(J_1, J_2; M_1, M_2 | J_3, M_3) = (-1)^{J_1 - M_1} \left[ \frac{2J_3 + 1}{2J_2 + 1} \right]^{\frac{1}{2}} (J_1, J_3; M_1, -M_3 | J_2, -M_2) \quad (2.99)$$

and the fact that  $J_C$  and  $M_C$  differ by an integer so that  $(-1)^{2(J_C - M_C)} = 1$ , we have

$$\begin{aligned} \mathcal{Q} = & \sum_{M_i} \frac{2J_i + 1}{\sqrt{2K_B + 1} \sqrt{2J_B + 1}} \\ & \times (J_C, J_i; M_C, -M_i | K_B, -N_B) (J_C, J_i; M_C, -M_i | J_B, -M_B) \end{aligned} \quad (2.100)$$

Clebsch-Gordan coefficients obey the following orthogonality relation:

$$\sum_{M_1, M_2} (J_1, J_2; M_1, M_2 | J, M) (J_1, J_2; M_1, M_2 | J', M') = \delta_{J, J'} \delta_{M, M'} \quad (2.101)$$

Applying (2.101) to (2.100), we find that  $\mathcal{Q} = 0$  unless both

$$N_B = M_B \quad (2.102)$$

and

$$K_B = J_B \quad (2.103)$$

are satisfied. This allows us to rewrite (2.100) as

$$\mathcal{Q} = \frac{2J_i + 1}{2J_B + 1} \quad (2.104)$$

Applying (2.104) to both the  $M_i$  and  $M_f$  summations in (2.97), we have

$$\frac{d\sigma}{d\Omega_\eta} = \frac{\alpha}{8\pi} \frac{(2J_f + 1)}{R} \frac{p_\eta}{E_\gamma} \sum_{J_B, M_B} \sum_{J_{B'}, M_{B'}} \sum_{\xi} \frac{\mathcal{S}_{J_i J_C}(J_B)}{(2J_B + 1)} \frac{\mathcal{S}_{J_f J_C}(J_{B'})}{(2J_{B'} + 1)} |\mathcal{Z}|^2 \quad (2.105)$$

where  $\mathcal{Z}$  depends on  $M_B, M_{B'}$ , and  $\xi$ .

### 2.5.5 Units

Throughout the derivations of  $S_{fi}$  and  $d\sigma$ , we have been using natural units, wherein  $\hbar = c = 1$ . Now we must examine the dimensions of the various factors in (2.105) so that we can restore any necessary factors of  $\hbar$  and  $c$ .

The differential cross section,  $d\sigma$ , has dimensions of area, or length squared. Since  $\Omega_\eta$  is measured in steradians, which are dimensionless, the left side of (2.105) has dimensions of length squared. On the right side,  $\alpha$ ,  $J_f$ ,  $J_B$ ,  $J_{B'}$ , and  $R$  are all dimensionless, as are the spectroscopic factors  $\mathcal{S}_{J_i J_C}(J_B)$  and  $\mathcal{S}_{J_f J_C}(J_{B'})$ . The ratio  $\frac{p_\eta}{E_\gamma}$  is also dimensionless if we measure both  $p_\eta$  and  $E_\gamma$  in the same units. To remind us of this, we will multiply  $p_\eta$  by a factor  $c$ . Looking at (2.72), we see that  $\mathcal{Z}$  is the spatial integral of two continuum particle wavefunctions times two bound state nucleon wave functions that sandwich a  $\Gamma$  operator. The continuum wavefunctions,  $\varphi_\eta^*(\vec{x})$  and  $e^{-i\vec{k}_\gamma \cdot \vec{x}}$ , are dimensionless. The bound state wave functions,  $\psi_{J_{B'}, M_{B'}}^\dagger(\vec{x})$  and  $\psi_{J_B M_B}(\vec{x})$ , are normalized so that their combined dimensions cancel the dimensions introduced by the spatial integration. Looking at (2.48), we see that if we calculate all  $k$  and  $M$  quantities with dimensions of inverse length, then  $\Gamma$  will have dimensions of length. As a result, the right side of (2.105) will have dimensions of length squared without the need for any other additional factors of  $\hbar$  or  $c$ .

### 2.5.6 Final Form of the Observables

Given the discussion in the previous section, we can rewrite the differential cross section (2.105) as

$$\frac{d\sigma}{d\Omega_\eta} = \frac{\alpha}{8\pi} \frac{(2J_f + 1)}{R} \frac{p_\eta c}{E_\gamma} \sum_{J_B, M_B} \sum_{J_{B'}, M_{B'}} \sum_{\xi} \frac{\mathcal{S}_{J_i J_C}(J_B)}{(2J_B + 1)} \frac{\mathcal{S}_{J_f J_C}(J_{B'})}{(2J_{B'} + 1)} |\mathcal{Z}|^2 \quad (2.106)$$

$\frac{d\sigma}{d\Omega_\eta}$ , as a function of  $\theta_\eta$ , will be one of the observables of interest to us. We are also interested in the total cross section, which is easily obtained by integrating (2.106) over  $d\Omega_\eta$ . Since the initial configuration of the system possesses azimuthal symmetry, we can use

$$d\Omega_\eta = \sin \theta_\eta d\theta_\eta d\phi_\eta \quad (2.107)$$

and integrate (2.106) over  $\phi_\eta$  by multiplying by a factor of  $2\pi$ . This yields

$$\sigma = 2\pi \int \frac{d\sigma}{d\Omega_\eta} \sin \theta_\eta d\theta_\eta \quad (2.108)$$

The last observable that we will calculate is the photon asymmetry. If we take the two independent spin states of the photon, as indexed by  $\xi$ , to be linear polarization states parallel and perpendicular to the reaction plane defined by  $\vec{p}_\gamma$  and  $\vec{p}_\eta$ , we can remove  $\frac{1}{2} \sum_\xi$  from (2.106) and calculate

$$d\sigma_{\parallel} \equiv \left( \frac{d\sigma}{d\Omega_\eta} \right)_{\xi_{\parallel}} \quad (2.109)$$

and

$$d\sigma_{\perp} \equiv \left( \frac{d\sigma}{d\Omega_\eta} \right)_{\xi_{\perp}} \quad (2.110)$$

Hence, we define the photon asymmetry to be

$$A \equiv \frac{d\sigma_{\parallel} - d\sigma_{\perp}}{d\sigma_{\parallel} + d\sigma_{\perp}} \quad (2.111)$$



## Appendix 2.A Gauge Invariance

In this appendix we address the conditions under which the reaction amplitude is gauge invariant.

As a starting point, we observe that the effective Lagrangian with which we begin is explicitly gauge invariant. For example,

$$\mathcal{L}_{\gamma NN} = -e\bar{\psi}\gamma_\mu A^\mu\psi - \frac{e\kappa_p}{4M}\bar{\psi}\sigma_{\mu\nu}F^{\mu\nu}\psi \quad (2.112)$$

when combined with the free Lagrangian terms for the fields  $\psi$  and  $A^\mu$ , is invariant under the local gauge transformation

$$A^\mu \longrightarrow A^\mu + \partial^\mu\lambda \quad (2.113)$$

$$\psi \longrightarrow e^{-iq\lambda}\psi \quad (2.114)$$

The reaction amplitude,

$$S_{fi}^{(j)} \sim \int d^4x \Psi_{J_{B'}M_{B'}}^\dagger(x) \Gamma_{(j)} \Psi_{J_B M_B}(x) \Phi_\eta^*(x) e^{-ik_\gamma \cdot x} \quad (2.115)$$

is gauge invariant if and only if the operator  $\Gamma_{(j)}$  is gauge invariant. We will now show that all the  $\Gamma_{(j)}$  operators are gauge invariant except for the part of the operator that arises from the first term of  $\mathcal{L}_{\gamma NN}$ , commonly referred to as the electric term.

Observe that whenever a term in the interaction Lagrangian contains  $F^{\mu\nu}$ , the subsequent Fock space calculation leads to a factor of the form

$$\{k_\gamma^\mu \epsilon^\nu - k_\gamma^\nu \epsilon^\mu\} \quad (2.116)$$

as was shown in equation (2.38).

To test gauge invariance, we note that

$$\epsilon \longrightarrow \epsilon + ak_\gamma \quad (2.117)$$

is the general gauge transformation that preserves the Lorentz condition

$$\epsilon \cdot k_\gamma = 0 \quad (2.118)$$

since  $k_\gamma \cdot k_\gamma$  vanishes for the massless photon. When we have an expression involving  $\epsilon$  and  $k_\gamma$ , such as (2.116), we test gauge invariance by showing that the transformation (2.117) leaves the expression unchanged. This is equivalent to making the substitution

$$\epsilon \longrightarrow k_\gamma \quad (2.119)$$

with the requirement that the resulting expression equal zero. By using (2.119) on (2.116), we conclude that all operators arising from Lagrangian terms containing  $F^{\mu\nu}$  are gauge invariant.

The electric term,

$$\mathcal{L}_{el} = -e\bar{\psi}\gamma_\mu A^\mu\psi \quad (2.120)$$

does not contain  $F^{\mu\nu}$ , so the Fock space calculations alone do not guarantee that gauge invariance is maintained. The terms in the  $\Gamma$  operator that arise from (2.120) are

$$\Gamma_{el} = g_{\eta NN}\gamma_0 \left[ \gamma_5 \frac{\not{k}_s + M}{k_s^2 - M^2} \not{\epsilon} + \not{\epsilon} \frac{\not{k}_u + M}{k_u^2 - M^2} \gamma_5 \right] \quad (2.121)$$

Using  $k_s = k_\gamma + k_i$  and  $k_u = k_f + k_\gamma$ , where  $k_i$  and  $k_f$  represent the initial and final nucleons, along with (2.119), we have

$$\Gamma_{el} = g_{\eta NN}\gamma_0 \left[ \gamma_5 \frac{\not{k}_\gamma + \not{k}_i + M}{k_\gamma^2 + k_i^2 + 2k_\gamma \cdot k_i - M^2} \not{k}_\gamma + \not{k}_\gamma \frac{-\not{k}_\gamma + \not{k}_f + M}{k_\gamma^2 + k_f^2 - 2k_\gamma \cdot k_f - M^2} \gamma_5 \right] \quad (2.122)$$

We can use  $\not{k}_\gamma \not{k}_\gamma = 0$  and  $k_\gamma^2 = 0$  to simplify this expression. Also, suppose that the initial and final nucleons are on mass shell, so that  $k_i^2 - M^2 = 0$  and  $k_f^2 - M^2 = 0$ . This allows us to write (2.122) as

$$\Gamma_{el} = g_{\eta NN}\gamma_0 \left[ \gamma_5 \frac{\not{k}_i + M}{2k_\gamma \cdot k_i} \not{k}_\gamma + \not{k}_\gamma \frac{\not{k}_f + M}{-2k_\gamma \cdot k_f} \gamma_5 \right] \quad (2.123)$$

$\not{k}_\gamma$  commutes with  $M$  and almost anticommutes with  $\not{k}_i$ :

$$\begin{aligned}\not{k}_i \not{k}_\gamma &= k_{i\mu} k_{\gamma\nu} \gamma^\mu \gamma^\nu \\ &= k_{i\mu} k_{\gamma\nu} [2g^{\mu\nu} - \gamma^\nu \gamma^\mu] \\ &= 2k_i \cdot k_\gamma - \not{k}_\gamma \not{k}_i\end{aligned}\tag{2.124}$$

Similarly,

$$\not{k}_\gamma \not{k}_f = 2k_\gamma \cdot k_f - \not{k}_f \not{k}_\gamma\tag{2.125}$$

so that

$$\begin{aligned}\Gamma_{el} &= g_{\eta NN} \gamma_0 \left[ -\gamma_5 \not{k}_\gamma \frac{\not{k}_i - M}{2k_\gamma \cdot k_i} + \gamma_5 + \frac{\not{k}_f - M}{2k_\gamma \cdot k_f} \not{k}_\gamma \gamma_5 - \gamma_5 \right] \\ &= g_{\eta NN} \gamma_0 \left[ -\gamma_5 \not{k}_\gamma \frac{\not{k}_i - M}{2k_\gamma \cdot k_i} + \frac{\not{k}_f - M}{2k_\gamma \cdot k_f} \not{k}_\gamma \gamma_5 \right]\end{aligned}\tag{2.126}$$

In the limit of vanishing nuclear potentials, the initial and final nucleons are governed by the Dirac equation for a free particle of mass  $M$ :

$$\bar{\Psi}_f (\not{k}_f - M) = 0\tag{2.127}$$

$$(\not{k}_i - M) \Psi_i = 0\tag{2.128}$$

Since we have  $\Psi_f^\dagger \Gamma \Psi_i$  in equation (2.115) for  $S_{fi}$ , the first term of (2.126) vanishes due to (2.128) and the second term vanishes due to (2.127).

To summarize, we have shown that almost all the parts of the reaction amplitude are explicitly gauge invariant. One part, which turns out to be a very small part of the amplitude, is only gauge invariant if the initial and final nucleons are on mass shell and if the nuclear potentials can be neglected so that the initial and final nucleons are well described by a free Dirac equation.

# Chapter 3

## Details of the Calculation

In the previous chapter we derived formal expressions for the reaction amplitude and the observables that arise in an incoherent  $\eta$ -photoproduction reaction. Our ultimate goal is to perform numerical calculations for the observables. To do this, we need to take a closer look at our analytic expressions so that we can eventually break such a numerical calculation down into manageable pieces. In this section we will examine the steps that are taken in order to transform the analytic expressions for the observables into simpler pieces for which we can write computer code.

### 3.1 Kinematics

There are two perspectives from which we can look at the kinematics of our reaction. From one perspective, our reaction is of the form

$$A + B \longrightarrow C + D \tag{3.1}$$

where  $A$  is the incident photon,  $B$  is the target nucleus,  $C$  is the eta meson that is produced, and  $D$  is the recoiling nucleus. We will refer to this perspective as

the outer kinematics of the reaction. Alternatively, we observe that our reaction model treats the target and recoiling nuclei as being composed of a valence nucleon coupled to a core which does not participate in the reaction directly. The momentum of this valence nucleon, both before and after the interaction, enters into the model. We will refer to this partition of the energy and momentum of a nucleus among its nucleons as the inner kinematics of the reaction.

### 3.1.1 Outer Kinematics

We are interested in the incoherent  $\eta$ -photoproduction reaction  $A(\gamma, \eta)A^*$ , which we label using the subscripts  $\gamma$ ,  $\eta$ ,  $T$ , and  $R$ , so that we have

$$\gamma + T \longrightarrow \eta + R \quad (3.2)$$

We begin by defining a coordinate system. We take the direction of the incident photon to be the  $z$ -axis so that in the laboratory frame the photon has four-momentum

$$p_\gamma^\mu = (E_\gamma, 0, 0, p_\gamma) \quad (3.3)$$

We define the reaction plane to be the plane spanned by the vectors  $\vec{p}_\gamma$  and  $\vec{p}_\eta$ . The  $y$ -axis will be defined to be normal to this plane using the following prescription:

$$\hat{y} \equiv \frac{(\vec{p}_\gamma \times \vec{p}_\eta)}{|\vec{p}_\gamma \times \vec{p}_\eta|} \quad (3.4)$$

Figure 3.1 shows the orientation of the axes relative to the reaction plane.

In the laboratory frame, the target nucleus has four-momentum

$$p_T^\mu = (M_T, 0, 0, 0) \quad (3.5)$$

Conservation of four-momentum implies that

$$p_\gamma^\mu + p_T^\mu = p_\eta^\mu + p_R^\mu \quad (3.6)$$

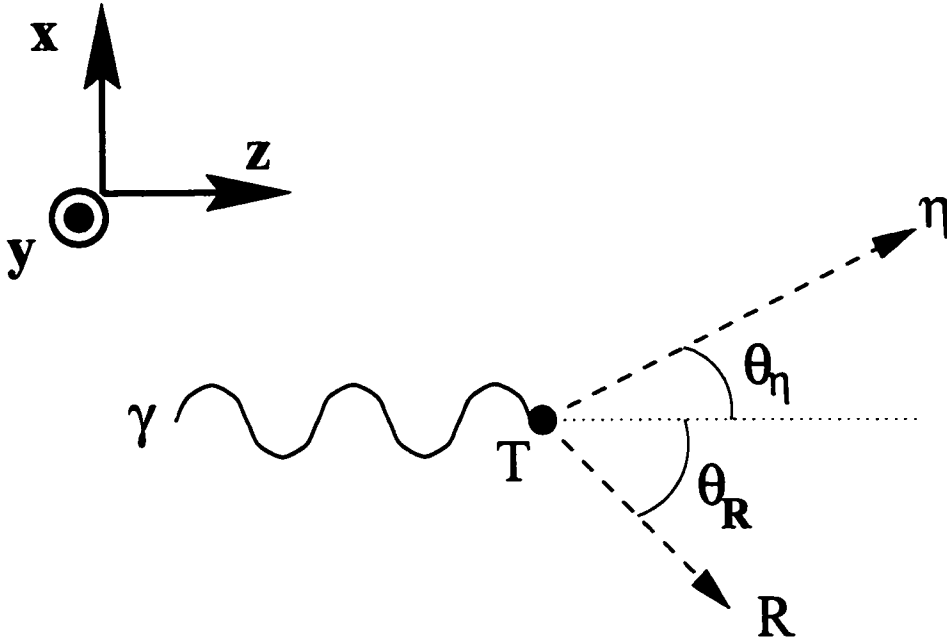


Figure 3.1: Definition of the coordinate system used for this reaction

Now we wish to obtain expressions for  $p_\eta^\mu$  and  $p_R^\mu$ . By the definition of our axes,

$$0 \leq \theta_\eta \leq 180^\circ \quad (3.7)$$

$$\phi_\eta = 0 \quad (3.8)$$

$$0 \leq \theta_R \leq 180^\circ \quad (3.9)$$

$$\phi_R = 180^\circ \quad (3.10)$$

so that the four-momenta of the outgoing particles take the form

$$p_\eta^\mu = (E_\eta, p_\eta \sin \theta_\eta, 0, p_\eta \cos \theta_\eta) \quad (3.11)$$

$$p_R^\mu = (E_R, -p_R \sin \theta_R, 0, p_R \cos \theta_R) \quad (3.12)$$

The energies and momenta of the outgoing particles are constrained by

$$E_\eta^2 - p_\eta^2 = m_\eta^2 \quad (3.13)$$

and

$$E_R^2 - p_R^2 = M_R^2 \quad (3.14)$$

Furthermore,

$$M_R = M_T + E_x \quad (3.15)$$

where  $E_x$  is the excitation energy of the final nucleus compared to the target nucleus, which is assumed to be in its ground state.

Using equations (3.3), (3.5), (3.11), and (3.12) in the conservation law (3.6), we obtain

$$E_\gamma + M_T = E_\eta + E_R \quad (3.16)$$

$$p_\eta \sin \theta_\eta - p_R \sin \theta_R = 0 \quad (3.17)$$

$$p_\gamma = p_\eta \cos \theta_\eta + p_R \cos \theta_R \quad (3.18)$$

At this stage, we observe that there is only one effective degree of freedom in the final state. This is because we are fully specifying the initial conditions and we have only two particles in the final state. As a result, we have essentially four unknowns in the final state: the energies and angles of the  $\eta$  meson and of the recoiling nucleus. Equations (3.16), (3.17), and (3.18) provide three constraints on these four unknowns. Given this situation, we need to specify only one of these four variables in order to determine the final state completely. Since, according to (2.106), we are calculating the differential cross section as a function of  $\theta_\eta$ , we will fix  $\theta_\eta$  at the start of the calculation. More specifically, we will calculate the differential cross section for a number of different fixed values of  $\theta_\eta$ .

Our next objective is to calculate  $E_\eta$  in terms of  $\theta_\eta$  and the other fixed parameters. Once we have achieved this,  $E_R$  and  $\theta_R$  are easily found using the equations already derived. By combining (3.17) with (3.18) so as to eliminate  $\theta_R$ ,

we obtain

$$p_R^2 = p_\eta^2 + p_\gamma^2 - 2p_\eta p_\gamma \cos \theta_\eta \quad (3.19)$$

Using (3.14) and (3.16) to rewrite  $p_R^2$ , we then have

$$(E_\gamma + M_T)^2 + E_\eta^2 - 2E_\eta(E_\gamma + M_T) - M_R^2 = p_\eta^2 + p_\gamma^2 - 2p_\eta p_\gamma \cos \theta_\eta \quad (3.20)$$

Finally, using (3.13) and the fact that  $p_\gamma = E_\gamma$  for the massless photon, we end up with

$$\alpha - \beta E_\eta + \kappa \sqrt{E_\eta^2 - m_\eta^2} = 0 \quad (3.21)$$

where the constants  $\alpha$ ,  $\beta$ , and  $\kappa$  are defined by

$$\alpha \equiv M_T^2 + m_\eta^2 - M_R^2 + 2E_\gamma M_T \quad (3.22)$$

$$\beta \equiv 2(E_\gamma + M_T) \quad (3.23)$$

$$\kappa \equiv 2E_\gamma \cos \theta_\eta \quad (3.24)$$

From (3.21), we get a quadratic equation for  $E_\eta$  which has solutions

$$E_\eta = \frac{\alpha\beta \pm |\kappa| \sqrt{\alpha^2 - m_\eta^2 (\beta^2 - \kappa^2)}}{\beta^2 - \kappa^2} \quad (3.25)$$

One of these solutions is unphysical and arises when we square equation (3.21).

Since we explicitly require that  $E_\eta \geq m_\eta$ , (3.21) leads to the condition

$$\frac{\beta E_\eta - \alpha}{\kappa} \geq 0 \quad (3.26)$$

If  $\theta_\eta < 90^\circ$  then  $\kappa > 0$  so that the constraint in (3.26) compels us to choose the solution of (3.25) that has  $E_\eta > \frac{\alpha}{\beta}$ . Similarly, if  $\theta_\eta > 90^\circ$  then  $\kappa < 0$  and so we choose the solution of (3.25) that has  $E_\eta < \frac{\alpha}{\beta}$ .

It is worth pointing out that by setting the argument of the square root in (3.25) to zero, we can solve for the reaction threshold:

$$(E_\gamma)_{\text{threshold}} = m_\eta \left( 1 + \frac{m_\eta}{2M_T} \right) + E_x \left( 1 + \frac{m_\eta}{M_T} + \frac{E_x}{2M_T} \right) \quad (3.27)$$



For a sufficiently massive target, the threshold is essentially the  $\eta$  mass. Nuclear recoil effects raise the threshold somewhat for less massive targets.

### 3.1.2 Inner Kinematics

Our model for the elementary reaction process explicitly incorporates the four-momentum of the particular nucleon that participates in the reaction. For example, equation (2.48) shows that  $\Gamma_{S_{11}}$  depends on the four-momenta  $k_s$  and  $k_u$ . These momenta, as defined in (2.50) and (2.51), are related to  $k_p$  and  $k_{p'}$ . Therefore, we need to specify these four-momenta in order to calculate the  $\Gamma$  operators. However, since the target nucleus remains intact after the interaction in an incoherent process, we cannot directly observe any of the nuclear constituents. As a result, a certain degree of ambiguity arises whenever we discuss the inner kinematics of the reaction.

We will choose the simplest option available to us, namely, that the four-momentum of the nucleus is partitioned equally among its constituent nucleons:

$$k_p^\mu = \frac{1}{(\hbar c)A} p_T^\mu \quad (3.28)$$

$$k_{p'}^\mu = \frac{1}{(\hbar c)A} p_R^\mu \quad (3.29)$$

where  $(\hbar c) = 197.3 \text{ MeV fm}$  converts momenta from units of MeV to units of  $\text{fm}^{-1}$ . Since the four-momentum of the nucleus, both before and after the interaction, is completely specified by the outer kinematics, this choice completely determines the inner kinematics as well. Having specified the inner kinematics, the only pieces missing in order to calculate the  $\Gamma$  operators are numerical parameters such as resonance masses, coupling constants and magnetic moments.

To conclude this section, we will now mention another approach to the problem of the inner kinematics. The calculation that we are performing is local, since

we fix all of the momenta and integrate over spacetime points. Alternatively, we could formulate a model that integrates over the momenta of the particles. In this case, the indeterminacy of the inner kinematics would no longer be a problem since all possible partitions of the nuclear momentum would be accounted for by these integrals. On the other hand, such a formalism introduces complications that are absent in our model, such as off-shell effects and cutoffs in the propagators.

## 3.2 Particle Wavefunctions

One of the pieces that goes into calculating the reaction amplitude is  $\mathcal{Z}$ , which, as given by (2.72), involves a spatial integration of particle wavefunctions and a  $\Gamma$  operator. In this section we will exhibit the ways in which the particle wavefunctions are obtained.

### 3.2.1 Nucleon Wavefunctions

In Chapter 2, we discussed how Quantum Hadrodynamics (QHD) allows us to write the wavefunction of a bound nucleon as the solution of the Dirac equation

$$[\vec{\alpha} \cdot \vec{p} + \beta(M + S(r)) + V(r)] \psi_B(\vec{x}) = E \psi_B(\vec{x}) \quad (3.30)$$

where the scalar and vector potentials  $S(r)$  and  $V(r)$  approximate the meson exchanges that mediate the strong force which binds the nucleon to the rest of the nucleus.

Since the scalar and vector potentials in (3.30) are explicitly spherically symmetric, the nucleon wavefunction  $\psi_B(\vec{x})$  can be written as a four-component

spinor with well-defined angular momentum in the form [27]:

$$\psi_{J_B M_B}(\vec{x}) = \begin{pmatrix} f_B(r) \mathcal{Y}_{L_B \frac{1}{2} J_B}^{M_B}(\Omega) \\ i g_B(r) \mathcal{Y}_{L'_B \frac{1}{2} J_B}^{M_B}(\Omega) \end{pmatrix} \quad (3.31)$$

where

$$L'_B \equiv 2J_B - L_B \quad (3.32)$$

$\mathcal{Y}_{L_B \frac{1}{2} J_B}^{M_B}(\Omega)$  is a generalized spherical harmonic. Such functions are convenient shorthand for the eigenfunctions of the angular momentum operators that are constructed from linear combinations of products of spherical harmonics and two-component spinors:

$$\mathcal{Y}_{L_B \frac{1}{2} J_B}^{M_B}(\Omega) = \sum_{\mu} \left( L_B, \frac{1}{2}; M_B - \mu, \mu \mid J_B, M_B \right) Y_{L_B}^{M_B - \mu}(\Omega) \chi_{1/2}^{\mu} \quad (3.33)$$

By substituting (3.31) into (3.30), we see that the upper and lower radial components of the nucleon wavefunction,  $f_B(r)$  and  $g_B(r)$ , are related by the coupled differential equations

$$[E_B + M + S(r) - V(r)] g_B(r) = \left[ \frac{d}{dr} + \frac{1 + \kappa_B}{r} \right] f_B(r) \quad (3.34)$$

$$[E_B - M - S(r) - V(r)] f_B(r) = - \left[ \frac{d}{dr} + \frac{1 - \kappa_B}{r} \right] g_B(r) \quad (3.35)$$

where

$$\kappa_B \equiv (L_B - J_B)(2J_B + 1) \quad (3.36)$$

Provided we specify the potentials  $S(r)$  and  $V(r)$ , in addition to the angular momentum quantum numbers of the bound nucleon, equations (3.34) and (3.35) can be solved numerically for the radial functions  $f_B(r)$  and  $g_B(r)$  which characterize  $\psi_B(\vec{x})$ .

One way to generate the potentials  $S(r)$  and  $V(r)$  is to solve numerically the coupled nonlinear QHD field equations that characterize the nucleons and mesons in the nucleus. The resulting potentials are known as Hartree potentials.

The potentials that we will use are parametrized by Woods-Saxon functions:

$$S(r) = \frac{W_S}{1 + e^{(r-R_S A^{1/3})/D_S}} \quad (3.37)$$

$$V(r) = \frac{W_V}{1 + e^{(r-R_V A^{1/3})/D_V}} \quad (3.38)$$

$R$  and  $D$  are the radius and diffuseness of the potentials and  $A$  is the mass number of the nucleus. The denominators of (3.37) and (3.38) approximate the radial dependence of the nuclear density.  $W$  represents the strength of the potentials. The potential strengths are chosen so as to reproduce the binding energy of the valence nucleon while conforming with the relative sizes of scalar and vector Hartree potentials.

By way of example, consider a  $1p_{1/2}$  proton in  $^{16}\text{O}$  with a binding energy of 12.637 MeV. Table 3.1 lists the Woods-Saxon parameters for  $^{16}\text{O}$ , as obtained in [27]. Figure 3.2 shows a graph of the radial wavefunctions  $f_B(r)$  and  $g_B(r)$  that are numerically obtained using these parameters.

Parameter	Vector	Scalar
$W$ (MeV)	367.37	-451.13
$R$ (fm)	1.0176	1.0379
$D$ (fm)	0.5728	0.6258

Table 3.1: Woods-Saxon binding potential parameters for  $^{16}\text{O}$

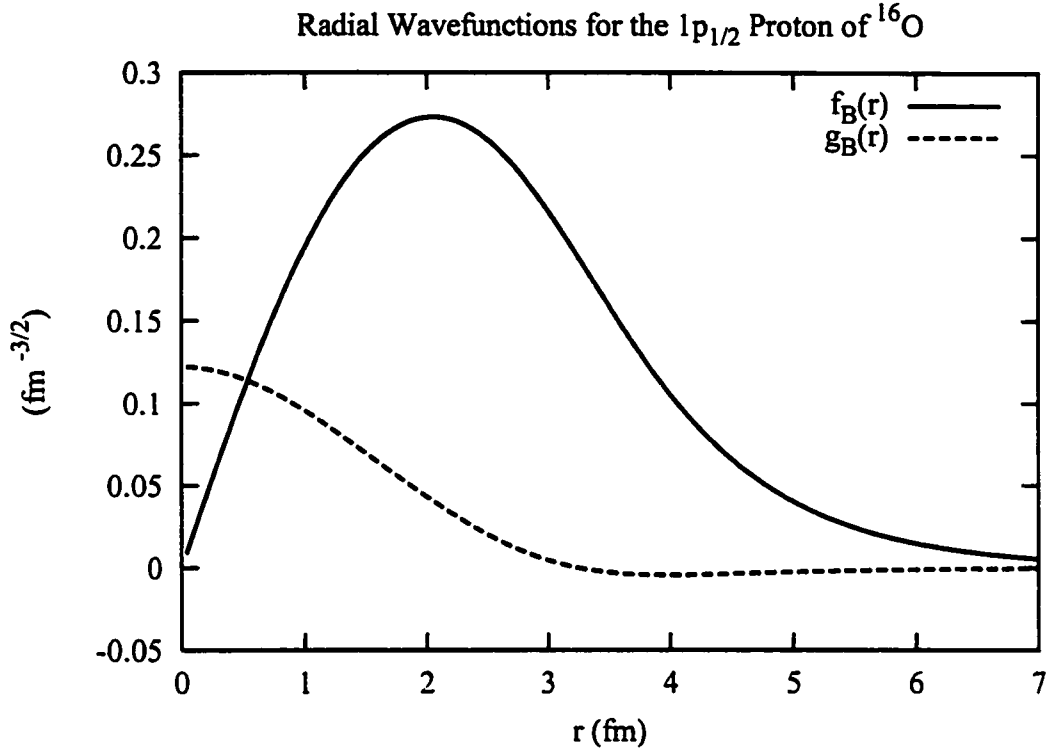


Figure 3.2: The upper and lower component radial wavefunctions of the  $1p_{1/2}$  proton of  $^{16}\text{O}$

### 3.2.2 The Photon Wavefunction

Since the incident photon has a definite energy and direction, the photon wavefunction is a plane wave, as we have already seen. In the previous subsection, we factored the wavefunctions of the bound nucleons into radial and angular parts. This factorization will be used for the other wavefunctions as well. We can write a plane wave in terms of spherical waves using [28]:

$$e^{i\vec{k}\cdot\vec{x}} = \sum_L i^L \sqrt{4\pi(2L+1)} j_L(kr) Y_L^0(\Omega) \quad (3.39)$$

where  $k \equiv |\vec{k}|$  and  $j_L(kr)$  is a spherical Bessel function of order  $L$ .

### 3.2.3 The $\eta$ Meson Wavefunction

The  $\eta$  meson is a spin-zero particle and is therefore described by the Klein-Gordon equation

$$\left[\square + m_\eta^2\right] \Phi_\eta(x) = 0 \quad (3.40)$$

which, for a time-independent interaction, reduces to

$$\left[\nabla^2 + \vec{k}_\eta^2\right] \varphi_\eta(\vec{x}) = 0 \quad (3.41)$$

Equation (3.41) assumes that the  $\eta$  meson is a free particle from the moment it is produced. This assumption might be a good approximation, but we would also like to include the possibility that the  $\eta$  meson interacts with the nucleus after it is produced. We can account for such final state interactions by including a potential term in (3.41):

$$\left[\nabla^2 + \vec{k}_\eta^2 + U(r)\right] \varphi_\eta(\vec{x}) = 0 \quad (3.42)$$

In subsection 3.2.6 we will discuss the details of this potential term.

We would now like to factor the  $\eta$  wavefunction into radial and angular parts, as we did for the photon wavefunction. The situation is more complicated with the  $\eta$  wavefunction for two reasons, though. First, the solid angle  $\Omega$  in (3.39) is measured with respect to the axis defined by  $\vec{k}$ . Since we have defined the  $z$ -axis by the direction of  $\vec{k}_\gamma$ , we can use (3.39) for the photon wavefunction with the understanding that  $\Omega$  is measured with respect to the  $z$ -axis. The  $\eta$  meson, on the other hand, does not necessarily travel in the  $z$ -direction. Given that we still want  $\Omega$  to be measured with respect to the  $z$ -axis, we have to make use of the spherical harmonic addition theorem [26]

$$Y_L^0(\Omega') = \sqrt{\frac{4\pi}{2L+1}} \sum_{M=-L}^L \left(Y_L^M(\hat{k}')\right)^* Y_L^M(\Omega) \quad (3.43)$$

to write a spherical harmonic defined with respect to the direction of the  $\eta$  meson in terms of spherical harmonics defined with respect to the  $z$ -axis. The second complication arises from the inclusion of the potential  $U(r)$  in (3.42). Since the  $\eta$  meson is not a completely free particle, it will not be a plane wave and the radial factors in the wavefunction will not be spherical Bessel functions. We will denote these radial factors by  $v_{L_\eta}(r)$ . By analogy with (3.39), and making use of (3.43), we can then expand the  $\eta$  wavefunction as

$$\varphi_\eta(\vec{x}) = 4\pi \sum_{L_\eta, M_\eta} i^{L_\eta} v_{L_\eta}(r) \left( Y_{L_\eta}^{M_\eta}(\hat{k}_\eta) \right)^* Y_{L_\eta}^{M_\eta}(\Omega) \quad (3.44)$$

Substituting (3.44) into (3.42), and noting that

$$\nabla^2 = \frac{1}{r} \frac{\partial^2}{\partial r^2} r - \frac{\hat{L}^2}{r^2} \quad (3.45)$$

we obtain an equation for  $v_{L_\eta}(r)$ :

$$\frac{1}{r} \frac{\partial^2}{\partial r^2} (r v_{L_\eta}) - \frac{L_\eta(L_\eta + 1)}{r^2} v_{L_\eta} + \left( \vec{k}_\eta^2 + U(r) \right) v_{L_\eta} = 0 \quad (3.46)$$

Given  $U(r)$ , equation (3.46) can be solved numerically to yield  $v_{L_\eta}(r)$ .

### 3.2.4 The Plane Wave Approximation

In the Plane Wave Approximation (PWA), we assume that the  $\eta$  meson does not interact with the nucleus after it is produced. This is equivalent to setting the potential  $U(r)$  in (3.42) and (3.46) equal to zero. With this substitution, (3.46) can be explicitly solved for  $v_{L_\eta}(r)$  with the result

$$v_{L_\eta}(r) = j_{L_\eta}(k_\eta r) \quad (3.47)$$

Using (3.47) in (3.44) and referring to (3.43) and (3.39), we have

$$\varphi_\eta(\vec{x}) = e^{i\vec{k}_\eta \cdot \vec{x}} \quad (3.48)$$

in other words, the  $\eta$ -meson wavefunction is indeed a plane wave.

When we use the PWA, the photon and  $\eta$  meson wavefunctions can be combined:

$$e^{i\vec{k}_\gamma \cdot \vec{x}} \varphi_\eta^*(\vec{x}) = e^{i(\vec{k}_\gamma - \vec{k}_\eta) \cdot \vec{x}} \quad (3.49)$$

With (3.39), this becomes

$$\varphi_\eta^*(\vec{x}) e^{i\vec{k}_\gamma \cdot \vec{x}} = 4\pi \sum_{L,M} i^L j_L(kr) \left( Y_L^M(\hat{k}) \right)^* Y_L^M(\Omega) \quad (3.50)$$

where  $\vec{k} \equiv (\vec{k}_\gamma - \vec{k}_\eta)$ .

### 3.2.5 The Distorted Wave Approximation

In the Distorted Wave Approximation (DWA), we allow the  $\eta$  meson to interact with the nucleus after it is produced. Since the  $\eta$  wavefunction is no longer a plane wave, we cannot combine the photon and  $\eta$  wavefunctions as easily as we did in (3.50). Instead, we combine (3.39) and (3.44) to write

$$\begin{aligned} \varphi_\eta^*(\vec{x}) e^{i\vec{k}_\gamma \cdot \vec{x}} &= 8\pi^{\frac{3}{2}} \sum_{L_\eta, M_\eta} \sum_{L_\gamma} i^{L_\gamma - L_\eta} \sqrt{2L_\gamma + 1} j_{L_\gamma}(k_\gamma r) v_{L_\eta}(r) \\ &\times Y_{L_\eta}^{M_\eta}(\hat{k}_\eta) \left( Y_{L_\eta}^{M_\eta}(\Omega) \right)^* Y_{L_\gamma}^0(\Omega) \end{aligned} \quad (3.51)$$

Comparing (3.51) with (3.50), we see that in each equation, exactly one of the spherical harmonics carries a complex conjugation. On the other hand, we are fixing the kinematics for the calculation from the beginning, so a spherical harmonic of the form  $Y_L^M(\hat{k})$  is just a number, whereas a spherical harmonic of the form  $Y_L^M(\Omega)$  is a function of an angle over which we will integrate. We will find it useful to cast (3.51) in a form that is as similar to (3.50) as possible. In particular, we would like to write the spherical harmonic functions in (3.51) without complex conjugation. Using the identity

$$\left( Y_L^M(\theta, \phi) \right)^* = (-1)^M Y_L^{-M}(\theta, \phi) \quad (3.52)$$



on both of the  $Y_{L_\eta}^{M_\eta}$  spherical harmonics in (3.51), we have three changes. First, we pick up two factors of  $(-1)^{M_\eta}$ , but since  $M_\eta$  is an integer, these factors do not change the expression. Second, we replace  $M_\eta$  with  $-M_\eta$  in both of the spherical harmonics. Since  $M_\eta$  only occurs in these two places and we are summing over  $M_\eta$  from  $-L_\eta$  to  $L_\eta$ , this change does not affect our expression either. The final change is that we have moved the complex conjugation from  $Y_{L_\eta}^{M_\eta}(\Omega)$  to  $Y_{L_\eta}^{M_\eta}(\hat{k}_\eta)$ , as intended. As a result, we now have

$$\begin{aligned} \varphi_\eta^*(\vec{x}) e^{i\vec{k}_\eta \cdot \vec{x}} &= 8\pi^{\frac{3}{2}} \sum_{L_\eta, M_\eta} \sum_{L_\gamma} i^{L_\gamma - L_\eta} \sqrt{2L_\gamma + 1} j_{L_\gamma}(k_\gamma r) v_{L_\eta}(r) \\ &\times (Y_{L_\eta}^{M_\eta}(\hat{k}_\eta))^* Y_{L_\eta}^{M_\eta}(\Omega) Y_{L_\gamma}^0(\Omega) \end{aligned} \quad (3.53)$$

### 3.2.6 $\eta$ Optical Potentials

Whenever mesons are produced on a nucleus, the mesons are strongly affected by their final-state interactions with the nucleus. Therefore, the wavefunction of the  $\eta$  meson is given by the solution of the Klein-Gordon equation (3.42) which contains a potential term  $U(r)$  to describe these final state interactions. This potential term is often written as

$$U(r) = -2\omega_\eta V_{opt}(r) \quad (3.54)$$

where  $\omega_\eta$  is the  $\eta$  energy in  $\text{fm}^{-1}$  and  $V_{opt}(r)$  is called the optical potential. Hereafter, we will be working with  $U(r)$  directly and we will refer to this potential as the optical potential.

The most common way to construct an optical potential is to use the  $t\rho$  approximation

$$U(r) = t\rho(r) \quad (3.55)$$

where  $\rho(r)$  is the nuclear density and  $t$  is a parameter that is related to the  $\eta N \rightarrow \eta N$  scattering amplitude  $f$  by

$$t = 4\pi \frac{(p_\eta)_{LAB}}{(p_\eta)_{CM}} f \quad (3.56)$$

At this stage, the situation remains unclear. If we were interested in constructing a  $\pi$  optical potential, we could proceed through the same reasoning as above. Since the  $\pi N$  interaction is well known, both theoretically and experimentally, we would have little trouble in finding the scattering amplitude in (3.56). Unfortunately, the  $\eta N$  interaction is not so well understood and so we have to postulate a plausible form for the scattering amplitude in order to construct the  $\eta$  optical potential. We will look at two different optical potentials.

The first optical potential, which we shall denote by DW1, was used by Lee *et al.* [11]. Using results from the coupled-channel approach of Bennhold *et al.* [1], they parametrize the  $\eta N$  scattering amplitude as

$$f = \frac{a_\eta}{1 - ia_\eta(p_\eta)_{CM} + \frac{1}{2}a_\eta r_\eta(p_\eta)_{CM}^2} \quad (3.57)$$

with the parameters

$$a_\eta = (0.25 + i0.118) \text{ fm} \quad (3.58)$$

$$r_\eta = (-5.71 - i0.391) \text{ fm} \quad (3.59)$$

The second optical potential that we will use will be labelled DW3. It was introduced by Peters *et al.* [20] using the results of Effenberger *et al.* [14]. Writing the optical potential as a  $t\rho$  ansatz with no real part, they obtain

$$U(r) = i(3 \text{ fm}^2)p_\eta\rho(r) \quad (3.60)$$

We will now illustrate some of the features of these optical potentials. Figure 3.3 depicts the nuclear density function,  $\rho(r)$ , as calculated in our computer

program `dw.for`, for each of the three nuclei that we will be studying:  $^{12}\text{C}$ ,  $^{16}\text{O}$ , and  $^{40}\text{Ca}$ . These functions are normalized so that

$$\int \rho(r) dV = A \quad (3.61)$$

where  $A$  is the total number of nucleons in the nucleus. In Figure 3.4, we show the density-independent parts of the optical potentials. These parts correspond to the  $t$  factor in (3.55).

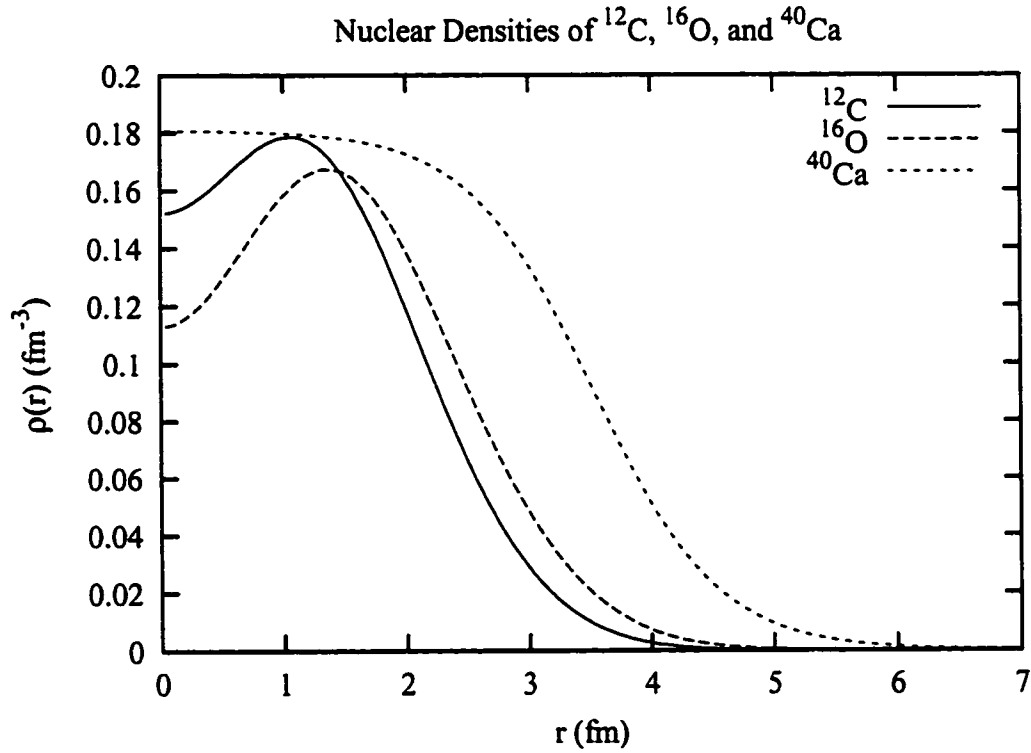


Figure 3.3: Graph of the nuclear densities for  $^{12}\text{C}$ ,  $^{16}\text{O}$ , and  $^{40}\text{Ca}$

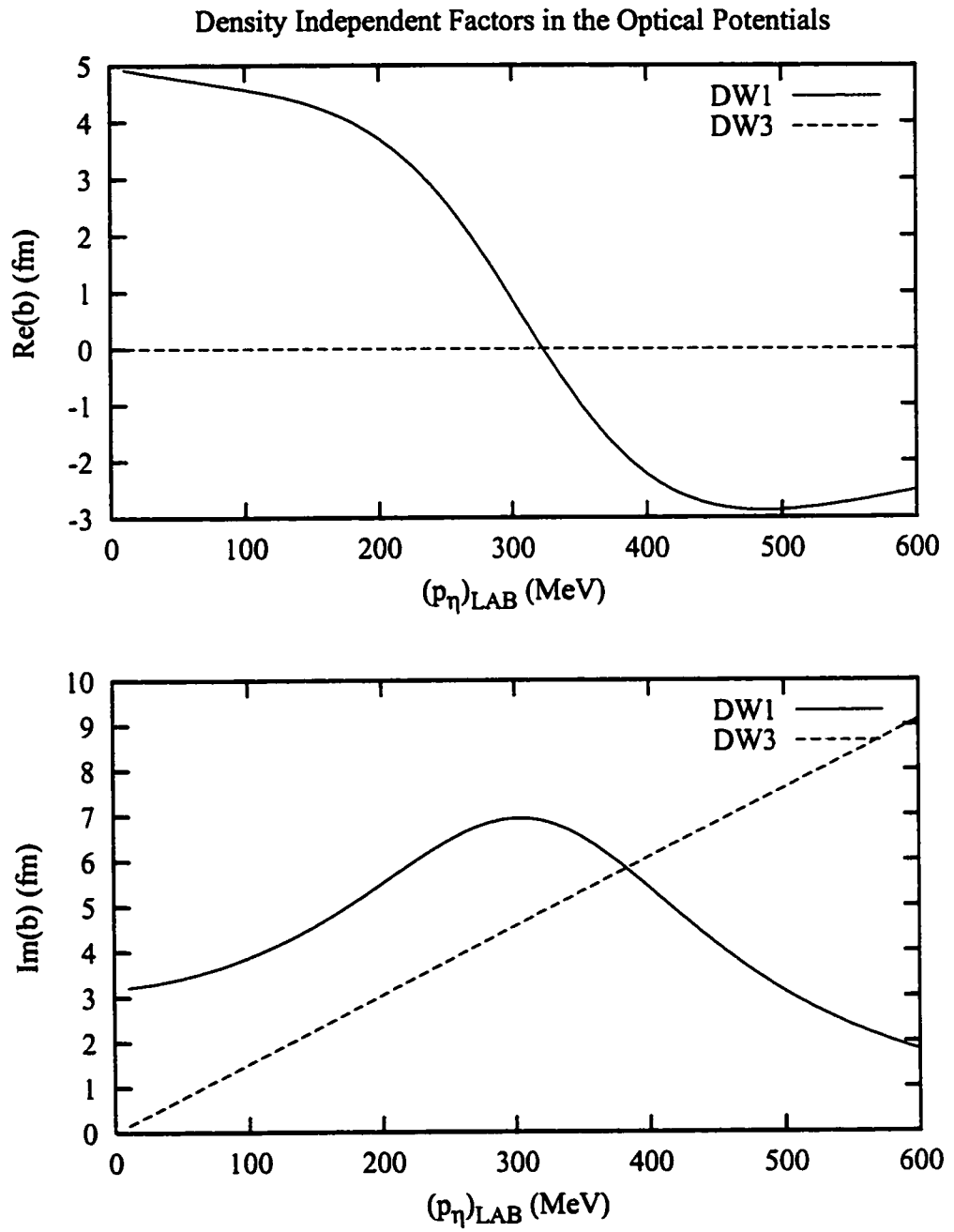


Figure 3.4: Comparison of the DW1 and DW3 optical potentials

### 3.3 Evaluation of the Integral

One of the steps along the way to a calculation of the differential cross section is to evaluate  $\mathcal{Z}$ , which was first defined in (2.72) of Chapter 2 as

$$\mathcal{Z} \equiv \int d^3x \psi_{J_{B'}, M_{B'}}^\dagger(\vec{x}) \Gamma \psi_{J_B M_B}(\vec{x}) \varphi_\eta^*(\vec{x}) e^{i\vec{k}_\gamma \cdot \vec{x}} \quad (3.62)$$

In the previous section, we saw how to factor the wavefunctions that appear in (3.62) into radial and angular pieces. Now we will use these results to express  $\mathcal{Z}$  in terms of radial and angular integrals.

#### 3.3.1 Substituting the Wavefunctions

Using

$$\int d^3x = \int r^2 dr \int d\Omega \quad (3.63)$$

we can substitute the wavefunctions, as found in the previous section, into (3.62).

The initial bound state nucleon wavefunction was given in (3.31) as

$$\psi_{J_B M_B}(\vec{x}) = \begin{pmatrix} f_B(r) \mathcal{Y}_{L_B \frac{1}{2} J_B}^{M_B}(\Omega) \\ i g_B(r) \mathcal{Y}_{L'_B \frac{1}{2} J_B}^{M_B}(\Omega) \end{pmatrix} \quad (3.64)$$

where  $L'_B \equiv 2J_B - L_B$ . Similarly, we can write the adjoint of the final bound state nucleon wavefunction as

$$\psi_{J_{B'}, M_{B'}}^\dagger(\vec{x}) = \left[ f_{B'}(r) \left( \mathcal{Y}_{L_{B'} \frac{1}{2} J_{B'}}^{M_{B'}}(\Omega) \right)^\dagger - i g_{B'}(r) \left( \mathcal{Y}_{L'_{B'} \frac{1}{2} J_{B'}}^{M_{B'}}(\Omega) \right)^\dagger \right] \quad (3.65)$$

where  $L'_{B'} \equiv 2J_{B'} - L_{B'}$ .

In the PWA, we will use (3.50):

$$\varphi_\eta^*(\vec{x}) e^{i\vec{k}_\gamma \cdot \vec{x}} = 4\pi \sum_{L, M} i^L j_L(kr) \left( Y_L^M(\hat{k}) \right)^* Y_L^M(\Omega) \quad (3.66)$$

where  $\vec{k} \equiv (\vec{k}_\gamma - \vec{k}_\eta)$ , whereas in the DWA, we will make use of (3.53):

$$\begin{aligned} \varphi_\eta^*(\vec{x}) e^{i\vec{k}_\gamma \cdot \vec{x}} &= 8\pi^{\frac{3}{2}} \sum_{L_\eta, M_\eta} \sum_{L_\gamma} i^{L_\gamma - L_\eta} \sqrt{2L_\gamma + 1} j_{L_\gamma}(k_\gamma r) v_{L_\eta}(r) \\ &\times \left( Y_{L_\eta}^{M_\eta}(\hat{k}_\eta) \right)^* Y_{L_\eta}^{M_\eta}(\Omega) Y_{L_\gamma}^0(\Omega) \end{aligned} \quad (3.67)$$

Finally, we will write the  $4 \times 4$  matrix operator  $\Gamma$  in terms of four  $2 \times 2$  matrix operators  $\Gamma_{ij}$ :

$$\Gamma = \begin{pmatrix} \Gamma_{11} & \Gamma_{12} \\ \Gamma_{21} & \Gamma_{22} \end{pmatrix} \quad (3.68)$$

For the PWA, when we substitute (3.31), (3.65), (3.66), and (3.68) into (3.62), we obtain

$$\mathcal{Z}_{PWA} = 8\pi^{\frac{3}{2}} \sum_{L, M} i^L \left( Y_L^M(\hat{k}) \right)^* \{ R_{ff} A_{11} + i R_{fg} A_{12} - i R_{gf} A_{21} + R_{gg} A_{22} \} \quad (3.69)$$

In the DWA, using (3.67) in place of (3.66), we have

$$\begin{aligned} \mathcal{Z}_{DWA} &= 8\pi^{\frac{3}{2}} \sum_{L_\gamma, L_\eta} i^{L_\gamma - L_\eta} \sqrt{2L_\gamma + 1} \sum_{M_\eta} \left( Y_{L_\eta}^{M_\eta}(\hat{k}_\eta) \right)^* \\ &\times \{ R_{ff} A_{11} + i R_{fg} A_{12} - i R_{gf} A_{21} + R_{gg} A_{22} \} \end{aligned} \quad (3.70)$$

$R_{XY}$  and  $A_{ij}$  are shorthand notations for the radial and angular integrals, respectively. We will now examine their explicit forms for both the PWA and DWA.

### 3.3.2 The Radial Integrals

In the DWA, the radial integrals that appear in (3.70) are defined by

$$R_{XY} \equiv \int X_{B'}(r) Y_B(r) j_{L_\gamma}(k_\gamma r) v_{L_\eta}(k_\eta r) r^2 dr \quad (3.71)$$

where  $X_{B'}$  is either the upper or lower radial wavefunction for the final nucleon bound state, as specified by the first subscript of  $R_{XY}$ , and  $Y_B$  is either the upper

or lower radial wavefunction for the initial nucleon bound state, as specified by the second subscript of  $R_{XY}$ . Similarly, for the PWA, the radial integrals in (3.69) are defined by

$$R_{XY} \equiv \int X_{B'}(r) Y_B(r) j_L(kr) r^2 dr \quad (3.72)$$

All of the functions in (3.72) and (3.71) are calculated numerically as arrays over the range of 0 fm to 20 fm with a radial lattice spacing of 0.04 fm. The radial integrations are then performed numerically using Simpson's rule.

### 3.3.3 The Angular Integrals

In the DWA, the angular integrals that occur in (3.69) are defined by

$$A_{ij} \equiv \int \left( \mathcal{Y}_{\lambda_{B'}^i \frac{1}{2} J_{B'}}^{M_{B'}}(\Omega) \right)^\dagger \Gamma_{ij} \mathcal{Y}_{\lambda_B^j \frac{1}{2} J_B}^{M_B}(\Omega) Y_{L_\eta}^{M_\eta}(\Omega) Y_{L_\gamma}^0(\Omega) d\Omega \quad (3.73)$$

where

$$\lambda_{B'}^i \equiv \begin{cases} L_{B'} & \text{if } i = 1 \\ L'_{B'} & \text{if } i = 2 \end{cases} \quad (3.74)$$

and

$$\lambda_B^j \equiv \begin{cases} L_B & \text{if } j = 1 \\ L'_B & \text{if } j = 2 \end{cases} \quad (3.75)$$

Similarly, for the PWA, the angular integrals in (3.69) are defined by

$$A_{ij} \equiv \int \left( \mathcal{Y}_{\lambda_{B'}^i \frac{1}{2} J_{B'}}^{M_{B'}}(\Omega) \right)^\dagger \Gamma_{ij} \mathcal{Y}_{\lambda_B^j \frac{1}{2} J_B}^{M_B}(\Omega) Y_L^M(\Omega) Y_0^0(\Omega) d\Omega \quad (3.76)$$

Notice that we have used

$$Y_0^0(\Omega) = \frac{1}{\sqrt{4\pi}} \quad (3.77)$$

in order to include a second spherical harmonic in (3.76). This spherical harmonic is used to bring the PWA angular integrals into the same form as the DWA

angular integrals. Equation (3.69) already carries an extra factor of  $2\pi^{\frac{1}{2}}$  to compensate for this spherical harmonic. We will write this common form as

$$A = \int \left( \mathcal{Y}_{L_2 \frac{1}{2} J_2}^{M_2}(\Omega) \right)^\dagger \Delta \mathcal{Y}_{L_1 \frac{1}{2} J_1}^{M_1}(\Omega) Y_{L_3}^{M_3}(\Omega) Y_{L_4}^0(\Omega) d\Omega \quad (3.78)$$

where  $\Delta$  is a  $2 \times 2$  matrix operator corresponding to  $\Gamma_{ij}$ . To evaluate (3.78), we are going to use a result derived in [24] which makes use of spherical tensor techniques to express this angular integral in terms of 3-j and 6-j symbols.

The first step of this process is to rewrite  $\Delta$  as a linear combination of the  $2 \times 2$  identity matrix  $I_2$  and the three Pauli spin matrices:

$$\Delta = CI_2 + \vec{D} \cdot \vec{\sigma} \quad (3.79)$$

This can be done by writing  $\Delta$  explicitly as a  $2 \times 2$  matrix and expanding the right side of equation (3.79) so that we have

$$\begin{pmatrix} \Delta_{11} & \Delta_{12} \\ \Delta_{21} & \Delta_{22} \end{pmatrix} = \begin{pmatrix} C + D_3 & D_1 - iD_2 \\ D_1 + iD_2 & C - D_3 \end{pmatrix} \quad (3.80)$$

which can be solved for the expansion coefficients  $C$  and  $\vec{D}$  using

$$C = \frac{1}{2} (\Delta_{11} + \Delta_{22}) \quad (3.81)$$

$$D_1 = \frac{1}{2} (\Delta_{21} + \Delta_{12}) \quad (3.82)$$

$$D_2 = \frac{1}{2i} (\Delta_{21} - \Delta_{12}) \quad (3.83)$$

$$D_3 = \frac{1}{2} (\Delta_{11} - \Delta_{22}) \quad (3.84)$$

The Cartesian vector  $\vec{D}$  is related to a spherical tensor of rank one by the transformation

$$\begin{aligned} D_1^1 &= -\frac{1}{\sqrt{2}} (D_x + iD_y) \\ D_1^{-1} &= \frac{1}{\sqrt{2}} (D_x - iD_y) \\ D_1^0 &= D_z \end{aligned} \quad (3.85)$$



Similarly, we can transform  $\vec{\sigma}$  into a rank-one spherical tensor so that (3.79) becomes

$$\Delta = CI_2 + \sum_{\mu} (-1)^{\mu} D_1^{-\mu} \sigma_1^{\mu} \quad (3.86)$$

Using this result, (3.78) can be broken down into

$$A = CS + \sum_{\mu} (-1)^{\mu} D_1^{-\mu} \mathcal{T}_1^{\mu} \quad (3.87)$$

where  $S$  and  $\mathcal{T}_1^{\mu}$  are integrals that behave under rotations as a scalar and a rank-one spherical tensor. They are defined by

$$S \equiv \int \left( \mathcal{Y}_{L_2 \frac{1}{2} J_2}^{M_2}(\Omega) \right)^{\dagger} \mathcal{Y}_{L_1 \frac{1}{2} J_1}^{M_1}(\Omega) Y_{L_3}^{M_3}(\Omega) Y_{L_4}^0(\Omega) d\Omega \quad (3.88)$$

$$\mathcal{T}_1^{\mu} \equiv \int \left( \mathcal{Y}_{L_2 \frac{1}{2} J_2}^{M_2}(\Omega) \right)^{\dagger} \sigma_1^{\mu} \mathcal{Y}_{L_1 \frac{1}{2} J_1}^{M_1}(\Omega) Y_{L_3}^{M_3}(\Omega) Y_{L_4}^0(\Omega) d\Omega \quad (3.89)$$

The next step, which is somewhat tedious, is to apply a number of theorems and identities concerning angular momentum coupling to (3.88) and (3.89) in order to write these integrals in terms of 3-j and 6-j symbols. The 3-j symbol is a close relative of the Clebsch-Gordan coefficient; both are used when coupling two angular momenta. The two are related by [26]

$$\begin{pmatrix} L_1 & L_2 & L_3 \\ M_1 & M_2 & -M_3 \end{pmatrix} = \frac{(-1)^{L_1-L_2+M_3}}{\hat{L}_3} (L_1, L_2; M_1, M_2 | L_3, M_3) \quad (3.90)$$

where  $\hat{L} \equiv \sqrt{2L+1}$ . The 6-j symbol is related to the Racah coefficient; both are used when coupling three angular momenta. They are related by [26]

$$\begin{Bmatrix} J_1 & J_2 & J_{12} \\ J_3 & J & J_{23} \end{Bmatrix} = (-1)^{J_1+J_2+J_3+J} W(J_1, J_2, J, J_3; J_{12}, J_{23}) \quad (3.91)$$

With these notations in place, we now proceed to write the final expressions for  $S$  and  $\mathcal{T}_1^{\mu}$ , as given in [24]:

$$\begin{aligned}
S = & (-1)^{2J_2+\frac{1}{2}-M_2+M_3} \frac{\hat{L}_3 \hat{L}_4 \hat{J}_2 \hat{J}_1}{4\pi} \\
& \times \sum_A (2A+1) \frac{1}{2} [1 + (-1)^{L_2+L_1+A}] \\
& \times \begin{pmatrix} J_2 & J_1 & A \\ 1/2 & -1/2 & 0 \end{pmatrix} \begin{pmatrix} J_2 & J_1 & A \\ -M_2 & M_1 & M_A \end{pmatrix} \\
& \times \begin{pmatrix} L_3 & L_4 & A \\ 0 & 0 & 0 \end{pmatrix} \begin{pmatrix} L_3 & L_4 & A \\ M_3 & 0 & -M_A \end{pmatrix} \quad (3.92)
\end{aligned}$$

$$\begin{aligned}
\mathcal{T}_1^\mu = & \frac{1}{2\pi} \sqrt{\frac{3}{2}} (-1)^{2J_2+L_2+\mu+M_3} \hat{J}_2 \hat{J}_1 \hat{L}_3 \hat{L}_4 \\
& \times \sum_A (2A+1) \frac{1}{2} [1 + (-1)^{L_2+L_1+A}] \\
& \times \begin{pmatrix} L_3 & L_4 & A \\ 0 & 0 & 0 \end{pmatrix} \begin{pmatrix} L_3 & L_4 & A \\ M_3 & 0 & -M_A \end{pmatrix} \\
& \times \sum_K (2K+1) \begin{pmatrix} J_1 & A & K \\ -1/2 & 0 & 1/2 \end{pmatrix} \begin{pmatrix} J_1 & A & K \\ M_1 & M_A & M_K \end{pmatrix} \\
& \times \begin{pmatrix} 1 & J_2 & K \\ -\mu & M_2 & M_K \end{pmatrix} \left\{ \begin{matrix} L_2 & 1/2 & J_2 \\ 1 & K & 1/2 \end{matrix} \right\} \quad (3.93)
\end{aligned}$$

These are certainly formidable expressions, but as a result of all the selection rules that apply to 3-j and 6-j coefficients, they can be evaluated quickly. Optimizing the speed of the calculation is quite important since we have summations over  $M_B$  and  $M_{B'}$ , in addition to  $L$  and  $M$  for the PWA or  $L_\eta$ ,  $M_\eta$ , and  $L_\gamma$  for the DWA. These summations require the evaluation of as many as a billion angular integrals like the one in (3.87) over the course of a DWA calculation!

## Appendix 3.A Parameter Values

To go beyond the analytic expressions for the reaction amplitude and the observables, we require numerical values for the parameters that appear in these expressions, such as coupling constants, particle and resonance masses, magnetic moments, and off-shell parameters. While some of these parameters, such as the mass of the  $\eta$  meson, are very well determined experimentally, there are other parameters that are not known so accurately. In this appendix we will tabulate the numerical values that were used for the parameters in our calculations.

Table 3.2 shows the masses and widths of the particles we encounter. We neglect the width of the  $\eta$  meson during our calculations since it is so much smaller than  $m_\eta$ .

Particle	Mass (MeV)	Width (MeV)
$\eta$	547.30	0
$p$	938.27231	0
$\rho$	770.0	153.0
$\omega$	782.0	8.5
$P_{11}(1440)$	1440	350
$D_{13}(1520)$	1520	120
$S_{11}(1535)$	1535	150

Table 3.2: Masses and widths of the particles in our calculations [2]

Many other parameters appear in the expressions for the  $\Gamma$  matrix operators in (2.48) and equations (2.53) through (2.57). These parameters were obtained in [8] by fitting to existing data sets for  $\eta$ -photoproduction experiments. We use

the values obtained with a vector meson form factor cutoff of  $\Lambda^2 = 1.2 \text{ GeV}^2$ . Table 3.3 summarizes the coupling constants and magnetic moments in these equations.

Parameter	Numerical Value	Parameter	Numerical Value
$g_{\eta NN}$	4.1	$\lambda_\rho$	1.06
$g_{\eta NS_{11}}$	2.01991	$\lambda_\omega$	0.31
$g_{\eta NP_{11}}$	2.60322	$(g_v)_\rho$	2.63
$\kappa_p$	1.7928456	$(g_t)_\rho$	16.05
$\kappa_{S_{11}}$	0.880317	$(g_v)_\omega$	10.09
$\kappa_{P_{11}}$	-0.00379488	$(g_t)_\omega$	1.42
$f_{\eta ND_{13}} \kappa_{D_{13}}^{(1)}$	15.306		
$f_{\eta ND_{13}} \kappa_{D_{13}}^{(2)}$	16.1189		

Table 3.3: Coupling constants and magnetic moments used in our calculations

Finally, equation (2.58) refers to the off-shell parameters  $X$ ,  $Y$ , and  $Z$ . We use the values in Table 3.4.

Parameter	Numerical Value
$X$	-1
$Y$	-0.025
$Z$	0

Table 3.4: Off-shell parameters used in our calculations

With these parameters in hand, along with a complete set of kinematic information, we are in a position to evaluate all the different  $\Gamma$  matrix operators. Once we have these operators, each in the form of a  $4 \times 4$  matrix of complex numbers, we can easily extract all the coefficients  $C$  and  $D_1^\mu$  that appear in equation (3.87) for the angular integrals.

## Appendix 3.B The Spectroscopic Factors

Looking at equation (2.106), our final expression for the differential cross section, we see that it contains the spectroscopic factors  $[S_{J_i J_C}(J_B)]$  and  $[S_{J_f J_C}(J_{B'})]$ . When we first introduced these factors in section 2.3.2 to write the initial and final bound state nucleon wavefunctions, we mentioned that these spectroscopic factors were there to account for the probability that the real nuclei have the shell-configurations that we assumed. In this appendix, we will see how to assign numerical values to these spectroscopic values.

Using the nuclear shell model, we describe the ground state of a nucleus by placing all of the protons and neutrons in the lowest energy shells such that the Pauli exclusion principle is not violated. In Table 3.5, we show the hierarchy of the nuclear shells, listed in order of increasing energy [29].

Shell	Occupancy
$1s_{\frac{1}{2}}$	2
$1p_{\frac{3}{2}}$	4
$1p_{\frac{1}{2}}$	2
$1d_{\frac{5}{2}}$	6
$2s_{\frac{1}{2}}$	2
$1d_{\frac{3}{2}}$	4
$1f_{\frac{7}{2}}$	8

Table 3.5: Hierarchy and occupancy of nuclear shells

By way of example, let us consider an  $^{16}\text{O}$  target. In the ground state, the

eight protons in this nucleus fill all the shells up to and including the  $1p_{\frac{1}{2}}$  shell. The same can be said of the eight neutrons in this nucleus. Now suppose that we fix the final state of the recoiling nucleus to be the  $3^-$  state having an excitation energy of 7.88 MeV. We would like to write the wavefunction of this state in terms of the excitations of individual nucleons into higher energy shells. Using a sophisticated shell model calculation, it was shown [30] that this excited state is fairly well described by a single  $1p - 1h$  excitation of a nucleon from the  $1p_{\frac{1}{2}}$  shell to the  $1d_{\frac{3}{2}}$  shell. A similar result is given in Table 6.1 of [29], which we show in Table 3.6.

$p$	$1f_{\frac{7}{2}}$	$1f_{\frac{5}{2}}$	$1d_{\frac{5}{2}}$	$1d_{\frac{3}{2}}$	$1d_{\frac{1}{2}}$
$h^{-1}$	$1s_{\frac{1}{2}}^{-1}$	$1s_{\frac{1}{2}}^{-1}$	$1p_{\frac{3}{2}}^{-1}$	$1p_{\frac{1}{2}}^{-1}$	$1p_{\frac{1}{2}}^{-1}$
$p$	-0.01	+0.01	+0.15	-0.20	+0.72
$n$	-0.02	+0.01	+0.15	-0.18	+0.60

Table 3.6: Wavefunction of the  $3^-$ ,  $E_x = 7.88$  MeV state of  $^{16}\text{O}$

The numbers given in Table 3.6 correspond to the coefficients of the different  $1p - 1h$  terms in the wavefunction of the state. The large values in the last column indicate that nearly 90% of this state consists of the  $1d_{\frac{3}{2}} - 1p_{\frac{1}{2}}^{-1}$  configuration, with the remainder of the state consisting of small amounts of other configurations. We will ignore these other configurations and assume that the  $3^-$ ,  $E_x = 7.88$  MeV state of  $^{16}\text{O}$  consists solely of the  $1d_{\frac{3}{2}} - 1p_{\frac{1}{2}}^{-1}$  configuration. With this assumption, we have now determined one of the spectroscopic factors:

$$[S_{J_f J_C}(J_{B'})] = 1 \quad (3.94)$$

In our calculations, we will be working with three different targets:  $^{12}\text{C}$ ,  $^{16}\text{O}$ ,

and  $^{40}\text{Ca}$ . For the  $^{12}\text{C}$  target, we will consider four different nuclear resonances for the final state. Using the spectroscopic information in [30] and [31], we summarize the resonance configurations in Table 3.7. In all six cases, the nuclear

Nucleus	Resonance	Configuration
$^{12}\text{C}$	$1^+, E_x = 12.71 \text{ MeV}$	$1p_{\frac{1}{2}} - 1p_{\frac{3}{2}}^{-1}$
$^{12}\text{C}$	$2^+, E_x = 4.44 \text{ MeV}$	$1p_{\frac{1}{2}} - 1p_{\frac{3}{2}}^{-1}$
$^{12}\text{C}$	$2^+, E_x = 16.11 \text{ MeV}$	$1p_{\frac{1}{2}} - 1p_{\frac{3}{2}}^{-1}$
$^{12}\text{C}$	$3^-, E_x = 9.641 \text{ MeV}$	$1d_{\frac{5}{2}} - 1p_{\frac{3}{2}}^{-1}$
$^{16}\text{O}$	$3^-, E_x = 7.88 \text{ MeV}$	$1d_{\frac{5}{2}} - 1p_{\frac{1}{2}}^{-1}$
$^{40}\text{Ca}$	$5^-, E_x = 4.48 \text{ MeV}$	$1f_{\frac{7}{2}} - 1d_{\frac{3}{2}}^{-1}$

Table 3.7: Resonance configurations used in our calculations

excited states are fairly well described by a single  $1p - 1h$  configuration, therefore we will be using (3.94) for the final state spectroscopic factor in all our calculations. On the other hand, we see that three of the  $^{12}\text{C}$  resonances are predominantly described by the  $1p_{\frac{1}{2}} - 1p_{\frac{3}{2}}^{-1}$  configuration. This implies that there is not a one-to-one correspondence between the  $1p - 1h$  descriptions of the excited states of a nucleus and the  $J^\pi$  descriptions. The resolution of this difficulty requires a closer examination of nuclear structure. We will address this point



again in the next chapter. For now, however, we will take a different approach for the sake of a model calculation. Rather than specifying the precise nature of the nuclear excited state and then inferring the dominant  $1p - 1h$  configuration, we will instead fix the  $1p - 1h$  configuration and then infer a possible candidate for the nuclear excited state. We will still use (3.94) for the final spectroscopic factor.

Our next task is to determine the initial-state spectroscopic factor  $[S_{J_i J_C}(J_B)]$ . For  $^{16}\text{O}$ , for instance, we have already decided that a  $1p_{\frac{1}{2}}$  nucleon is going to be excited to the  $1d_{\frac{5}{2}}$  shell so that a  $3^-$  resonance with an excitation energy of  $E_x = 7.88 \text{ MeV}$  will be formed. The problem that we encounter is that there are two protons in the  $1p_{\frac{1}{2}}$  shell, along with two neutrons, and we have no way of knowing which of these nucleons is excited to the  $1d_{\frac{5}{2}}$  shell. Furthermore, the reaction formalism developed in Chapter 2 assumes that the nucleon is a proton.

Let us begin by addressing the first of these difficulties. If we assume that the reaction can only take place on a proton in the  $1p_{\frac{1}{2}}$  shell, then we must multiply the final cross sections by two since we have no way of knowing which of the  $1d_{\frac{5}{2}}$  protons participated in the reaction. The business of neutrons is not as clear. Ideally, we would incorporate neutrons into our effective Lagrangian formalism from the start. Unfortunately, we would not be able to obtain accurate parameters for the terms involving neutrons since it is impossible to perform certain photoproduction experiments on free neutrons. Typically, we infer information about the behavior of neutrons by doing photoproduction experiments with protons and then repeating the experiments with deuterons. For example, in an experiment at MAMI, Krusche *et al.* [4] investigated the  $\eta$ -photoproduction reaction  $n(\gamma, \eta)n$  by doing the corresponding  $p(\gamma, \eta)p$  and  $d(\gamma, \eta)d$  experiments. They found that for photon energies in the range 680 – 790 MeV, the  $\eta$ -photoproduction cross

sections for neutron targets were only two-thirds as large as the corresponding cross sections for proton targets:

$$\frac{\sigma_n}{\sigma_p} = (0.66 \pm 0.01) \quad (3.95)$$

At photon energies higher than we will be using, preliminary data seemed to indicate that the two cross sections were roughly equal. For our purposes, we will take

$$\frac{\sigma_n}{\sigma_p} = \frac{2}{3} \quad (3.96)$$

at all energies. As a result, the initial state spectroscopic factor will be taken to be the number of protons in the  $1p_{\frac{1}{2}}$  shell, multiplied by the factor  $\frac{5}{3}$  in order to account for the neutrons. In general, we are fixing  $J_B$  and  $J_{B'}$  and setting

$$[\mathcal{S}_{J_i J_C}(J_B)] = \left(1 + \frac{2}{3}\right) (2J_B + 1) \quad (3.97)$$

Equations (3.94) and (3.97) are the forms of the spectroscopic factors that will be used to calculate the differential cross section (2.106).

## Appendix 3.C Tests of the Code

In order to calculate observable quantities for incoherent  $\eta$ -photoproduction reactions from complex nuclei, we have written several computer programs. In addition, we have written extensive documentation files which thoroughly explain the detailed structure of the programs. In this appendix, we will briefly show the overall structure of the programs and discuss some of the programming tests that were performed in order to check the validity of the programs.

In our calculations, we are fixing both the initial and final states of the interacting nucleon to a specific bound state with well defined angular momentum quantum numbers, as opposed to an allowance for configuration mixing, whereby the initial and final nucleon states would each be linear combinations of several specific bound states. As a result, we require only one set of radial wavefunctions for each of the initial and final bound state nucleons:  $f_B(r)$ ,  $g_B(r)$ ,  $f_{B'}(r)$ , and  $g_{B'}(r)$ . The program `bound.for` calculates  $f(r)$  and  $g(r)$  for a bound nucleon and writes these wavefunctions to a data file. We used this program to generate the radial wavefunctions for a  $1p_{\frac{1}{2}}$  proton in  $^{16}\text{O}$  in Section 3.2.1, as displayed in Figure 3.2. This program automatically checks that the wavefunctions satisfy the correct normalization condition:

$$\int \left( f^2(r) + g^2(r) \right) r^2 dr = 1 \quad (3.98)$$

The documentation for this program is contained in `bound.doc`.

The program `pw.for` calculates the observables in the PWA, with the file `pw.doc` containing the detailed documentation. Many of the subroutines in this program have been borrowed from the code used in [19] to calculate observables for quasifree  $\eta$ -photoproduction from complex nuclei. The subroutines we added were carefully scrutinized over the course of many months in order to ensure

that every subcalculation yielded the correct result. Sometimes it was possible to subject the program to more clever tests. For example, by setting the initial and final bound states equal to each other, putting  $\vec{k}_\gamma = \vec{k}_\eta$ , and setting  $\Gamma$  equal to the  $4 \times 4$  identity matrix, we verified that  $\mathcal{Z}$ , as given by (2.72), was indeed equal to one. We also verified that the summations over  $L$  and  $M$  in (3.69) are indeed bounded by the selection rule

$$L \leq J_B + J_{B'} + 1 \quad (3.99)$$

which is obtained by a detailed inspection of (3.92) and (3.93).

The program `dw.for`, accompanied by the documentation file `dw.doc`, calculates the observables in the DWA. This code was obtained by modifying `pw.for`, so that many of the programming tests carry over. In `dw.for`, we have summations over  $L_\eta$ ,  $M_\eta$ , and  $L_\gamma$ . The additional summation, as compared to the PWA, implies that none of these summations is bounded from above by selection rules such as (3.99). Therefore, we needed to verify that these summations converged. Since the time and memory required to perform a DWA calculation is a very nonlinear function of the maximum number of partial waves, it was important to carry these summations no further than was absolutely necessary. We found that the differential cross sections converged to at least six decimal places when the  $L_\eta$  and  $L_\gamma$  summations were truncated at 30. The next test of `dw.for` involved a DWA calculation with the optical potential  $U(r)$  set to zero. As expected, the  $\eta$  meson radial wavefunctions matched the corresponding spherical Bessel functions and the observables were identical to those of the corresponding PWA calculation. Having completed this very important test, we then included non-zero optical potentials in a DWA calculation and verified that the  $\eta$  meson wavefunctions were properly distorted.

## Chapter 4

### Results for the Reaction $A(\gamma, \eta)A^*$

Having derived manageable expressions for the observables in an incoherent  $\eta$ -photoproduction reaction on a complex nucleus, we are now in a position to examine the actual results of the calculations. In the first part of this chapter, we will present the results of our model calculations. Here, we will examine the effects of certain parts of our model relative to the rest. For example, some studies of other types of  $\eta$ -photoproduction reactions have indicated that near threshold the reaction is dominated by the formation of the  $S_{11}(1535)$  resonance. We will investigate whether or not this behavior carries over to our reaction. Also, we are keenly interested in the effects of the final state interactions that are included in the DWA.

In the second part of this chapter, we will make some modifications to our model in order to account more realistically for the effects of nuclear structure. In particular, we will examine the consequences of these modifications to our calculations for the  $2^+$  excited states of  $^{12}\text{C}$ . We then intend to compare these results to the incoherent  $\eta$ -photoproduction calculations performed by Bennhold and Tanabe [1] using a very different approach.

In the third part of this chapter, we will repeat some of our model calculations using a different parameter set. Our objective will be to examine the sensitivity of our calculated cross sections to the set of parameters used.

## 4.1 Model Calculations

### 4.1.1 The $^{16}\text{O}(\gamma, \eta)^{16}\text{O}^*(3^-; 7.88)$ Reaction

The reaction threshold for an  $^{16}\text{O}$  target, as given by equation (3.27), is about 560 MeV. Conversely, the accuracy of the model that we are using becomes questionable beyond 1 GeV as other resonances begin to play a more significant role and additional diagrams must be introduced. Therefore, we have performed our calculations with photon energies ranging from 575 MeV to 975 MeV. We will focus on the photon energies of 600 MeV, 750 MeV, and 900 MeV to illustrate some of the features of our results. Figure 4.1 displays the differential cross sections, averaged over both photon polarizations, for the  $^{16}\text{O}(\gamma, \eta)^{16}\text{O}^*(3^-; 7.88)$  reaction with  $E_\gamma = 600$  MeV. The upper graph shows the shape of the differential cross sections, as a function of  $\theta_\eta$ , in the PWA and in the DWA, using both the DW1 and DW3 optical potentials. The lower graph shows the differential cross sections for the diagrams corresponding to each of the five contributing  $\Gamma$  operators, along with the total differential cross section, in the DWA using the DW1 optical potential. Figure 4.2 and Figure 4.3 display the same information as Figure 4.1, except with photon energies of 750 MeV and 900 MeV, respectively.

Examining the upper graph in Figure 4.1, we see that the overall shape of the differential cross sections, as a function of  $\theta_\eta$ , is somewhat like half of a Gaussian distribution. The differential cross sections in the DWA are lower than the corresponding PWA differential cross section, but the shapes are essentially

the same. Turning to the lower graph, we see that the total differential cross section results almost entirely from the contribution of the  $S_{11}(1535)$  resonance. The  $\rho$  and  $\omega$  vector mesons, along with the  $D_{13}(1520)$  resonance and the proton poles, make minor contributions, and the  $P_{11}(1440)$  resonance contribution is negligible. Turning our attention to the upper graph of Figure 4.2, we notice that although the shapes of the differential cross sections have not changed, they have shifted toward decreasing  $\theta_\eta$ . The magnitudes of the peaks of the differential cross sections have increased by a factor of about seven from those of Figure 4.1. In the lower graph, there is now significant interference between the  $S_{11}(1535)$  channel and the other reaction channels, despite the fact that the size of the  $S_{11}(1535)$  differential cross section relative to the others has not changed appreciably. Finally, in Figure 4.3, we see in the upper graph that the differential cross sections have decreased slightly from those of Figure 4.2. The DW1 optical potential does not suppress the PWA differential cross section as much as the DW3 optical potential does. The shape of the differential cross sections is still unchanged but there is further scaling toward decreasing  $\theta_\eta$ . In the lower graph, there is substantial interference between the  $S_{11}(1535)$  channel and the other reaction channels. The  $D_{13}(1520)$  resonance, the proton pole, and the vector meson reaction channels are beginning to produce larger differential cross sections. In addition, the shapes of the proton and vector meson differential cross sections are noticeably different from that of the total differential cross section.

Now we turn to the photon asymmetry, as defined in (2.111). Figure 4.4 displays the photon asymmetry, as a function of  $\theta_\eta$ , in the PWA and in the DWA using both the DW1 and DW3 optical potentials, for the  $^{16}\text{O}(\gamma, \eta)^{16}\text{O}^*(3^-; 7.88)$  reaction with  $E_\gamma = 600$  MeV. Figure 4.5 and Figure 4.6 display the same in-

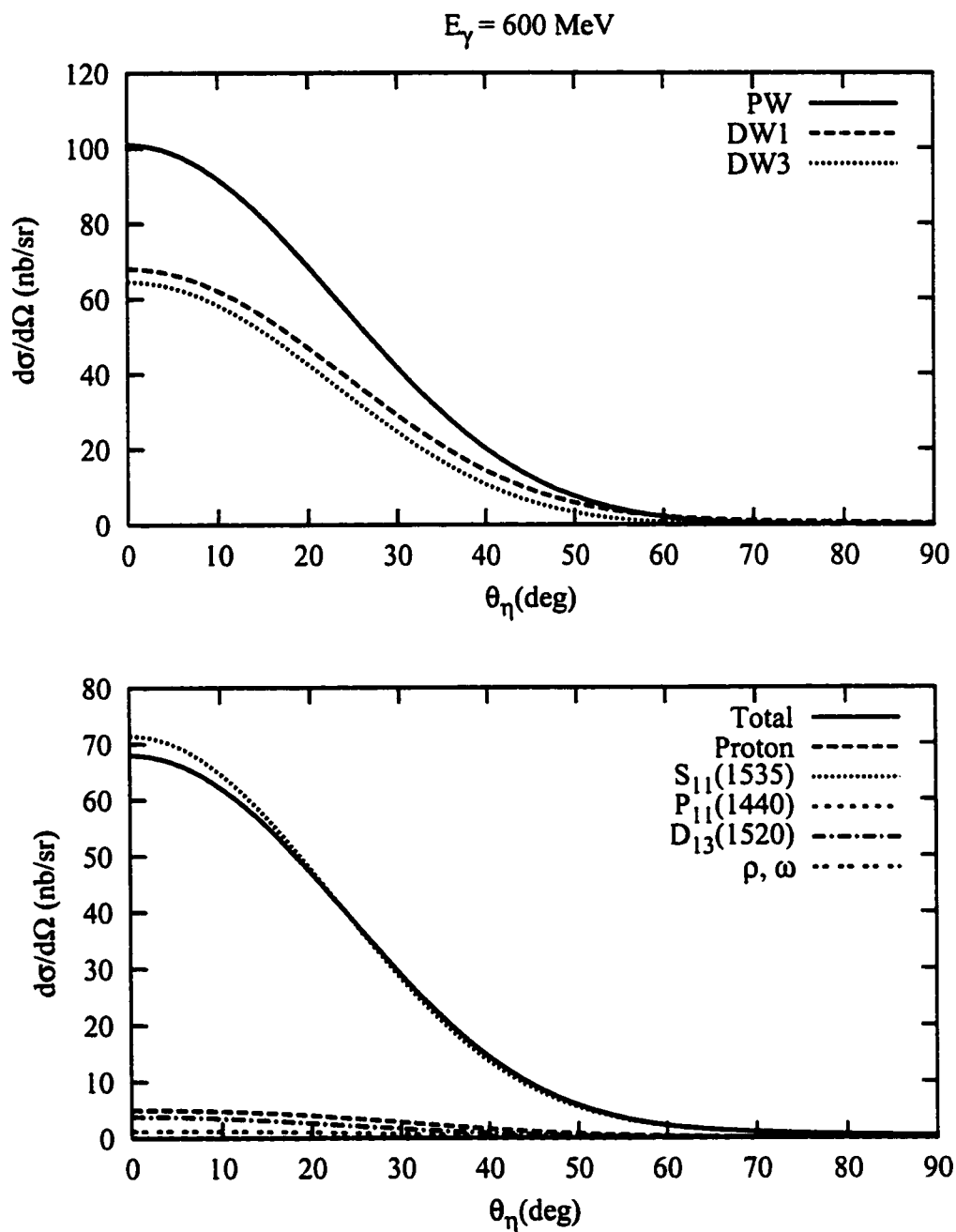


Figure 4.1: Differential cross sections for the  $^{16}\text{O}(\gamma, \eta)^{16}\text{O}^*(3^-; 7.88)$  reaction with  $E_\gamma = 600 \text{ MeV}$ . The upper graph shows the total differential cross sections. The lower graph shows the contributions to the DW1 differential cross section from the individual diagrams.



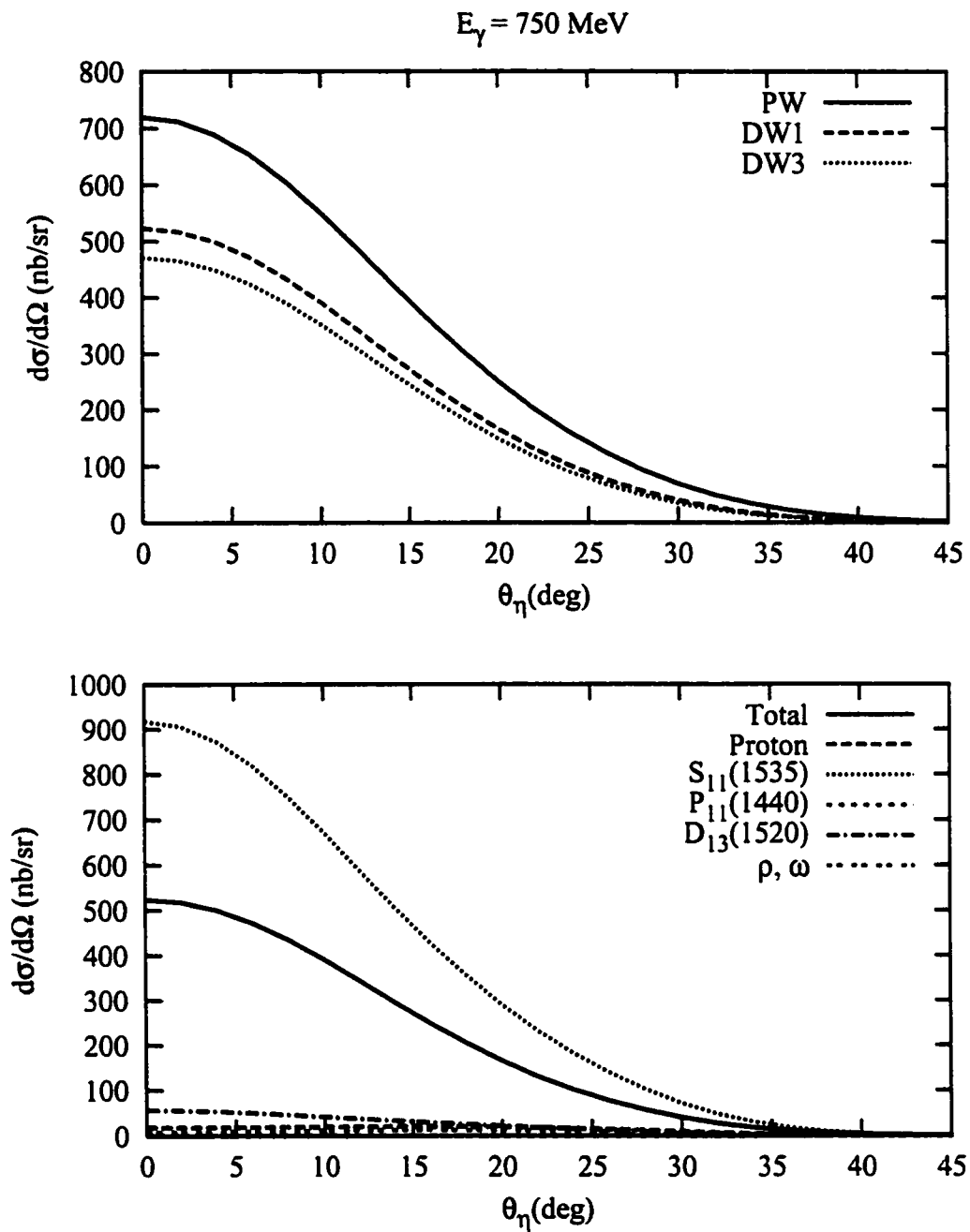


Figure 4.2: Differential cross sections for the  $^{16}\text{O}(\gamma, \eta)^{16}\text{O}^*(3^-; 7.88)$  reaction with  $E_\gamma = 750 \text{ MeV}$

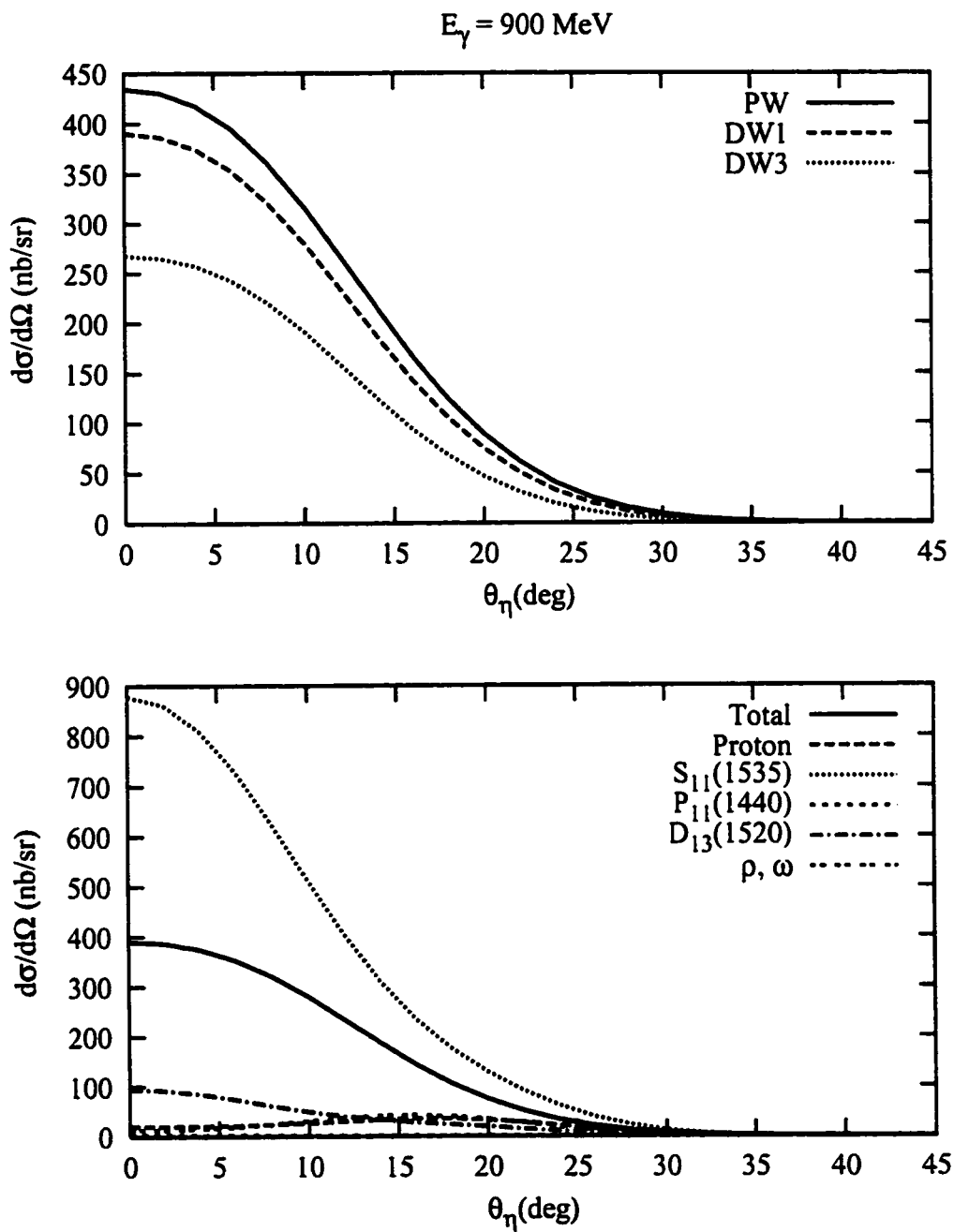


Figure 4.3: Differential cross sections for the  $^{16}\text{O}(\gamma, \eta)^{16}\text{O}^*(3^-; 7.88)$  reaction with  $E_\gamma = 900 \text{ MeV}$

formation as Figure 4.4, except with photon energies of 750 MeV and 900 MeV, respectively. The significant feature of these graphs is that the photon asymmetry is very small for those values of  $\theta_\eta$  where the differential cross section is nonnegligible. For larger values of  $\theta_\eta$ , especially for the higher photon energies, the photon asymmetry oscillates wildly between small and large positive values, indicating a strong suppression of the reaction for photons polarized perpendicularly to the reaction plane. Unfortunately, the vanishing differential cross sections at these angles renders this interesting behavior unobservable.

Finally, let us examine the total cross sections. Figure 4.7 displays the total cross sections, as a function of the energy of the incident photon, in the PWA and in the DWA using both the DW1 and DW3 optical potentials, for the  $^{16}\text{O}(\gamma, \eta)^{16}\text{O}^*(3^-; 7.88)$  reaction. We see that for all three curves the total cross section rises somewhat linearly for the first 100 MeV past the reaction threshold. The curves then reach a maximum, after which they slowly tail off for increasing values of  $E_\gamma$ . The maximum cross section for both of the DWA curves is about half that of the PWA maximum. Whereas the DW3 cross sections remain half as large as those of the PW over the entire energy range, the DW1 curve approaches the PW curve for large values of  $E_\gamma$ . Furthermore, the peak cross section for the DW1 curve occurs at  $E_\gamma = 725$  MeV, as opposed to  $E_\gamma = 700$  MeV for the PW and DW3 curves.

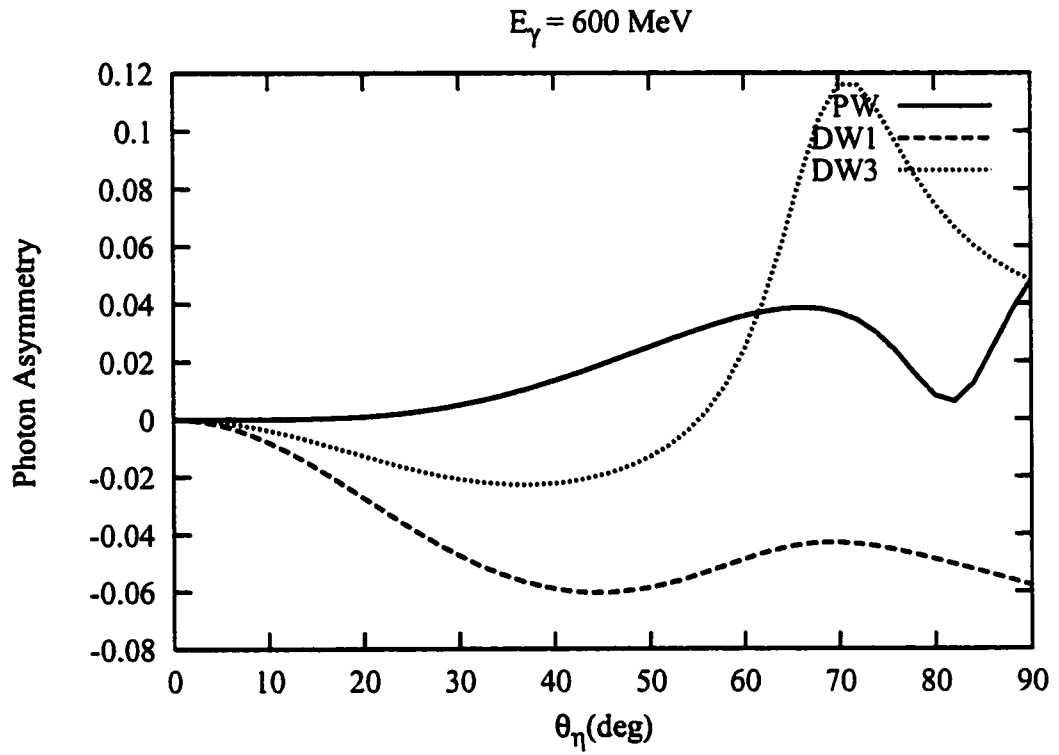


Figure 4.4: Photon asymmetries for the  $^{16}\text{O}(\gamma, \eta)^{16}\text{O}^*(3^-; 7.88)$  reaction with  $E_\gamma = 600 \text{ MeV}$

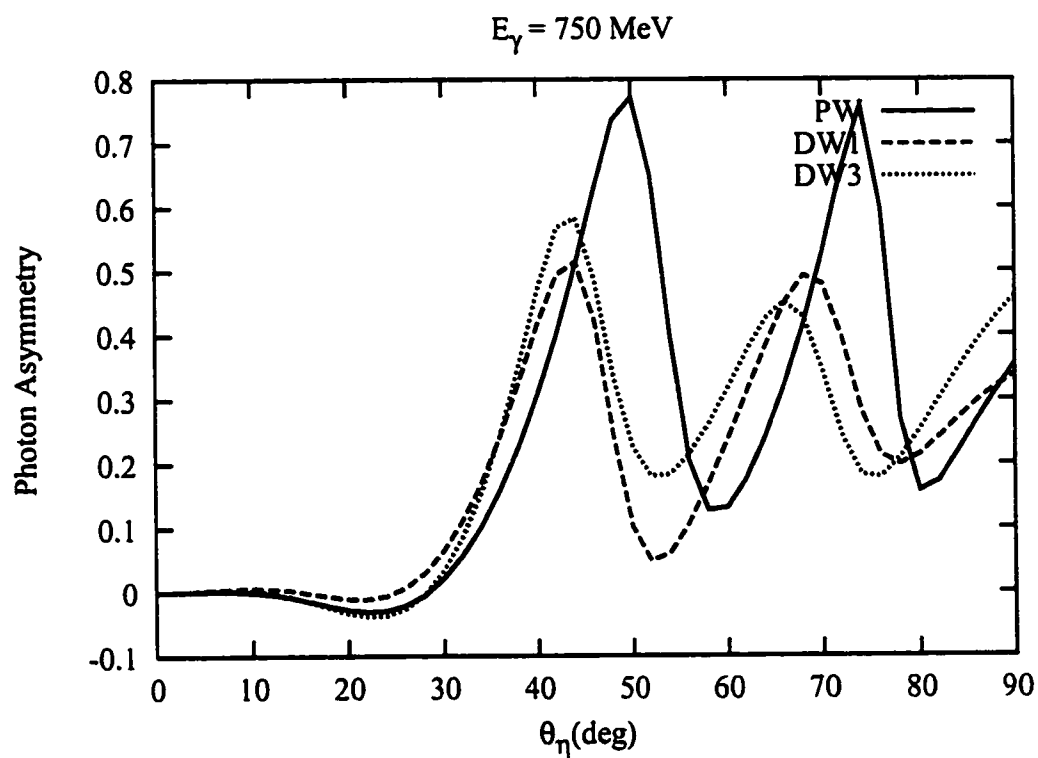


Figure 4.5: Photon asymmetries for the  $^{16}\text{O}(\gamma, \eta)^{16}\text{O}^*(3^-; 7.88)$  reaction with  $E_\gamma = 750 \text{ MeV}$

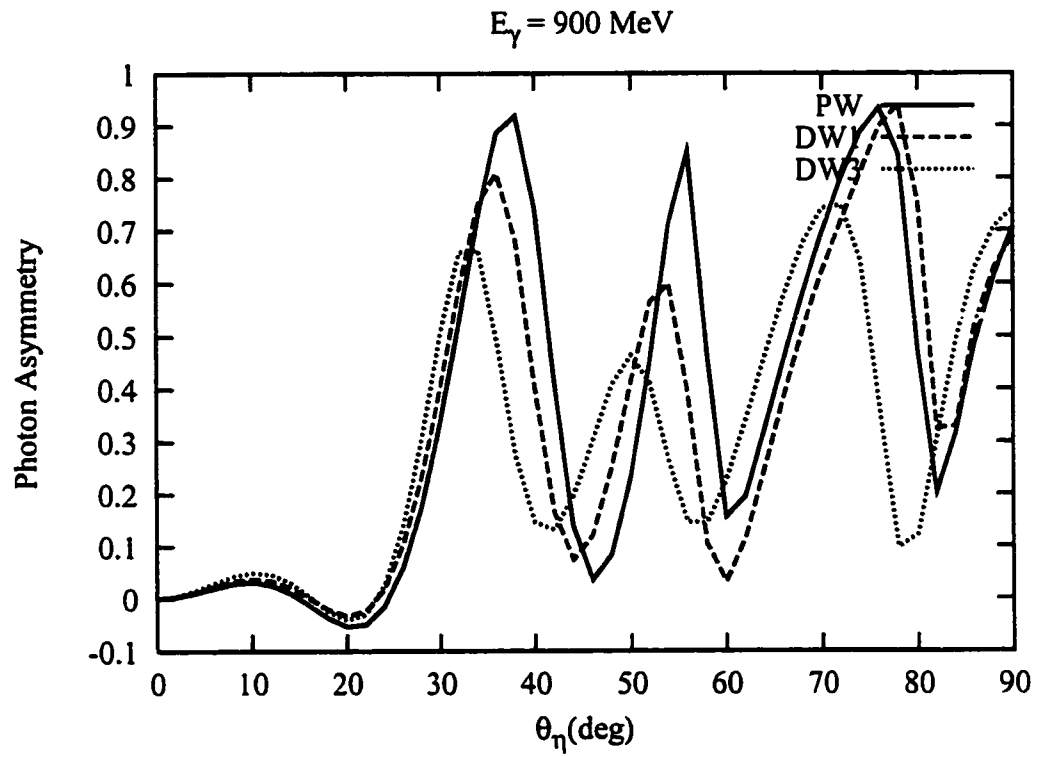


Figure 4.6: Photon asymmetries for the  $^{16}\text{O}(\gamma, \eta)^{16}\text{O}^*(3^-; 7.88)$  reaction with  $E_\gamma = 900 \text{ MeV}$

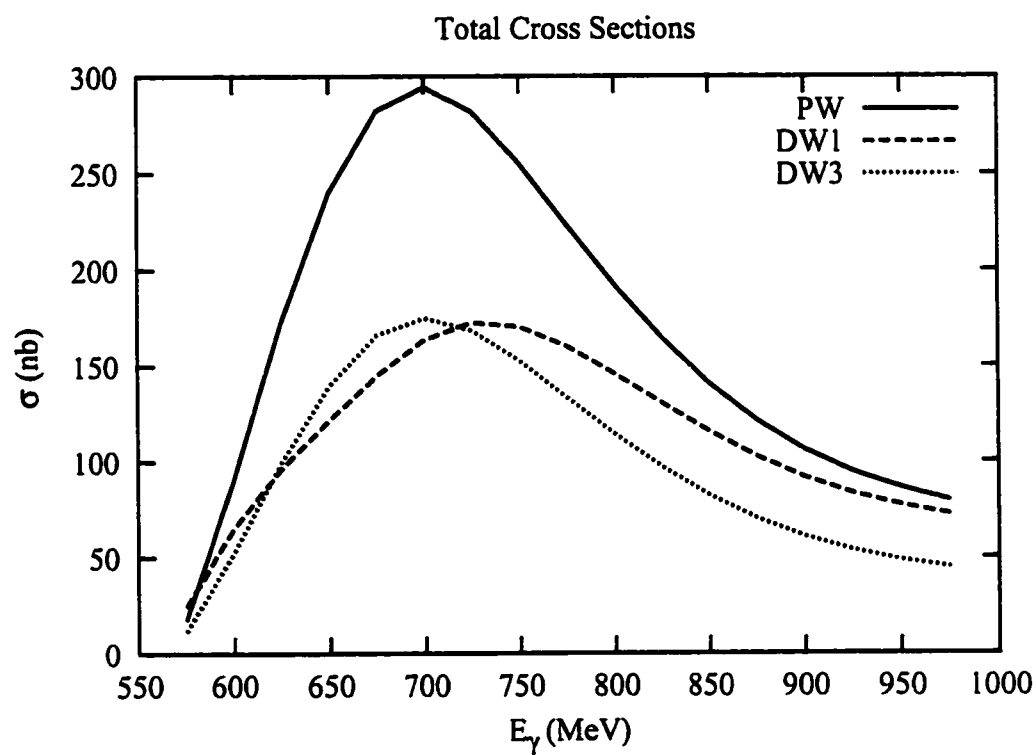


Figure 4.7: Total cross sections for the  $^{16}\text{O}(\gamma, \eta)^{16}\text{O}^*(3^-; 7.88)$  reaction

### 4.1.2 The $^{12}\text{C}(\gamma, \eta)^{12}\text{C}^*(2^+; 4.44)$ Reaction

Switching our attention to a  $^{12}\text{C}$  target, we will first consider an excitation to the  $(2^+; 4.44)$  final state. Figure 4.8 displays the total cross sections, as a function of the energy of the incident photon, in the PWA and in the DWA using both the DW1 and DW3 optical potentials, for the  $^{12}\text{C}(\gamma, \eta)^{12}\text{C}^*(2^+; 4.44)$  reaction. This graph shares most of the features of Figure 4.7, but with two minor differences. First, the maximum magnitudes of the total cross sections are larger than those of the corresponding  $^{16}\text{O}$  curves by a factor of about three. Second, the PW and DW3 curves peak at  $E_\gamma = 675$  MeV, some 50 MeV lower than the DW1 curve.

Figure 4.9 shows the contributions to the differential cross section from the different diagrams for the  $^{12}\text{C}(\gamma, \eta)^{12}\text{C}^*(2^+; 4.44)$  reaction when  $E_\gamma = 750$  MeV. The properties of these curves, apart from an overall scaling, are similar to the differential cross sections shown in Figure 4.2.

### 4.1.3 The $^{12}\text{C}(\gamma, \eta)^{12}\text{C}^*(2^+; 16.11)$ Reaction

In order to examine the dependence of the cross sections on the excitation energy of the nuclear final state, we will now consider an excitation to the  $(2^+; 16.11)$  state of  $^{12}\text{C}$ . Figure 4.10 displays the total cross sections, as a function of the energy of the incident photon, in the PWA and in the DWA using both the DW1 and DW3 optical potentials, for the  $^{12}\text{C}(\gamma, \eta)^{12}\text{C}^*(2^+; 16.11)$  reaction. The most striking feature of Figure 4.10 is that the DWA cross sections are of comparable magnitude to the PWA cross sections. In particular, beyond  $E_\gamma = 775$  MeV, the DW1 cross sections exceed those of the PWA. Despite this, a comparison with Figure 4.8 indicates that all the cross sections have dropped by a factor of two or three from the  $E_x = 4.44$  MeV state to the  $E_x = 16.11$  MeV state.



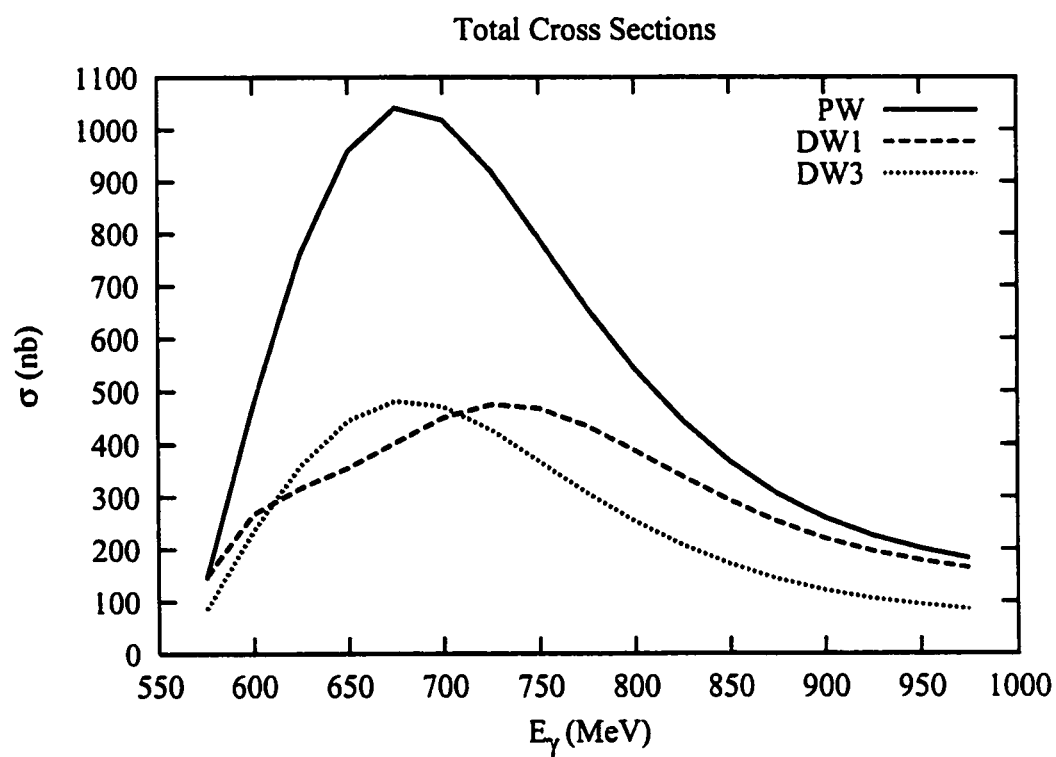


Figure 4.8: Total cross sections for the  $^{12}\text{C}(\gamma, \eta)^{12}\text{C}^*(2^+; 4.44)$  reaction

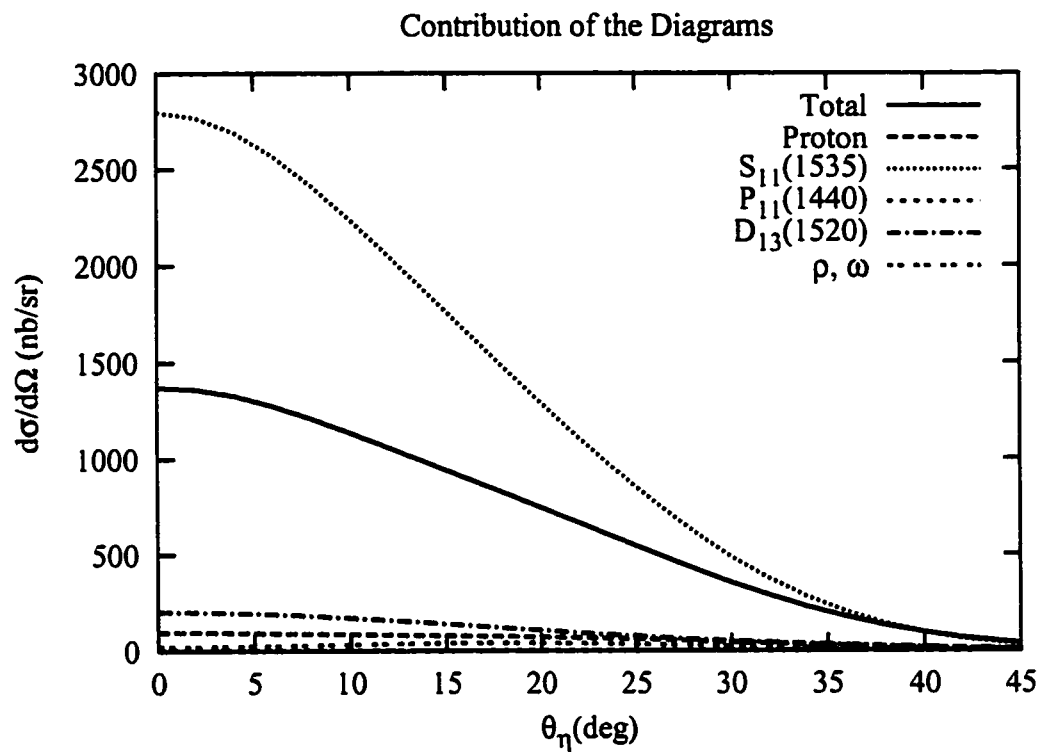


Figure 4.9: Differential cross sections for the  $^{12}\text{C}(\gamma, \eta)^{12}\text{C}^*(2^+; 4.44)$  reaction with  $E_\gamma = 750$  MeV

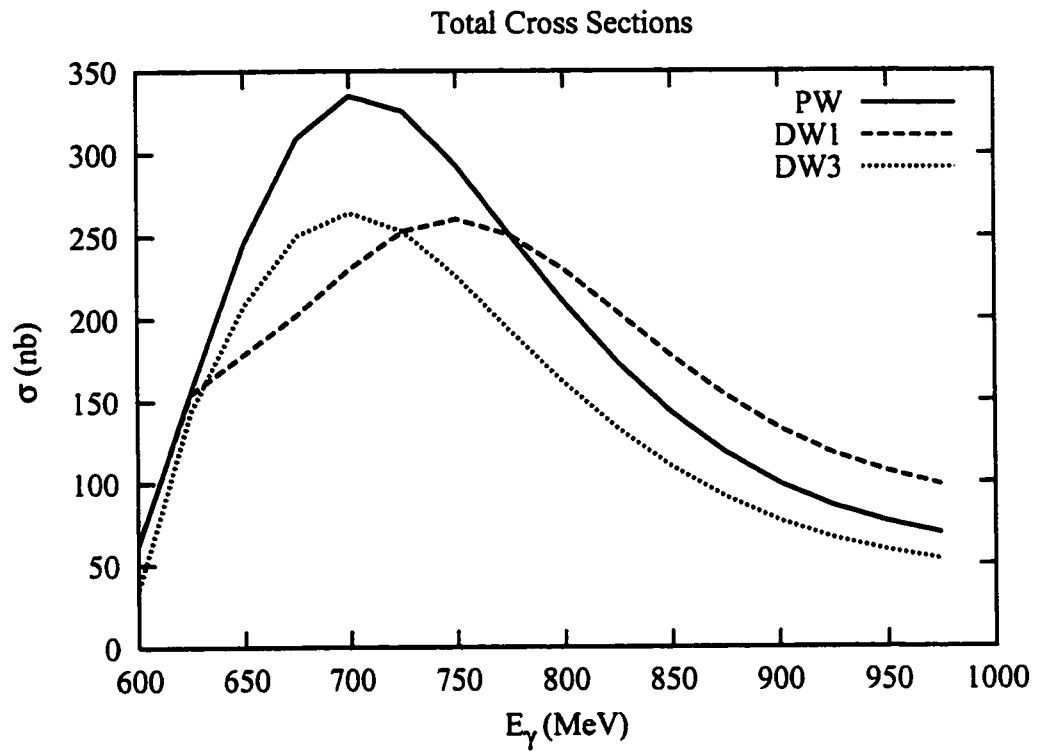


Figure 4.10: Total cross sections for the  $^{12}\text{C}(\gamma, \eta)^{12}\text{C}^*(2^+; 16.11)$  reaction

#### 4.1.4 The $^{12}\text{C}(\gamma, \eta)^{12}\text{C}^*(1^+; 12.71)$ Reaction

Our next objective is to examine the influence of the angular momentum of the final nuclear state on our calculations. In Appendix 3.B, we stated that the  $1p_{\frac{1}{2}} - 1p_{\frac{3}{2}}^{-1}$  transition in  $^{12}\text{C}$  could lead to either of the  $2^+$  states that we have considered so far, as well as the  $1^+$  state at 12.71 MeV. In Figure 4.11 we show the total cross sections for the  $^{12}\text{C}(\gamma, \eta)^{12}\text{C}^*(1^+; 12.71)$  reaction. By comparison with Figure 4.10, we see that the PWA cross sections are very similar to those for the  $(2^+; 16.11)$  final state. On the other hand, both DWA cross sections exhibit a suppression by a factor of about two.

#### 4.1.5 The $^{12}\text{C}(\gamma, \eta)^{12}\text{C}^*(3^-; 9.641)$ Reaction

In Figure 4.12, we show the total cross sections, as a function of the energy of the incident photon, in the PWA and in the DWA using both the DW1 and DW3 optical potentials, for the  $^{12}\text{C}(\gamma, \eta)^{12}\text{C}^*(3^-; 9.641)$  reaction. This graph is virtually identical to Figure 4.8, except that the magnitudes of the total cross sections in Figure 4.12 are 50 % larger.

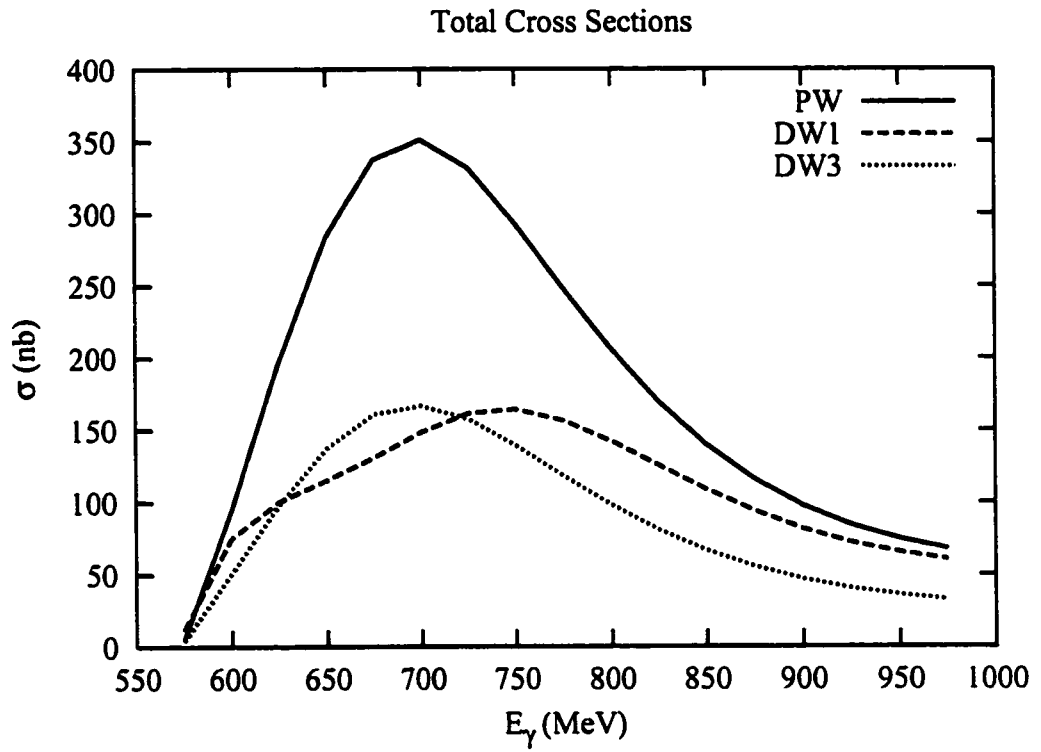


Figure 4.11: Total cross sections for the  $^{12}\text{C}(\gamma, \eta)^{12}\text{C}^*(1^+; 12.71)$  reaction

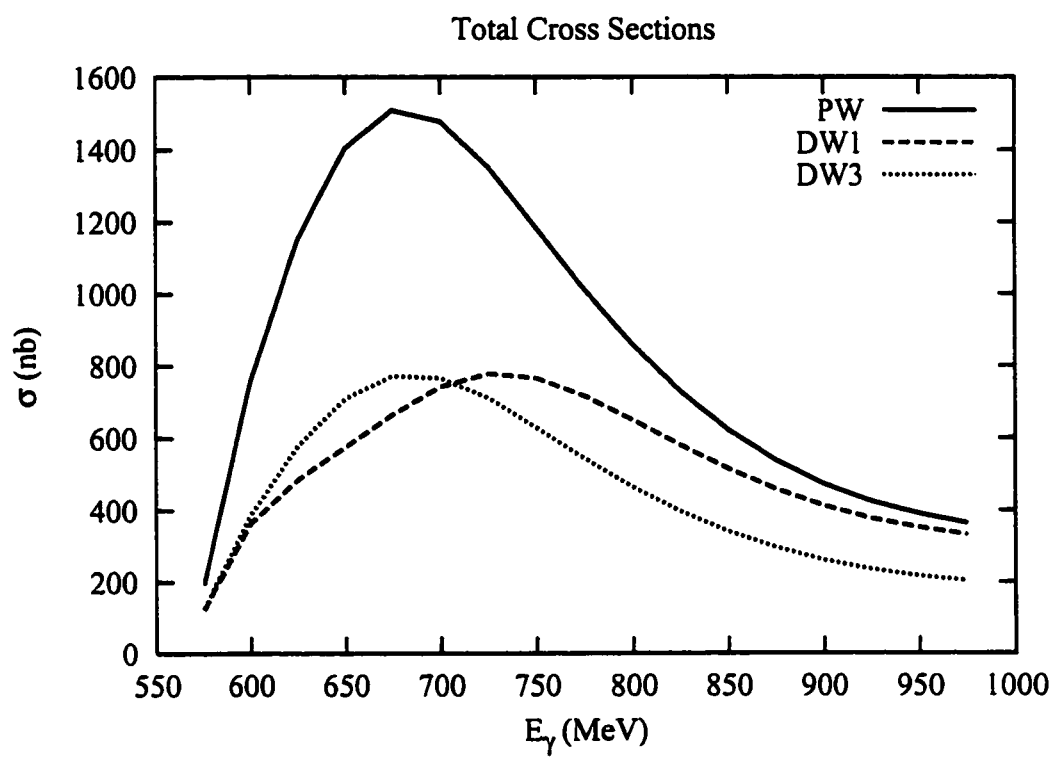


Figure 4.12: Total cross sections for the  $^{12}\text{C}(\gamma, \eta)^{12}\text{C}^*(3^-; 9.641)$  reaction

### 4.1.6 The $^{40}\text{Ca}(\gamma, \eta)^{40}\text{Ca}^*(5^-; 4.48)$ Reaction

Finally, we consider a  $^{40}\text{Ca}$  target. Figure 4.13 displays the total cross sections, as a function of the energy of the incident photon, in the PWA and in the DWA using both the DW1 and DW3 optical potentials, for the  $^{40}\text{Ca}(\gamma, \eta)^{40}\text{Ca}^*(5^-; 4.48)$  reaction. This graph has most of the same properties as the corresponding graphs for the reactions on other targets. The magnitudes of the cross sections are larger than those on an  $^{16}\text{O}$  target, but smaller than those on a  $^{12}\text{C}$  target. Also, the DW1 and DW3 cross sections are slightly smaller, relative to the corresponding PW cross sections, for  $^{40}\text{Ca}$  than for  $^{16}\text{O}$  and  $^{12}\text{C}$ .

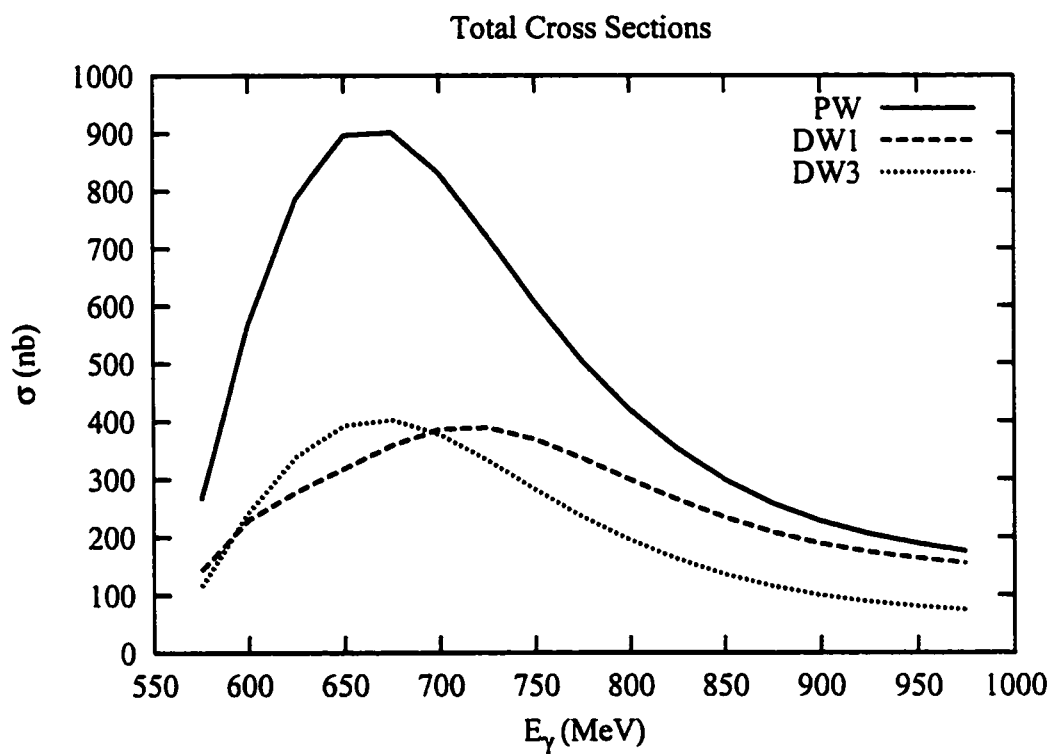


Figure 4.13: Total cross sections for the  $^{40}\text{Ca}(\gamma, \eta)^{40}\text{Ca}^*(5^-; 4.48)$  reaction

### 4.1.7 Discussion of Results

Our calculations have indicated that the  $S_{11}(1535)$  resonance plays a very important role in an incoherent  $\eta$ -photoproduction reaction, especially near threshold. Studies of other  $\eta$ -photoproduction reactions, such as [17], have found similar behavior. We also found that as we moved away from threshold, the other reaction channels began to make larger contributions to the cross section and that these contributions interfered strongly with those of the  $S_{11}(1535)$  resonance.

We performed DWA calculations using two different optical potentials for the  $\eta$  meson. Both the DW1 and the DW3 optical potentials suppressed the PWA cross sections by a factor of about two in the energy region with  $E_\gamma$  near 750 MeV. Whereas the DW3 optical potential provided such a suppression over the entire range of  $E_\gamma$ , the DW1 optical potential became weaker as  $E_\gamma$  increased past 750 MeV. This behavior of the DW1 potential at higher energies is very interesting, as it seems to suggest that many of the more energetic  $\eta$ -mesons are able to escape from the nuclear vicinity without experiencing significant final-state interactions with the nucleus.

The magnitude of the total cross section for incoherent  $\eta$ -photoproduction does not appear to be correlated with the size of the target nucleus. Our model creates this effect by allowing only those nucleons in the outermost filled shell to take part in the interaction. This is a reasonable limitation because we are considering only low-lying nuclear excited states; such states usually arise from simple  $1p - 1h$  configurations involving the outermost filled shell. We attribute the differences in the magnitudes of the total cross sections in Figures 4.7, 4.8, 4.10, 4.11, 4.12, and 4.13 to the sensitivity of the contributions to the total cross section from individual diagrams to the changes in the angular momentum quantum numbers of the nucleus and the interacting nucleon.



## 4.2 Realistic Modifications to the Model

In the model calculations that we have performed thus far, we have used a very simple description of nuclear structure. Unfortunately, the nucleus is an intricate many-body system that cannot always be accurately described in such a simple manner. Therefore, we will now introduce some modifications to our model that will more accurately account for the realities of nuclear structure. By applying these modifications to our existing calculations, we will obtain reasonable predictions for the cross sections of incoherent  $\eta$ -photoproduction processes.

### 4.2.1 Isospin Considerations

In Appendix 3.B, we deduced the final state spectroscopic factor by picking a specific excited state for the recoiling nucleus and examining its shell model configurations. For example, for the reaction on  $^{12}\text{C}$ , in the case where we specify the final state to be the  $(2^+; 4.44)$  state, we concluded that this state essentially corresponds to the transition of a nucleon from the  $1p_{3/2}$  shell to the  $1p_{1/2}$  shell. It is tempting to assume that there is a one-to-one correspondence between the set of shell model transitions and the set of nuclear excited states. This is not the case, because if we choose the  $(2^+; 16.11)$  state to be our final state instead, we find that this state is also almost completely described by the  $1p_{1/2} - 1p_{3/2}^{-1}$  configuration [30]. As a result, specifying the shell transition does not completely determine the final state of the nucleus. One of the tools that we will require in order to address this difficulty is the notion of isospin symmetry.

Isospin symmetry formalizes the symmetry of protons and neutrons, collectively known as nucleons, with respect to the strong interaction. In direct analogy to the description of the spin of an electron in quantum mechanics, we regard

the proton and the neutron as the two states of a two-component spinor residing in isospin space. We can then label any composite group of nucleons by two isospin quantum numbers:  $T$  and  $T_z$ . In particular, we can assign the quantum number  $T$ , commonly called the isospin, to nuclei and their excited states.  $T_z$  is easily obtained by subtracting the number of neutrons in a nucleus from the number of protons and dividing by two. In general, we will describe a nuclear state with the notation  $(J^\pi T; E_x)$  where  $E_x$  is in MeV. For closed-shell nuclei like  $^{12}\text{C}$ ,  $^{16}\text{O}$ , and  $^{40}\text{Ca}$ , the ground state is  $(0^+0; 0)$ . When we create an excited state from a  $1p - 1h$  transition, we are coupling a nucleon with a core. Both are isospin- $\frac{1}{2}$  objects, so the excited state will be either an isoscalar state with  $T = 0$ , or an isovector state with  $T = 1$ . For the two  $2^+$  excited states of  $^{12}\text{C}$  that we have been considering, it turns out that the state at 4.44 MeV is an isoscalar state and that the state at 16.11 MeV is an isovector state.

In our calculations so far, we have not explicitly taken isospin into account. On the other hand, in Appendix 3.B we discussed the results of an experiment at MAMI [4] which indicates that  $\eta$ -photoproduction reactions distinguish between the protons and neutrons in the target. We will now incorporate some isospin considerations into our model so that we can address the relative likelihoods of exciting isoscalar and isovector nuclear states.

Consider the amplitude,  $\mathcal{A}_p$ , with which an incident photon interacts with a specific proton in our target so that an  $\eta$  meson is photoproduced. Similarly, let  $\mathcal{A}_n$  designate the corresponding amplitude for  $\eta$ -photoproduction from a specific neutron in our target. Since, from equation (3.96), we have

$$\frac{\sigma_n}{\sigma_p} = \frac{2}{3} \quad (4.1)$$

we know that

$$|\mathcal{A}_n| = \sqrt{\frac{2}{3}} |\mathcal{A}_p| \quad (4.2)$$

We do not know, however, the relative phase between these amplitudes yet. With the assumption that the reaction proceeds through the formation of the  $S_{11}(1535)$  resonance, Krusche *et al.* [4] have determined that

$$\mathcal{A}_n = (-0.80) \mathcal{A}_p \quad (4.3)$$

As we shall soon see, the fact that  $\mathcal{A}_n$  and  $\mathcal{A}_p$  have opposite phases has significant implications for the connection between the magnitude of the cross section and the isospin of the recoiling nucleus.

For incoherent  $\eta$ -photoproduction on an isospin-zero target, the recoiling nucleus must be in either a  $T = 0$  or a  $T = 1$  state. Since the proton and the neutron correspond to isospin states of  $|\frac{1}{2}, \frac{1}{2}\rangle$  and  $|\frac{1}{2}, -\frac{1}{2}\rangle$ , respectively, we can write

$$\mathcal{A}_p = \mathcal{A}_0 + \mathcal{A}_1 \quad (4.4)$$

$$\mathcal{A}_n = \mathcal{A}_0 - \mathcal{A}_1 \quad (4.5)$$

where  $\mathcal{A}_0$  and  $\mathcal{A}_1$  are the amplitudes for isoscalar and isovector  $\eta$ -photoproduction processes on a nucleon, respectively. These equations can be solved for  $\mathcal{A}_0$  and  $\mathcal{A}_1$  to yield

$$\mathcal{A}_0 = \frac{1}{2} (\mathcal{A}_p + \mathcal{A}_n) \quad (4.6)$$

$$\mathcal{A}_1 = \frac{1}{2} (\mathcal{A}_p - \mathcal{A}_n) \quad (4.7)$$

Using (4.3), we then have

$$\mathcal{A}_0 = (0.1) \mathcal{A}_p \quad (4.8)$$

$$\mathcal{A}_1 = (0.9) \mathcal{A}_p \quad (4.9)$$

In our model, we calculate  $\mathcal{A}_p$ . Previously, we did not specify the isospin of the final state and accounted for the effects of neutrons by multiplying  $\sigma_p$  by  $\frac{5}{3}$ . Based on (4.8) and (4.9), a more detailed treatment of isospin leads to the following expressions for the total  $\eta$ -photoproduction cross sections for isoscalar and isovector transitions:

$$\sigma_0 = \frac{3}{5} (0.01) \sigma_{TOT} \quad (4.10)$$

$$\sigma_1 = \frac{3}{5} (0.81) \sigma_{TOT} \quad (4.11)$$

where  $\sigma_{TOT}$  represents the total cross section as obtained in our previous model calculations. As we can see, the isoscalar cross section is heavily suppressed relative to the isovector cross section.

### 4.2.2 Realistic Spectroscopic Factors

In our calculations so far, we have imposed perfect shell structure. By this, we mean that the spectroscopic factors take on their maximum allowed values and that the motion of each of the nucleons is independent. For the initial spectroscopic factor, this implies that the target nucleus is in its ground state, which is assumed to have all of the lowest-lying shells completely filled. For the final spectroscopic factor, we assume that a given final state consists of a single  $1p - 1h$  configuration. In Appendix 3.B, we justified these assumptions by referring to the shell model calculations of Gillet *et al.* [30, 31]. This justification is somewhat specious, however, since these shell model calculations explicitly restrict the model space to  $1p - 1h$  configurations. A more realistic set of shell model calculations was performed by Cohen and Kurath [32, 33]. They studied the  $p$ -shell nuclei under the assumption that, above an  $\alpha$ -particle core of  $s$ -shell nucleons, all of the  $p$ -shell nucleons are interacting with each other. As a result,

the model space for excited states is not confined to  $1p-1h$  configurations. Using this model, they determined spectroscopic factors that are more realistic than the ones that we have been using so far. For a  $^{12}\text{C}$  target, the initial spectroscopic factor is

$$\left[ \mathcal{S}_{0\frac{3}{2}} \left( \frac{3}{2} \right) \right] = 2.85 \quad (4.12)$$

In other words, the  $1p_{\frac{3}{2}}$  shell is less than three-quarters full when  $^{12}\text{C}$  is in its ground state. The final spectroscopic factor for excitation to the  $(2^+0; 4.44)$  state of  $^{12}\text{C}$  is

$$\left[ \mathcal{S}_{2\frac{3}{2}} \left( \frac{1}{2} \right) \right]_{T=0} = 0.55 \quad (4.13)$$

Similarly, for excitation to the  $(2^+1; 16.11)$  state of  $^{12}\text{C}$ , we have

$$\left[ \mathcal{S}_{2\frac{3}{2}} \left( \frac{1}{2} \right) \right]_{T=1} = 0.28 \quad (4.14)$$

### 4.2.3 Transforming to the Center of Momentum Frame

We have performed our calculations in the laboratory (LAB) frame. This is also the frame in which experimental results have been reported for  $\eta$ -photoproduction on complex nuclei [5]. On the other hand, since a target such as  $^{12}\text{C}$ ,  $^{16}\text{O}$ , or  $^{40}\text{Ca}$  is very massive in comparison to the energy of the incident photon, it might seem reasonable to assume that the calculations would hardly differ in the center of momentum (CM) frame. For convenience, most theoretical calculations for incoherent  $\eta$ -photoproduction, including those of Bennhold and Tanabe [1], take place in the CM frame. We will now show how we can translate our calculations to the CM frame.

The fundamental idea, when considering the relationship between the differential cross sections in the CM and LAB frames, is that an event which produces an  $\eta$  meson and leaves the nucleus in a specific final state must be recognized

as an event in any frame. In other words, the total number of event counts is independent of the frame. The total number of event counts in a given frame can be calculated by integrating the product of the cross section and the luminosity over the time in which the beam was active. Since the luminosity is proportional to the flux, we conclude that

$$J_{CM} \sigma_{CM} = J_{LAB} \sigma_{LAB} \quad (4.15)$$

where the incident flux is defined by

$$J = \frac{v_{rel}}{(2\pi)^3} \quad (4.16)$$

In the LAB frame, the photon is incident on a stationary target, so  $v_{rel} = 1$ . In the CM frame, the target is moving toward the photon, so  $v_{rel} > 1$ . Therefore, the total CM cross section, as given by equation (4.15), is slightly smaller than the total LAB cross section:

$$\sigma_{CM} = \frac{1}{1 + (|\vec{p}_T|/E_T)_{CM}} \sigma_{LAB} \quad (4.17)$$

The cross sections  $\sigma_{CM}$  and  $\sigma_{LAB}$  are obtained by integrating over the differential cross sections  $\left(\frac{d\sigma}{d\Omega_\eta}\right)_{CM}$  and  $\left(\frac{d\sigma}{d\Omega_\eta}\right)_{LAB}$ , respectively. These differential cross sections are related by [34]:

$$\left(\frac{d\sigma}{d\Omega_\eta}\right)_{CM} = \frac{1}{1 + (|\vec{p}_T|/E_T)_{CM}} \frac{p_\eta'^2 E_\eta}{p_\eta^2 E_\eta'} \left(\frac{d\sigma}{d\Omega_\eta}\right)_{LAB} \quad (4.18)$$

The first factor in (4.18) accounts for the apparent difference in flux observed in the two frames. The second factor is the Jacobian that relates the phase space volume element  $d^3\vec{p}_\eta$  in the two frames. Here, the primed variables denote the CM frame and the unprimed variables denote the LAB frame.

When we apply equation (4.18) to our LAB frame differential cross section for a 650 MeV photon incident on  $^{12}\text{C}$ , we find that the CM differential cross

sections at forward scattering angles are reduced by a factor of about 1.27. For lower photon energies or for more massive targets, we would expect the effect to be smaller.

#### 4.2.4 Results of the Modified Calculations

We will now examine the results of these modifications in the context of calculations where a 650 MeV photon is incident on  $^{12}\text{C}$ , and the nucleus is excited to either the  $(2^+0; 4.44)$  state or the  $(2^+1; 16.11)$  state. Using our original model, the differential cross sections in the LAB frame for these two processes are shown in Figure 4.14. The DW curves were obtained using the DW1 optical potential. Based on the isospin analysis that we performed in Section 4.2.1, we now realize that these differential cross sections have already been implicitly summed over the isospin of the final state. We have applied the modifications discussed in this section to these model calculations for the differential cross sections for the  $^{12}\text{C}(\gamma, \eta)^{12}\text{C}^*(2^+0; 4.44)$  and the  $^{12}\text{C}(\gamma, \eta)^{12}\text{C}^*(2^+1; 16.11)$  reactions. The results of these modified calculations, expressed in the CM frame, are displayed in Figure 4.15. Comparing Figure 4.14 and Figure 4.15, we see two major features. First, there is a substantial lowering of the differential cross sections. For the case of the isoscalar transition, the differential cross sections are lowered by a factor of about 500! Conversely, for the isovector transition, the differential cross sections are only lowered by a factor of about 10. This isospin discrepancy, resulting mainly from equations (4.10) and (4.11), comprises the other major feature of our modified calculations.

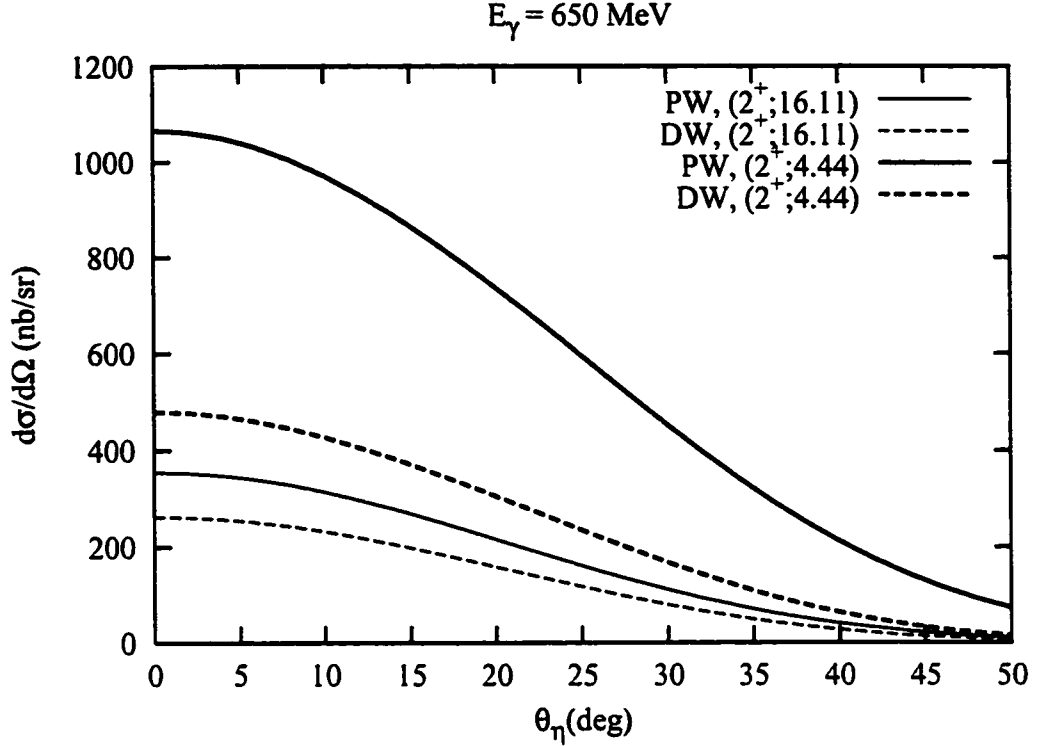


Figure 4.14: Model calculations for the  $^{12}\text{C}(\gamma, \eta)^{12}\text{C}^*(2^+; 4.44)$  and  $^{12}\text{C}(\gamma, \eta)^{12}\text{C}^*(2^+; 16.11)$  reactions

#### 4.2.5 Discussion of Results

Having completed realistic calculations for the  $^{12}\text{C}(\gamma, \eta)^{12}\text{C}^*(2^+0; 4.44)$  and the  $^{12}\text{C}(\gamma, \eta)^{12}\text{C}^*(2^+1; 16.11)$  reactions, we would like to see how our results compare with other calculations for similar  $\eta$ -photoproduction processes. In particular, we would like to examine the relative sizes of coherent, incoherent, and quasifree cross sections.

The only other theoretical study of incoherent  $\eta$ -photoproduction was performed by Bennhold and Tanabe [1] nearly a decade ago using a nonrelativistic model. In Figure 4.16, we show the results of their calculations for the



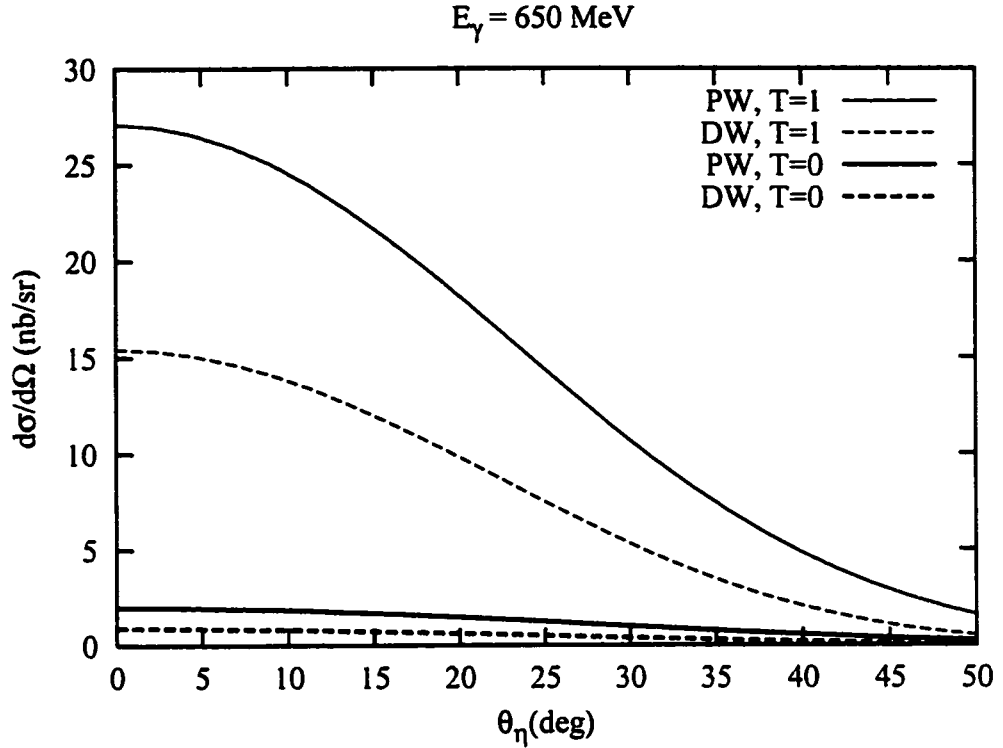


Figure 4.15: Modified calculations for the  $^{12}\text{C}(\gamma, \eta)^{12}\text{C}^*(2^+0; 4.44)$  and  $^{12}\text{C}(\gamma, \eta)^{12}\text{C}^*(2^+1; 16.11)$  reactions

$^{12}\text{C}(\gamma, \eta)^{12}\text{C}^*(2^+0; 4.44)$  and the  $^{12}\text{C}(\gamma, \eta)^{12}\text{C}^*(2^+1; 16.11)$  reactions. A comparison with Figure 4.15 reveals that the shapes of the differential cross sections, as well as the relative magnitudes of the isoscalar and isovector transitions, are essentially the same in Figure 4.15 as they are in Figure 4.16. The actual magnitudes of the differential cross sections in our modified calculations are lower than those of Bennhold and Tanabe by a factor of about two. This behavior, namely, that the relativistic calculations yield cross sections half as large as those of nonrelativistic calculations, carries a precedent. Hedayati-Poor and Sherif [17] studied the quasifree  $\eta$ -photoproduction process using essentially the same reac-

tion model that we are using for the incoherent process. When they examined their results for the inclusive reaction [18], they found that their calculations fell below the results of similar nonrelativistic calculations [11] by a factor of about two. Therefore, our relativistic  $\eta$ -photoproduction model yields results that are qualitatively similar to those of corresponding nonrelativistic models. On the other hand, the quantitative values of the cross sections are smaller in our calculations than in nonrelativistic calculations due to the inherent properties of the relativistic model.

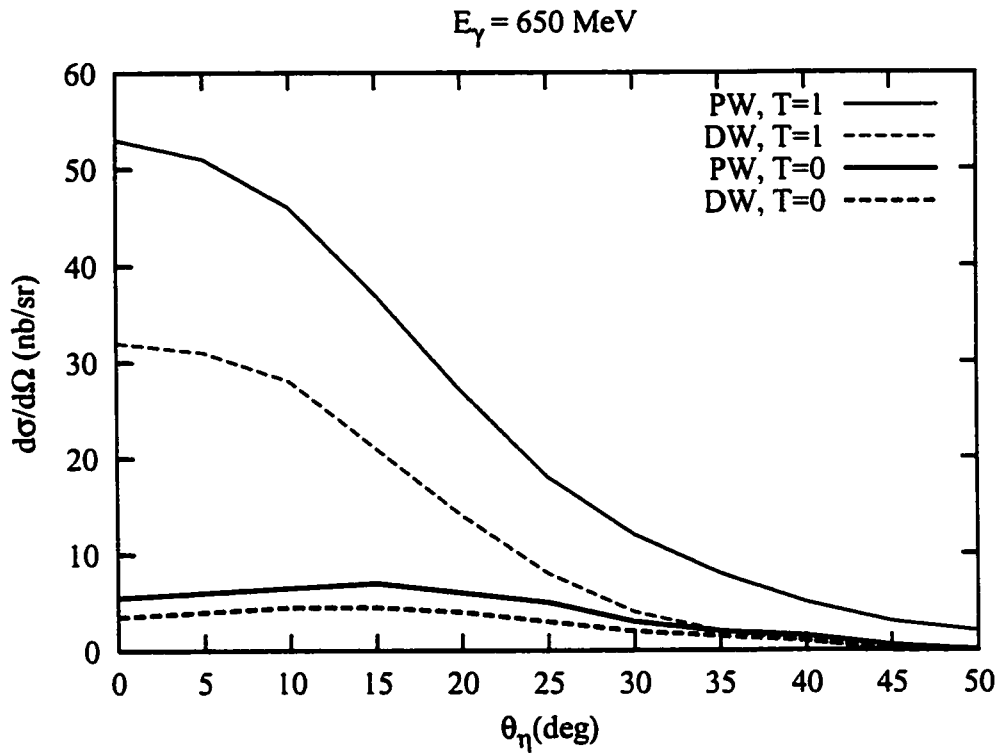


Figure 4.16: Calculations of Bennhold and Tanabe for the angular distributions of the reactions  $^{12}\text{C}(\gamma, \eta)^{12}\text{C}^*(2^+1; 16.11)$  and  $^{12}\text{C}(\gamma, \eta)^{12}\text{C}^*(2^+0; 4.44)$ , as taken from Figure 19 of [1]

Next, we would like to compare the magnitudes of our calculated cross sections for incoherent  $\eta$ -photoproduction processes to the recent MAMI data for the inclusive photoproduction reaction  $A(\gamma, \eta)X$  [5]. For a 650 MeV photon, we can integrate the DW differential cross sections in Figure 4.15 to find the total cross sections for the  $^{12}\text{C}(\gamma, \eta)^{12}\text{C}^*(2^+0; 4.44)$  and  $^{12}\text{C}(\gamma, \eta)^{12}\text{C}^*(2^+1; 16.11)$  reactions. The results are 1 nb and 11 nb, respectively. The experimental measurement for the inclusive cross section yields  $10 \mu\text{b}$  for  $\eta$ -photoproduction on  $^{12}\text{C}$  when  $E_\gamma = 650 \text{ MeV}$ . We conclude that the quasifree process  $A(\gamma, N\eta)A - 1$  is the predominant contributor to the inclusive process and that the incoherent cross sections are several orders of magnitude smaller than the quasifree cross sections. Any attempt to detect incoherent processes in an experiment will face the challenge of distinguishing between incoherent and quasifree reactions and then filtering out the relatively small number of incoherent events.

Finally, we would like to draw a comparison between our calculations for incoherent  $\eta$ -photoproduction and the calculations by Peters *et al.* [20] for coherent  $\eta$ -photoproduction on spin-zero nuclei. For a 650 MeV photon incident on  $^{12}\text{C}$ , they calculate a total coherent cross section of about 2 nb. Calculations by Fix and Arenhövel [16] also yield a total cross section of about 2 nb for coherent  $\eta$ -photoproduction for a 650 MeV photon incident on  $^{12}\text{C}$ . These coherent cross sections are roughly the same size as the cross sections that we have calculated for individual incoherent processes.

In fact, our model can be adapted to study coherent  $\eta$ -photoproduction with only a few modifications. First of all, the initial and final bound state wavefunctions for the interacting nucleon will be the same. As a result, the final spectroscopic factor will be exactly one. Furthermore, every nucleon in the nucleus will participate; not just the ones in the highest filled shell. Therefore, to

the extent that the contributions of the various diagrams for a specific nucleon transition are relatively unchanged, we can expect that the coherent cross section should only be slightly larger than any individual incoherent cross section. In practice, the specific spin and isospin selection rules that govern the coherent process suppress most of the contributions to the reaction amplitude from the  $S_{11}(1535)$  resonance and the  $\rho$  meson so that the coherent cross sections are similar to the incoherent cross sections.

### 4.3 Sensitivity to Parameters

Every model that is based on an effective Quantum Field Theory requires a set of phenomenological parameters to specify all of the couplings, masses, and other constants that appear in the effective Lagrangian. These parameters are usually obtained from experiments involving simple interactions of the different particles in the effective Lagrangian. Unfortunately, it is often very difficult to obtain precise determinations of some of these parameters, and as a result, it is natural to wonder to what extent the final calculations depend on the initial choice of parameters.

The parameters that we have used were obtained by Benmerrouche *et al.* [8] using data for the elementary reaction  $\gamma + p \rightarrow \eta + p$  that predates the recent experiments at MAMI [3]. These parameters do not agree as well with the new elementary reaction data from MAMI. Using the new data, along with the limitation that the only contributing resonances are the  $S_{11}(1535)$  and the  $D_{13}(1520)$ , Fix and Arenhövel [16] have obtained a new set of parameters for the effective Lagrangian. When Hedayati-Poor and Sherif incorporated this new parameter set into their model for inclusive  $\eta$ -photoproduction, they found that

their calculated cross sections increased by about 50 %. This increase in the cross sections brought their results into close agreement with the recent MAMI data for inclusive  $\eta$ -photoproduction from complex nuclei [5]. In Table 4.1, we list all of the changes made by Hedayati-Poor and Sherif in order to implement the new parameter set.

Parameter	Old Value	New Value
$\Gamma_{S_{11}(1535)}$	150 MeV	160 MeV
$g_{\eta NN}$	4.1	2.24
$g_{\eta NS_{11}}$	2.01991	2.0846
$\kappa_{S_{11}}$	0.880317	-0.958
$f_{\eta ND_{13}} \kappa_{D_{13}}^{(1)}$	15.306	37.75
$f_{\eta ND_{13}} \kappa_{D_{13}}^{(2)}$	16.1189	40.0

Table 4.1: Parameters changed in the new parameter set

In order to examine the effects of this new parameter set on our calculations, we will look more carefully at the model calculations for the  $^{12}\text{C}(\gamma, \eta)^{12}\text{C}^*(2^+; 4.44)$  reaction that we first explored in Section 4.1. The modifications that we discussed in Section 4.2 will have no effect on the relative changes in our calculations induced by the new parameter set. Also, we will only consider PWA calculations, since the parameters in the effective Lagrangian only manifest themselves in the  $\Gamma$  matrix operator in expressions for the reaction amplitude such as (2.68).

In Figure 4.17, we show the total PW cross sections, as a function of  $E_\gamma$ , for both parameter sets. This graph shows that the cross sections obtained with the new parameter set are about four times larger than those from the old parameter set.

In Figure 4.18, we show the contributions of the different diagrams to the

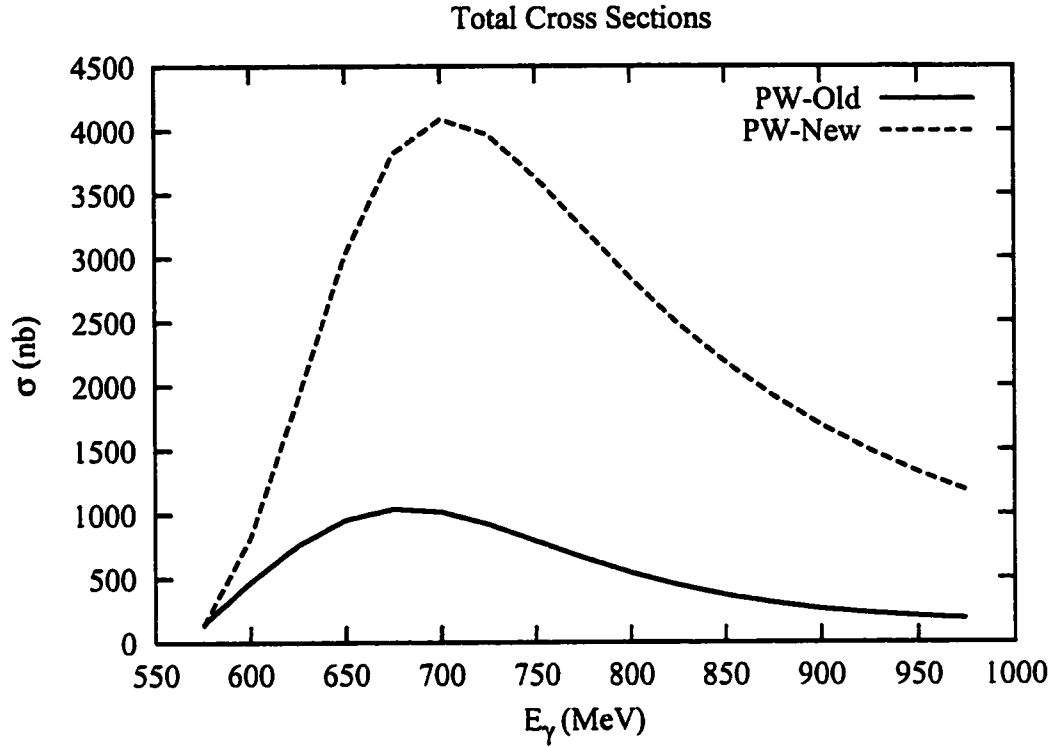


Figure 4.17: Comparison of the total PW cross sections for the  $^{12}\text{C}(\gamma, \eta)^{12}\text{C}^*(2^+; 4.44)$  reaction using different parameter sets

differential cross section when  $E_\gamma = 750$  MeV. We see that the  $S_{11}(1535)$  and the  $D_{13}(1520)$  resonance diagrams provide the only non-negligible contributions to the total differential cross section. The  $S_{11}(1535)$  contribution is about three times that of the  $D_{13}(1520)$ , and the two contributions interfere constructively, so as to make the total differential cross section larger than either of the individual contributions.

As a comparison, we can reexamine Figure 4.9, which showed the differential cross sections for the  $^{12}\text{C}(\gamma, \eta)^{12}\text{C}^*(2^+; 4.44)$  reaction with  $E_\gamma = 750$  MeV using the original parameter set. Here we see that the  $S_{11}(1535)$  contribution is about

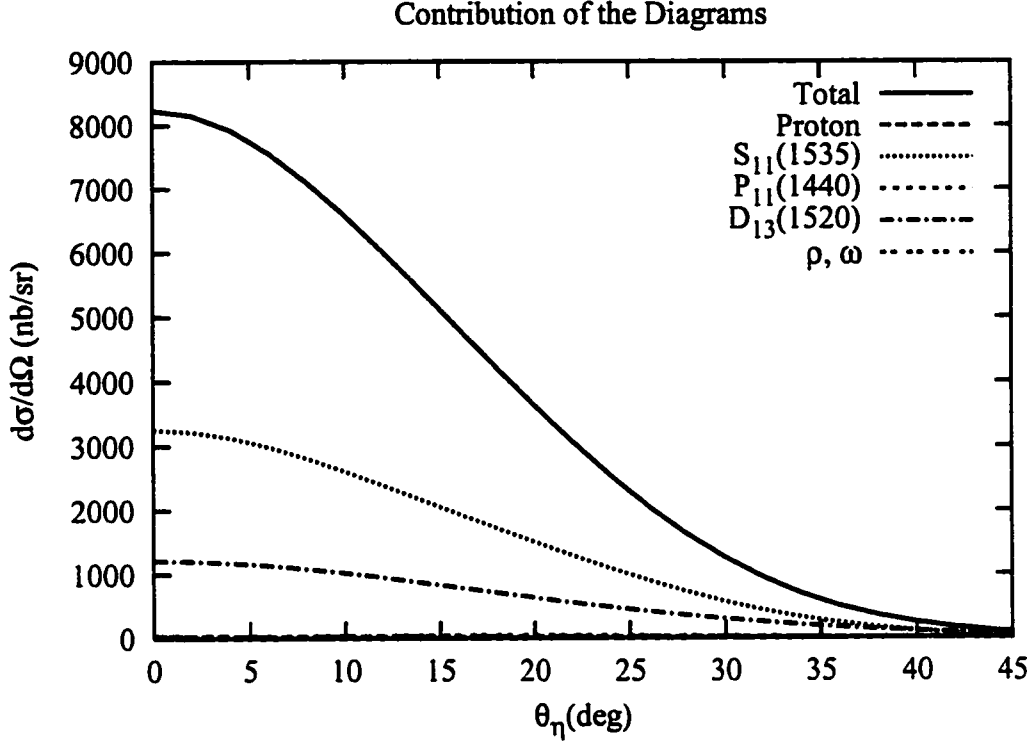


Figure 4.18: Contributions from the different diagrams to the differential cross section of the  $^{12}\text{C}(\gamma, \eta)^{12}\text{C}^*(2^+; 4.44)$  reaction when  $E_\gamma = 750$  MeV using the new parameter set

fifteen times that of the  $D_{13}(1520)$ , and that the two contributions interfere destructively.

The two differences that have arisen from the new parameter set are readily explained by looking at the changes to the parameters given in Table 4.1. The  $\Gamma$  operator for the  $D_{13}(1520)$  resonance, as given by equations (2.56) and (2.57), is proportional to a factor of  $f_{\eta ND_{13}} \kappa_{D_{13}}^{(1)}$  or  $f_{\eta ND_{13}} \kappa_{D_{13}}^{(2)}$ . The total  $D_{13}(1520)$  cross section goes as the square of  $\Gamma_{D_{13}}$ , so the changes to  $f_{\eta ND_{13}} \kappa_{D_{13}}^{(1)}$  and  $f_{\eta ND_{13}} \kappa_{D_{13}}^{(2)}$  given in Table 4.1 result in an increase in the  $D_{13}(1520)$  cross section by a

factor of about seven. Given that the  $S_{11}(1535)$  parameters are relatively stable, we can easily see how the ratio of the  $S_{11}(1535)$  contribution to the  $D_{13}(1520)$  contribution decreases from about fifteen to about three when we use the new parameter set. The constructive interference of the  $S_{11}(1535)$  and the  $D_{13}(1520)$  amplitudes that we observe with the new parameter set results from the change in the sign of  $\kappa_{S_{11}}$  in Table 4.1.

In summary, we have shown that our calculations are quite sensitive to the numerical values of the parameters used in the effective Lagrangian. More work needs to be done to constrain these parameters and, perhaps more importantly, to interpret their relative signs correctly.



# Chapter 5

## Conclusion

In this thesis, we have developed a relativistic model to describe incoherent photoproduction of  $\eta$  mesons on complex nuclei. The dynamics of the elementary process are described with an effective Lagrangian containing photons, nucleons, mesons, and nucleon resonances. In addition to the  $\eta$  meson, we include the  $\rho$  and  $\omega$  vector mesons. We use three nucleon resonances: the  $P_{11}(1440)$ , the  $S_{11}(1535)$ , and the  $D_{13}(1520)$ . From this effective Lagrangian, we derive expressions for all the different terms that comprise the reaction amplitude. Each of these terms corresponds to a Feynman diagram, so we elucidate a set of Feynman rules that automate these derivations.

This treatment of the  $\eta$ -photoproduction process is then extended to a nuclear target. The nucleon wavefunctions are obtained with the Dirac equation using scalar and vector potentials that simulate the meson exchanges responsible for nuclear binding. The Nuclear Shell Model is used to describe nuclear structure so that individual nucleons are labeled by their angular momentum quantum numbers. Spectroscopic factors arise from the amplitude with which a given nucleon state couples to a core state to yield a specific nuclear state.

The wavefunction of the  $\eta$  meson is a solution of the Klein-Gordon equation. An optical potential serves to account for the interactions of the  $\eta$  meson with the nucleus after the  $\eta$  meson is produced.

From the reaction amplitude, we derive expressions for the physical observables of the reaction such as the differential cross section and the photon asymmetry. These expressions, while in an aesthetically pleasing analytic form, do not immediately lend themselves to numerical calculations. Therefore, we exhibit a series of procedures which transform these expressions into more manageable ones. In the process, we introduce the Plane Wave Approximation (PWA) and the Distorted Wave Approximation (DWA) as two different frameworks within which we can perform numerical calculations. We introduce two different optical potentials to describe the final-state interactions of the  $\eta$  meson with the nucleus. We then discuss the computer programs that we have written to perform these calculations.

We present the results of our calculations for a variety of different reaction scenarios. In particular, we consider three different nuclear targets:  $^{12}\text{C}$ ,  $^{16}\text{O}$ , and  $^{40}\text{Ca}$ . We find that the  $S_{11}(1535)$  resonance plays the most important role in the process, especially near the reaction threshold. Both of the optical potentials that we consider cause the cross sections to be lowered from their PWA values by as much as a factor of two, although the two potentials behave differently with respect to the energy of the  $\eta$  meson. The photon asymmetries are found to be quite small in the regions within which the differential cross section is nonnegligible. The differential cross sections depend more heavily on the angular momentum and energy of the final state of the nucleus than they do on the identity of the initial nucleus.

The model calculations mentioned above were made more realistic by invoking

the isospin dependence of the elementary amplitude. This allowed the calculation of the cross sections for nuclear states with definite isospin. Surprisingly, we find that reactions leading to isoscalar nuclear final states are heavily suppressed relative to their isovector counterparts. Furthermore, the modifications that we make to our model lead to cross sections that are significantly lower than those of our original model calculations. This is to be expected since the latter used maximum values of the spectroscopic factors and effectively summed over possible isospin states.

We compare the results of one of our sets of calculations to a set of calculations obtained by other authors using a nonrelativistic model for incoherent  $\eta$ -photoproduction. We find that our calculations yield cross sections that are about a factor of two smaller than their nonrelativistic counterparts. This feature was also observed in previous comparisons of relativistic and nonrelativistic calculations for quasifree  $\eta$ -photoproduction reactions.

We also compare the results of our calculations for individual incoherent cross sections to a set of calculations for coherent  $\eta$ -photoproduction. We observe that the incoherent cross sections are roughly the same size as the coherent cross section.

We note that our predictions for the cross sections of a typical incoherent process fall several orders of magnitude below the data for the inclusive  $\eta$ -photoproduction reaction. This indicates that the cross sections for the quasifree process overwhelm those of the incoherent process. Consequently, experiments to measure the incoherent process will face the challenge of distinguishing between incoherent and quasifree events with enough precision to identify the incoherent signal reliably.

Finally, we examine the dependence of our results on the choice of numerical

parameters for the effective Lagrangian. Using a parameter set based on the most recent data for elementary  $\eta$ -photoproduction reactions, we find that our calculations are quite sensitive to changes in some of these parameters. In particular, the relative magnitudes and phases of the  $S_{11}(1535)$  and the  $D_{13}(1520)$  parameters need to be more precisely determined.

There are a few notable areas within which improvements could be made to our model and our calculations. From a numerical perspective, as mentioned previously, a better description of the elementary  $\eta$ -photoproduction reaction would lead to more accurate and precise parameters in our effective Lagrangian. In addition, there are discrepancies between the different optical potentials used to describe the final state interactions of the  $\eta$  meson with the nucleus. A better understanding of the  $\eta N$  interaction, with particular emphasis on the energy dependence of this interaction, would reduce the uncertainties in the optical potential, and consequently, in our DWA calculations. One aspect of our derivation of the reaction amplitude that is a prime candidate for improvement is the set of approximations made to the propagators for the nucleons and the nucleon resonances in Section 2.3.5. By allowing free propagation through the nuclear medium, we have ignored any medium modifications that might affect the propagation of these particles. Furthermore, we have used the assumption that the particles at the vertices are plane waves in order to be able to evaluate explicitly two of the four-dimensional integrals that we encounter. This results in a zero-range description of the  $\eta$ -photoproduction process.

The formalism and techniques that we have used are quite general and can be applied to the theoretical study of a wide variety of reactions. In particular, there has recently been a great deal of interest in strangeness, ranging from the strange content of the nucleon, through strange nuclei, and all the way up to strange stars.

In this spirit, our model could be used to investigate the photoproduction of  $K$  mesons from nuclei. The study of these reactions would help us gain a better understanding of  $K$  mesons and the properties of the strange nuclei that would be left behind.

# Bibliography

- [1] C. Bennhold and H. Tanabe, Nucl. Phys. A **530**, 625 (1991).
- [2] Phys. Rev. D **54**, 1 (1996).
- [3] B. Krusche *et al.*, Phys. Rev. Lett. **74**, 3736 (1995).
- [4] B. Krusche *et al.*, Phys. Lett. B **358**, 40 (1995).
- [5] M. Röbig-Landau *et al.*, Phys. Lett. B **373**, 45 (1996).
- [6] CLAS Collaboration, CEBAF Experiment 91-008.
- [7] CLAS Collaboration, CEBAF Experiment 94-008.
- [8] M. Benmerrouche, N. C. Mukhopadhyay, and J. F. Zhang, Phys. Rev. D **51**, 3237 (1995).
- [9] C. Bennhold and H. Tanabe, Phys. Lett. B **243**, 13 (1990).
- [10] L. Tiator, C. Bennhold, and S. S. Kamalov, Nucl. Phys. A **580**, 455 (1994).
- [11] F. X. Lee, L. E. Wright, C. Bennhold, and L. Tiator, Nucl. Phys. A **603**, 345 (1996).
- [12] R. C. Carrasco, Phys. Rev. C **48**, 2333 (1993).

- [13] A. Hombach *et al.*, *Z. Phys. A* **352**, 223 (1995).
- [14] M. Effenberger and A. Sibirtsev, *Nucl. Phys. A* **632**, 99 (1998).
- [15] L. Chen and H. Chiang, *Phys. Lett. B* **632**, 424 (1994).
- [16] A. Fix and H. Arenhövel, *Nucl. Phys. A* **620**, 457 (1997).
- [17] M. Hedayati-Poor and H. S. Sherif, *Phys. Rev. C* **56**, 1557 (1997).
- [18] M. Hedayati-Poor and H. S. Sherif, *Phys. Rev. C* **58**, 326 (1998).
- [19] M. Hedayati-Poor, Ph.D. thesis, University of Alberta, 1997.
- [20] W. Peters, H. Lenske, and U. Mosel, *Nucl. Phys. A* **642**, 506 (1998).
- [21] B. M. K. Nefkens, in *Few-Body Systems Suppl.* (Springer-Verlag, Vienna, 1995), No. 9, pp. 193–202.
- [22] B. D. Serot and J. D. Walecka, in *Advances in Nuclear Physics*, edited by J. W. Negele and E. Vogt (Plenum, New York, 1986), Vol. 16.
- [23] S. Weinberg, *The Quantum Theory of Fields* (Cambridge University Press, New York, 1995), Vol. 1.
- [24] J. I. Johansson, Ph.D. thesis, University of Alberta, 1993.
- [25] J. D. Bjorken and S. D. Drell, *Relativistic Quantum Mechanics* (McGraw-Hill, Toronto, 1964).
- [26] R. N. Zare, *Angular Momentum* (Wiley, Toronto, 1988).
- [27] G. Lotz, Ph.D. thesis, University of Alberta, 1989.
- [28] J. D. Jackson, *Classical Electrodynamics*, 2nd ed. (Wiley, Toronto, 1975).

- [29] K. L. G. Heyde, *The Nuclear Shell Model* (Springer-Verlag, New York, 1990).
- [30] V. Gillet and N. V. Mau, Nucl. Phys. A **54**, 321 (1964).
- [31] V. Gillet and E. A. Sanderson, Nucl. Phys. A **91**, 292 (1967).
- [32] S. Cohen and D. Kurath, Nucl. Phys. **73**, 1 (1965).
- [33] S. Cohen and D. Kurath, Nucl. Phys. A **101**, 1 (1967).
- [34] R. Hagedorn, *Relativistic Kinematics* (Benjamin, Reading, 1963).